

## Deep Synoptic Array Science: Polarimetry of 25 New Fast Radio Bursts Provides Insights into their Origins

MYLES B. SHERMAN,<sup>1</sup> LIAM CONNOR,<sup>1</sup> VIKRAM RAVI,<sup>1,2</sup> CASEY LAW,<sup>1,2</sup> GE CHEN,<sup>1</sup>  
MORGAN CATHA,<sup>2</sup> JAKOB T. FABER,<sup>1</sup> GREGG HALLINAN,<sup>1,2</sup> CHARLIE HARNACH,<sup>2</sup>  
GREG HELLBOURG,<sup>1,2</sup> RICK HOBBS,<sup>2</sup> DAVID HODGE,<sup>1</sup> MARK HODGES,<sup>2</sup> JAMES W. LAMB,<sup>2</sup>  
PAUL RASMUSSEN,<sup>2</sup> KRITTI SHARMA,<sup>1</sup> JUN SHI,<sup>1</sup> DANA SIMARD,<sup>1</sup> JEAN SOMALWAR,<sup>1</sup>  
REYNIER SQUILLACE,<sup>3</sup> SANDER WEINREB,<sup>1</sup> DAVID P. WOODY,<sup>2</sup> NITIKA YADLAPALLI,<sup>1</sup>

(THE DEEP SYNOPTIC ARRAY TEAM)

<sup>1</sup>*Cahill Center for Astronomy and Astrophysics, MC 249-17 California Institute of Technology, Pasadena CA 91125, USA.*

<sup>2</sup>*Owens Valley Radio Observatory, California Institute of Technology, Big Pine CA 93513, USA.*

<sup>3</sup>*Department of Astronomy, University of Virginia, 530 McCormick Rd, Charlottesville, VA 22904, USA.*

Submitted to AJ

### ABSTRACT

We report on a full-polarization analysis of the first 25 as yet non-repeating FRBs detected at 1.4 GHz by the 110-antenna Deep Synoptic Array (DSA-110) during commissioning observations. We present details of the data-reduction, calibration, and analysis procedures developed for this novel instrument. Faraday rotation measures (RMs) are searched between  $\pm 10^6$  rad m<sup>-2</sup> and detected for 20 FRBs with magnitudes ranging from 4 – 4670 rad m<sup>-2</sup>. 15/25 FRBs are consistent with 100% polarization, 10 of which have high ( $\geq 70\%$ ) linear-polarization fractions and 2 of which have high ( $\geq 30\%$ ) circular-polarization fractions. Our results disfavor multipath RM scattering as a dominant depolarization mechanism. Polarization-state and possible RM variations are observed in the four FRBs with multiple sub-components. We combine the DSA-110 sample with polarimetry of previously published FRBs, and compare the polarization properties of FRB sub-populations and FRBs with Galactic pulsars. Although FRB polarization fractions are typically higher than those of Galactic pulsars, and cover a wider range than those of pulsar single pulses, they resemble those of the youngest (characteristic ages  $< 10^5$  yr) pulsars. Our results support a scenario wherein FRB emission is intrinsically highly linearly polarized, and propagation effects can result in conversion to circular polarization and depolarization. Young pulsar emission and magnetospheric-propagation geometries may form a useful analogy for the origin of FRB polarization.

*Keywords:* Cosmic electrodynamics (318), Extragalactic magnetic fields (507), Radio transient sources (2008), Neutron stars (1108), Polarimetry (1278), Radio pulsars (1353), Pulsars (1306)

## 1. INTRODUCTION

Fast Radio Bursts (FRBs) are energetic, millisecond-duration radio transients of extragalactic origin. There are now over 500 confirmed FRBs recorded in the Transient Name Server<sup>1</sup> (TNS) catalog (Petroff & Yaron 2020). Several lines of evidence point to neutron-star progenitors for FRBs, although models with, e.g., black-hole engines remain viable (e.g., Zhang 2022a). Their exact emission mechanism is unknown, though multiple theories have been proposed. Some models predict emission from maser processes within the immediate plasma environments of neutron stars (Lyubarsky 2014; Metzger et al. 2019). Others associate them with magnetospheric processes nearer to neutron-star surfaces, for example driven by crustal oscillations or magnetic reconnection (Beloborodov 2021; Beniamini et al. 2020; Gu et al. 2016). Although both repeating and as yet one-off bursts can be described by these, other cataclysmic theories imply triggering in compact-object mergers and/or collapse that only produce one-off events (Falcke & Rezzolla 2014; Totani 2013). It is possible that multiple mechanisms are responsible for the FRB phenomenon, possibly even from the same source (e.g. Petroff 2017; Mckinven 2022; Kirsten et al. 2023; Hewitt et al. 2023). Perhaps relatedly, a remarkable diversity of progenitor host-galaxy systems is observed, including globular clusters (Kirsten et al. 2022), dwarf galaxies (Chatterjee et al. 2017; Bhandari et al. 2023), a variety of locations within galaxies on the star forming main sequence of galaxies (Mannings et al. 2021; Gordon et al. 2023), and massive quiescent galaxies (Sharma et al. 2023; Law et al. 2023).

The polarization of FRBs can be used to identify viable emission theories. Coupled with the observed high brightness temperatures  $T_B \gg 10^{12}$  K, high linear polarization implies a coherent emission process such as curvature radiation, inverse-Compton scattering, or synchrotron-maser emission (e.g., Li et al. 2021; Wang et al. 2022a; Qu & Zhang 2023). Smooth variations in the polarization position angle (PPA) over the burst durations can be associated with moving emission sites, in analogy with the rotating vector model applied to pulsar emission, or with propagation effects within or immediately outside the source magnetosphere (Radhakrishnan & Cooke 1969; Ravi & Lasky 2016; Luo et al. 2020; Cho et al. 2020; Oswald et al. 2023). Rapid jumps in PPA, observed in several pulsars, can indicate emission in different modes or from different locations within magnetospheres (e.g., Manchester et al. 1975; Stinebring et al. 1984). Circular polarization and depolarization from 100% linearly polarized bursts typically require mode conversion or absorption during propagation, multiple emission sites, or Faraday depolarization in a strongly magnetized, possibly inhomogeneous medium (Beniamini et al. 2022; Qu & Zhang 2023). Faraday rotation measure (RM) variations observed in some FRBs also hint toward dynamic local environments of FRB progenitors (e.g. Anna-Thomas et al. 2023a; Mckinven et al. 2023; Li et al. 2022). Each mechanism places stringent physical constraints on the sources and near-source environments.

38 FRB sources have published polarization and/or RM data (see Appendix A for a detailed compilation). This small sample has limited the characterization of standard properties, although

<sup>1</sup> <https://www.wis-tns.org/>

a few traits appear commonplace. Specifically, most repeating and non-repeating FRBs possess high linear polarization fractions ( $\geq 70\%$ ) (e.g., Mckinven et al. 2023; Hilmarsson et al. 2021b; Nimmo et al. 2021). Some FRBs have exhibited non-negligible circular polarization ( $\geq 30\%$ , e.g., FRB 20190611B Day et al. 2020). Repeaters appear non-uniform in their properties: some have stable polarization states like FRB 20190208A while others vary from burst to burst, like FRB 20121102A or FRB 20190520B (Mckinven et al. 2023; Feng et al. 2022a; Anna-Thomas et al. 2023a). One-off bursts, for example FRB 20181112A, can have complex time-domain morphologies and polarization properties that evolve over the burst duration (Cho et al. 2020). Polarization properties so far do not appear to be a viable means of distinguishing repeaters from non-repeaters (e.g., Zhang 2022a). Some repeaters exhibit smoothly time-varying RMs on week to month timescales, including FRB 20121102A, FRB 20190520B, and FRB 20180301 (Hilmarsson et al. 2021a; Kumar et al. 2023; Anna-Thomas et al. 2023a). Strong burst to burst variability in linear- and circular-polarization fractions, as well as frequency-dependent oscillations in these quantities, were observed from the repeating source FRB 20201124A (Xu et al. 2022). These were interpreted as originating during propagation through a strongly magnetized, evolving plasma environment within an AU of the FRB source. Frequency-dependent depolarization has also been observed in multiple FRBs (Feng et al. 2022b; Mckinven et al. 2023). This may be described by the stochastic RM model, in which spatial RM variations within a scattering screen depolarize FRB emission as it propagates along multiple pathways (Melrose & Macquart 1998; Beniamini et al. 2022; Yang et al. 2022). No systematic studies of the polarization properties of as yet non-repeating FRBs have been published.

During the commissioning phase of the 110-antenna Deep Synoptic Array (DSA-110), an FRB survey at declination  $\delta = 71^\circ$  at 1.4 GHz observing frequency was conducted. This paper reports on polarimetry of the first 25 FRBs detected with the DSA-110. The remainder of the paper will proceed as follows. Section 2 will describe the DSA-110 observations, polarization pipeline and methods for RM synthesis. We present linear- and circular-polarization fractions for 25 FRBs and RMs for 20 FRBs. Section 3 presents and discusses the physical implications of polarization subgroups based on the DSA-110 sample. In Section 4 we combine the DSA-110 sample with previously published FRBs to compare the polarization properties of repeaters and non-repeaters, and of FRBs with Galactic pulsars. The latter two sections include significant interpretation and discussion. We conclude in Section 5. We encourage the reader to peruse the extensive appendices for a detailed description of methodology in data reduction, analysis and interpretation, as well as a compilation of our data and literature data on FRB and pulsar polarization. We use a selection of symbols and common abbreviations summarized in Table 1. Calibrated full-polarization filterbank data and derived parameters in RMTTable format<sup>2</sup> are made available on the CaltechDATA public repository<sup>3</sup>. These can be accessed through the DSA-110 archive (Morrell & Law 2022).<sup>4</sup> Additional data will be made available upon request to the corresponding author.

## 2. OBSERVATIONS AND DATA ANALYSIS

<sup>2</sup> <https://github.com/CIRADA-Tools/RMTTable>

<sup>3</sup> <https://data.caltech.edu/>

<sup>4</sup> <https://code.deepsynoptic.org/dsa110-archive/>

**Table 1.** Table of Frequently Used Symbols and Abbreviations

| Symbol/<br>Abbreviation | Units      | Definition   |
|-------------------------|------------|--|
| PA, $\chi$              | $^{\circ}$ | Observed linear-polarization position angle without correcting Faraday rotation        |
| PPA, $\chi_0$           | $^{\circ}$ | Intrinsic linear polarization position angle after correcting for all Faraday rotation |
| $L/I$                   | %          | Frequency- and time-averaged debiased fractional linear polarization                   |
| $ V /I$                 | %          | Frequency- and time-averaged fractional absolute value circular polarization           |
| $V/I$                   | %          | Frequency and time-averaged fractional signed circular polarization                    |
| RVM                     |            | Rotating vector model  |
| AP                      |            | Average profiles of Galactic pulsars   |
| SP                      |            | Single pulses from Galactic pulsars  |
| S/N                     |            | Signal to noise ratio  |

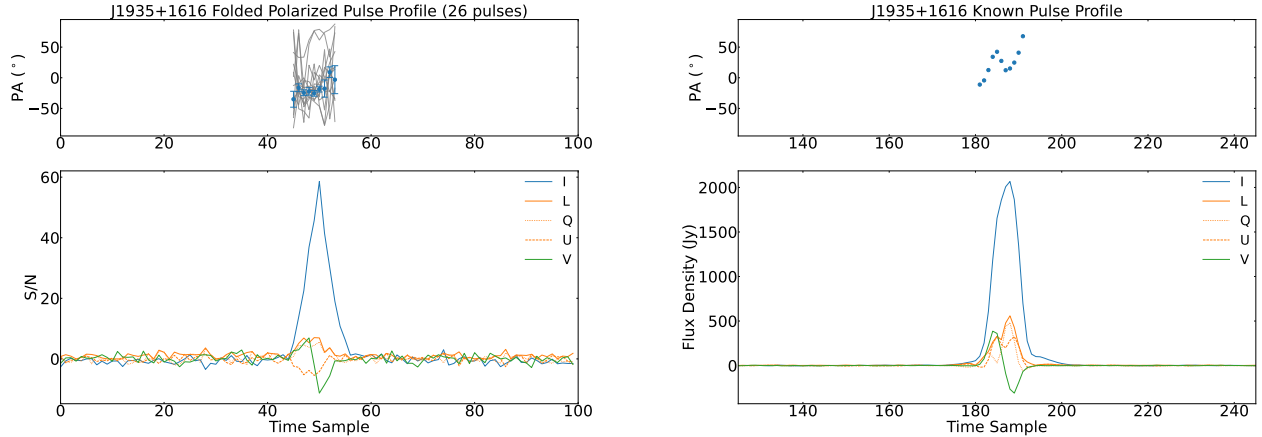


**Figure 1.** Comparison of the pulse profile of PSR J1935 + 1616 observed with the DSA-110 (left) to an archival profile from the European Pulsar Network (right). The observed profile was formed by centroiding and stacking 26 single-pulse detections automatically triggered and processed identically to DSA-110 FRBs. The top panels show the PA of the average profile (blue), and for the DSA-110 bursts, the PA of single pulses (grey). The bottom panels show the Stokes parameters and linear-polarization fraction ( $L/I$ ) as labeled. Besides a PA offset of unknown origin, the profiles are otherwise similar.

The DSA-110 array is currently in its commissioning phase. During the observations reported here, spanning January–November 2022, the array consisted of 48 core antennas for FRB searching, and 15 outrigger antennas to assist in FRB localization. Each 4.65-m antenna is equipped with dual orthogonal linearly polarized receivers, operating between 1280–1530 MHz. A linear basis using the IAU/IEEE handedness convention<sup>5</sup> is used for all polarimetry analysis discussed herein. The antennas are movable in elevation only, and are always pointed at the meridian. All FRBs we present here were detected during a survey at a declination of  $71.6^{\circ}$ . Ravi et al. in prep. will describe the instrument in detail, and some details have been included in previous publications on DSA-110

<sup>5</sup> The IAU/IEEE convention assumes that  $V > 0$  is right-hand polarization, while  $V < 0$  is left-hand polarization (Van Straten et al. 2010).

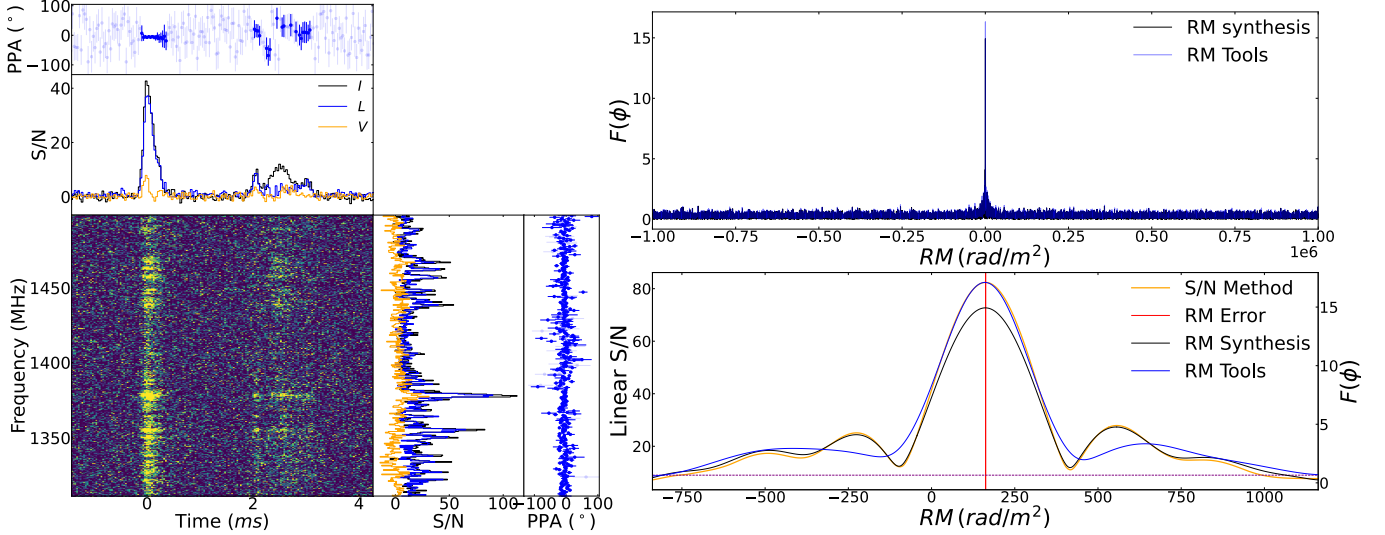


**Figure 2.** Summary of polarization and RM data on FRB 20220207C (*Zach*). Identical plots on all FRBs presented herein are shown in Appendix L. *Left:* From top, we show the PPA (with  $1\sigma$  errorbars) measured after correcting for RM, and frequency averaged time series of Stokes  $I$ ,  $L$ , and  $V$ . The PPA is highlighted in bins with linear-polarization  $S/N > 3\sigma$ . The dynamic spectrum is shown at center, to the right of which are shown optimally summed spectra (Appendix H) and the spectrally resolved PPA with  $> 3\sigma$  bins highlighted. *Right:* The top panel shows the RM spectra evaluated over the full range of sensitivity using two different methods (Appendix I), and the bottom panel shows a detailed analysis of the  $S/N$  of the peak.

FRBs (e.g., Ravi et al. 2022; Law et al. 2023). None of the FRBs presented here have been observed to repeat by the DSA-110 in 150 hours of observing time during 2022 (Law et al. 2023), and we consider them as non-repeaters for the purposes of our analysis. Of the sample of 25 FRBs presented here, arcsecond-scale localizations, and secure host-galaxy association and characterization have been summarized for 11 events by Law et al. (2023). As this paper is focused on the intrinsic polarization properties of the DSA-110 and other FRBs, we do not utilize information (e.g., redshifts) derived from host-galaxy data. A discussion of the RMs of the localized DSA-110 and other FRBs are presented in the companion paper, Sherman et al. (2023).

The calibration and analysis of the full-polarization properties of the 25 FRBs described herein were carried out using standard techniques. The chief novelty of the present analysis is that it is developed from the ground up using a custom implementation on a new telescope. Novel methods were developed for certain aspects of the analysis, such as the estimation of accurate RMs and the corresponding uncertainties. A summary of the calibration and analysis techniques can be found in Appendix B, and Appendices C to I justify them in detail.

In this section we show a single demonstration of the functioning of the polarization calibration and analysis pipeline. Figure 1 displays the calibrated, summed, polarized profile formed from 26 single-pulse detections of bright pulses from the PSR J1935+1616 (B1933). These pulses were detected and processed in exactly the same way as the DSA-110 FRBs. A comparison is made to the reported average profile from the European Pulsar Network (EPN) database of pulsar profiles (Gould & Lyne 1998).<sup>6</sup> Good agreement between the DSA-110 polarization profile and the EPN profile is found:

<sup>6</sup> <http://www.epta.eu.org/epndb/>

note particularly the swing in Stokes V. A time offset in the linear polarization peak is observed, which is attributed to low signal-to-noise of the DSA-110 profile, and pulse summation based on simple centroiding and stacking. An offset in PA is evident between the profiles: our method for deriving PAs is given in Appendix D, and it is unclear exactly what method was used in calibrating the EPN profile. Additional details on verification of the polarization pipeline with J1935+1616 are given in Appendix G.

We present polarization and RM results on all FRBs in Appendix L. Figures 14 to 17 show calibrated and RM-corrected burst temporal profiles and dynamic spectra. Figures 18 to 20 show RM spectra for all FRBs with detectable RMs. Table 2 summarizes the various polarization fractions and RMs for each FRB. Throughout this paper we sometimes refer to DSA-110 FRBs by their internal natural names (e.g., FRB 20220207C is referred to as *Zach*). Correspondence between the natural and formal names is noted in Table 2. Example plots for FRB 20220207C are shown in Figure 2.

Table 2. DSA-110 FRB Sample Polarization Properties

| FRB Names                       | R.A. (°) | Decl. (°) | $n_t$ | $n_f$ | S/N   | L/I           | V/I          | V/I           | RM (rad m <sup>-2</sup> ) | DM (pc cm <sup>-3</sup> )                  |
|---------------------------------|----------|-----------|-------|-------|-------|---------------|--------------|---------------|---------------------------|--|
| FRB 20220121B / "Clare"         | 85.66°   | 64.39°    | 8     | 128   | 13.36 | 70.5 ± 20.6%  | 51.0 ± 12.7% | -51.0 ± 12.7% | -4.6 ± 15.5               | 313.5 ± 0.2                                |
| FRB 20220204A / "Fen"           | 278.27°  | 72.58°    | 6     | 32    | 17.68 | 62.8 ± 15.3%  | 7.5 ± 7.7%   | -6.7 ± 7.7%   | -11.0 ± 11.7              | 612.2 <sup>+0.005</sup> <sub>-0.049</sub>  |
| FRB 20220207C / "Zach"          | 310.2°   | 72.88°    | 1     | 16    | 72.57 | 74.9 ± 4.5%   | 14.8 ± 1.7%  | 11.1 ± 1.7%   | 162.48 ± 0.04             | 262.3 ± 0.01                               |
| FRB 20220208A / "Ishita"        | 322.58°  | 70.04°    | 32    | 256   | 10.70 | 114.3 ± 29.1% | 11.4 ± 15.5% | -11.2 ± 15.5% | -23.3 ± 9.7               | 437.0 <sup>±</sup> 0.6                     |
| FRB 20220307B / "Alex"          | 350.88°  | 72.19°    | 1     | 128   | 15.72 | 69.8 ± 16.0%  | 18.9 ± 8.0%  | -10.3 ± 8.0%  | -947.2 ± 12.3             | 499.15 ± 0.03                              |
| FRB 20220310F / "Whitney"       | 134.72°  | 73.49°    | 1     | 32    | 98.32 | 60.6 ± 4.7%   | 16.6 ± 1.6%  | -7.4 ± 1.6%   | 11.4 ± 0.2                | 462.15 ± 0.004                             |
| FRB 20220319D / "Mark"          | 32.18°   | 71.04°    | 1     | 32    | 56.37 | 16.1 ± 4.0%   | 4.0 ± 2.0%   | -3.0 ± 2.0%   | 59.9 ± 14.3               | 110.95 ± 0.01                              |
| FRB 20220330D / "Erdos"         | 163.75°  | 70.35°    | 40    | 64    | 17.98 | 73.2 ± 17.7%  | 15.8 ± 9.0%  | 3.1 ± 9.0%    | -122.2 ± 4.5              | 468.1 <sup>+0.8</sup> <sub>-0.9</sub>      |
| FRB 20220418A / "Quincy"        | 219.11°  | 70.1°     | 2     | 128   | 16.84 | 64.1 ± 13.3%  | 21.4 ± 7.7%  | 2.7 ± 7.7%    | 6.1 ± 7.5                 | 623.45 ± 0.01                              |
| FRB 20220424E / "Davina"        | 19.51°   | 71.8°     | 2     | 64    | 14.60 | 59.9 ± 16.2%  | 15.8 ± 7.4%  | 15.8 ± 7.4%   | 126.9 ± 13.4              | 863.48 <sup>+0.022</sup> <sub>-0.036</sub> |
| FRB 20220506D / "Oran"          | 318.05°  | 72.83°    | 1     | 32    | 24.17 | 95.3 ± 10.9%  | 31.4 ± 4.6%  | 31.4 ± 4.6%   | -32.4 ± 3.6               | 396.93 ± 0.01                              |
| FRB 20220509G / "Jackie"        | 282.67°  | 70.24°    | 1     | 32    | 40.32 | 98.5 ± 11.1%  | 6.0 ± 2.8%   | 5.4 ± 2.8%    | -109.0 ± 1.2              | 269.5 ± 0.007                              |
| FRB 20220726A / "Gertrude"      | 73.95°   | 69.93°    | 2     | 64    | 18.25 | 93.5 ± 16.7%  | 13.8 ± 6.2%  | -3.7 ± 6.2%   | 499.8 ± 7.2               | 686.55 ± 0.01                              |
| FRB 20220801A / "Augustine"     | 54.96°   | 70.18°    | 4     | 64    | 11.77 | 30.1 ± 18.0%  | 35.8 ± 13.7% | -1.3 ± 13.7%  | -                         | 412.6 ± 0.04                               |
| FRB 20220825A / "Ansel"         | 311.98°  | 72.59°    | 1     | 32    | 32.80 | 53.7 ± 11.4%  | 9.0 ± 5.9%   | -7.4 ± 5.9%   | 750.2 ± 6.7               | 651.2 ± 0.02                               |
| FRB 20220831A / "Ada"           | 338.7°   | 70.54°    | 6     | 64    | 21.28 | 84.6 ± 12.8%  | 16.8 ± 5.3%  | 1.7 ± 5.3%    | 772.1 ± 7.2               | 1146.25 ± 0.2                              |
| FRB 20220914A / "Elektra"       | 282.06°  | 73.34°    | 1     | 64    | 17.43 | 16.3 ± 14.0%  | 20.5 ± 11.9% | 11.9 ± 11.9%  | -                         | 631.05 ± 0.02                              |
| FRB 20220920A / "Etienne"       | 240.26°  | 70.92°    | 2     | 128   | 18.88 | 89.0 ± 16.2%  | 19.7 ± 8.1%  | -14.9 ± 8.1%  | -830.3 ± 8.3              | 315.0 ± 0.06                               |
| FRB 20220926A / "Celeste"       | 328.73°  | 72.86°    | 2     | 128   | 18.16 | 17.5 ± 21.0%  | 9.5 ± 14.2%  | 2.0 ± 14.2%   | -                         | 441.53 ± 0.03                              |
| FRB 20221002A / "Armi"          | 281.0°   | 71.6°     | 12    | 256   | 8.08  | 26.8 ± 22.7%  | 19.7 ± 18.1% | -12.5 ± 18.1% | -                         | 322.5 ± 1.0                                |
| FRB 20221012A / "Juan" †        | 280.8°   | 70.52°    | 8     | 32    | 9.33  | 63.0 ± 21.4%  | 25.7 ± 11.0% | 0.6 ± 10.9%   | 165.7 ± 17.7              | 441.2 ± 0.26                               |
| FRB 20221027A / "Koyaanisqatsi" | 130.9°   | 71.6°     | 1     | 32    | 21.82 | 8.3 ± 7.0%    | 18.4 ± 5.2%  | -2.2 ± 5.2%   | -                         | 452.5 <sup>‡</sup>                         |
| FRB 20221029A / "Mifanshan"     | 143.8°   | 71.6°     | 4     | 128   | 17.12 | 85.7 ± 16.1%  | 15.6 ± 7.0%  | 6.8 ± 7.0%    | -155.8 ± 9.7              | 1391.05 <sup>‡</sup>                       |
| FRB 20221101B / "Nina"          | 342.0°   | 71.5°     | 4     | 32    | 14.21 | 99.3 ± 19.3%  | 24.5 ± 8.7%  | -19.4 ± 8.7%  | -32.2 ± 9.1               | 490.7 <sup>‡</sup>                         |
| FRB 20221101A / "Ayo"           | 75.6°    | 71.6°     | 2     | 64    | 19.27 | 55.3 ± 11.3%  | 11.6 ± 6.2%  | -5.5 ± 6.2%   | 4670.4 ± 10.8             | 1476.5 <sup>‡</sup>                        |

Notes:  $n_t$  and  $n_f$  are the downsampling factors in time and frequency from the native DSA-110 resolution (see Appendix B) used to maximize S/N. The total, linear, absolute value of circular and signed circular polarization are given in columns 7, 8, 9, and 10. The right ascension and declination given are the ICRS frame coordinates of the beam in which the FRB was detected.

† FRB 20221012A's polarization is computed after derotating to the reported RM. This detection was marginal, with low linear-polarization S/N below the  $9\sigma$  threshold. However, this is taken as a reliable measurement given the clear peak the RM spectrum (Figure 20) and apparent coherence when compared to the RMSF.

‡ Detailed burst structure analysis used to estimate DM errors has not yet been performed for these FRBs. See G. Chen et al., in preparation for details.

### 3. DISCUSSION OF INDIVIDUAL BURST POLARIZATION PROPERTIES

#### 3.1. *Motivation for Polarization-based Classification*

The DSA-110 FRB sample spans a wide range of polarimetric and spectro-temporal properties. This is the largest uniform sample of FRB polarization, and motivates its use as a basis for a polarization-dependent classification scheme. The need for such classes stems from the ability of polarimetry to distinguish FRB emission and propagation models. The high brightness temperatures observed in FRBs require a coherent, highly polarized emission process (e.g. Luan & Goldreich 2014). This could apply to pulsar-like ‘antenna’ mechanisms driven by charged particle bunches within the magnetosphere or synchrotron ‘maser’ emission via a shocked wind outside the magnetosphere (e.g. Metzger et al. 2019; Wang et al. 2022b,a; Zhang 2022a,b; Qu & Zhang 2023). ‘Antenna’ mechanisms appear more likely, since the observed circular polarization and de-polarization in FRBs require propagation through an extreme local plasma environment. For example, Faraday Conversion (FC) and cyclotron absorption each result in circular polarization; their presence would represent evidence of a highly magnetized, dense plasma nearby the source (e.g. Vedantham & Ravi 2019; Gruzinov & Levin 2019; Suresh & Cordes 2019; Kumar et al. 2022; Qu & Zhang 2023). Similarly, depolarization can indicate either multi-path scattering through a screen with non-uniform RM (e.g. Melrose & Macquart 1998), or the superposition of multiple emission modes (e.g. Mitra et al. 2023); these can be investigated through multi-band, high time-resolution polarization studies of FRBs (e.g. Hankins et al. 2003; Feng et al. 2022b; Mckinven et al. 2023). A generalized classification scheme will help identify the characteristic FRB polarization properties to narrow the range of likely FRB theories.

To date, the predominant FRB categorization method was offered by Pleunis et al. (2021) based on observations of FRBs from the Canadian Hydrogen Intensity Mapping Experiment (CHIME). Their classes were based on the spectro-temporal morphology of FRBs detected in the 400-800 MHz band. However, we find these classes insufficient to describe the full DSA-110 sample’s morphological properties. Furthermore, these classes do not include FRB polarization, for which we would like a straightforward and replicable classification framework. The DSA-110, whose polarization calibration scheme is verified in Appendices E, F, and G, is well-equipped to define polarization sub-classes using the uniform sample of 25 FRBs presented here. However, we acknowledge that such a classification scheme would be limited by the DSA-110 sensitivity, and furthermore cannot be generalized beyond L-band detections. While we hope that these sub-groups will form the groundwork for a more general, polarization- and frequency-dependent classification scheme, we make no claims on its universality in the current iteration. Polarization properties are also difficult to distinguish from being intrinsic or the result of propagation effects. Therefore, while we identify classes based on total, linear, and circular polarization, we use them primarily to motivate a more detailed discussion of linear and circular polarization in the following section.

We define four unique polarization sub-groups which are applied in turn to the total, linear, and circular polarization fractions of each DSA-110 FRB:

1. **Consistent with 100% Polarized:** The polarization fraction falls within  $3\sigma$  of 100% and beyond  $3\sigma$  of 0%.
2. **Consistent with 0% Polarized:** The polarization fraction falls within  $3\sigma$  of 0% and beyond  $3\sigma$  of 100%.
3. **Intermediate:** The polarization fraction falls beyond  $3\sigma$  of both 100% and 0%.

4. **Unconstrained:** The polarization fraction falls within  $3\sigma$  of both 100% and 0%. This is equivalent to stating the polarization is not well-defined.

We then define two orthogonal sub-groups which generalize and place more quantitative limits on the morphological classes of Pleunis et al. (2021):

1. **Single Component:** Bursts exhibit one component (on approx. millisecond timescales).
2. **Multi-Component:** Bursts exhibit multiple components separated on millisecond timescales.

In Table 3, we sort the DSA-110 sample among these sub-classes using total, linear, and circular polarization fractions. For the remainder of the paper, the sub-groups **Consistent with 100% Polarized**, **Consistent with 0% Polarized**, **Intermediate**, and **Unconstrained** will refer only to the total polarization-based sub-groups unless otherwise noted. In the next section, we explore the specific properties of FRBs in each class. Figure 3 shows  $L/I$  and  $|V|/I$  for the DSA-110 FRBs, grouped by their polarization class.

### 3.2. Single Component FRBs

A significant majority 21/25 of the DSA-110 sample are described by a single component on millisecond timescales, with most (13) of these being **Consistent with 100%** polarization. 3 **Single Component** FRBs fall into each of the **Consistent with 0%** and **Intermediate** classes, while two have **Unconstrained** polarization properties. In this section we explore the characteristic polarization properties of **Single Component** FRBs.

#### 3.2.1. Linear Polarization

As shown in Figure 3, all FRBs that are **Consistent with 100%** have  $L/I > 50\%$ , including 13 **Single Component** bursts; two-thirds of these (10) have  $L/I > 70\%$ . This is not uncommon among FRBs, as 36% of previously published repeaters and non-repeaters with L-band (1.4 GHz) polarization measurements also have  $L/I > 50\%$ . This large fraction of highly linearly polarized FRBs supports coherent radiation models such as curvature radiation from coherent charge bunches (Wang et al. 2022a; Qu & Zhang 2023). While Feng et al. (2022b) demonstrate that repeaters become depolarized at lower frequencies, they associate this with stochastic RM scattering rather than intrinsic emission. Coherent radiation models are further supported by the relatively flat PPA’s observed in this group. A  $\chi^2$  goodness-of-fit test was conducted to compare the PPA in time bins with linear-polarization  $S/N > 3\sigma$  to the weighted average PPA value (see Appendix K). None of the 13 **Single Component** FRBs consistent with 100% polarization were found with significant variations ( $p < 10\%$ ) in position angle. This may imply that there is a single dominant polarization mode in most FRBs, and resembles the behavior of young, high spin-down pulsars (Weltevrede & Johnston 2008; Ravi et al. 2010; Mitra et al. 2016). In Section 4.2, we explore possible connections between FRBs and young pulsars in more detail. Notably, of FRBs in the **Consistent with 100%** and **Intermediate** sub-groups, only FRB 20220319D has a linear polarization fraction below 20%, a trait shared only by the 3 FRBs that are **Consistent with 0%**.

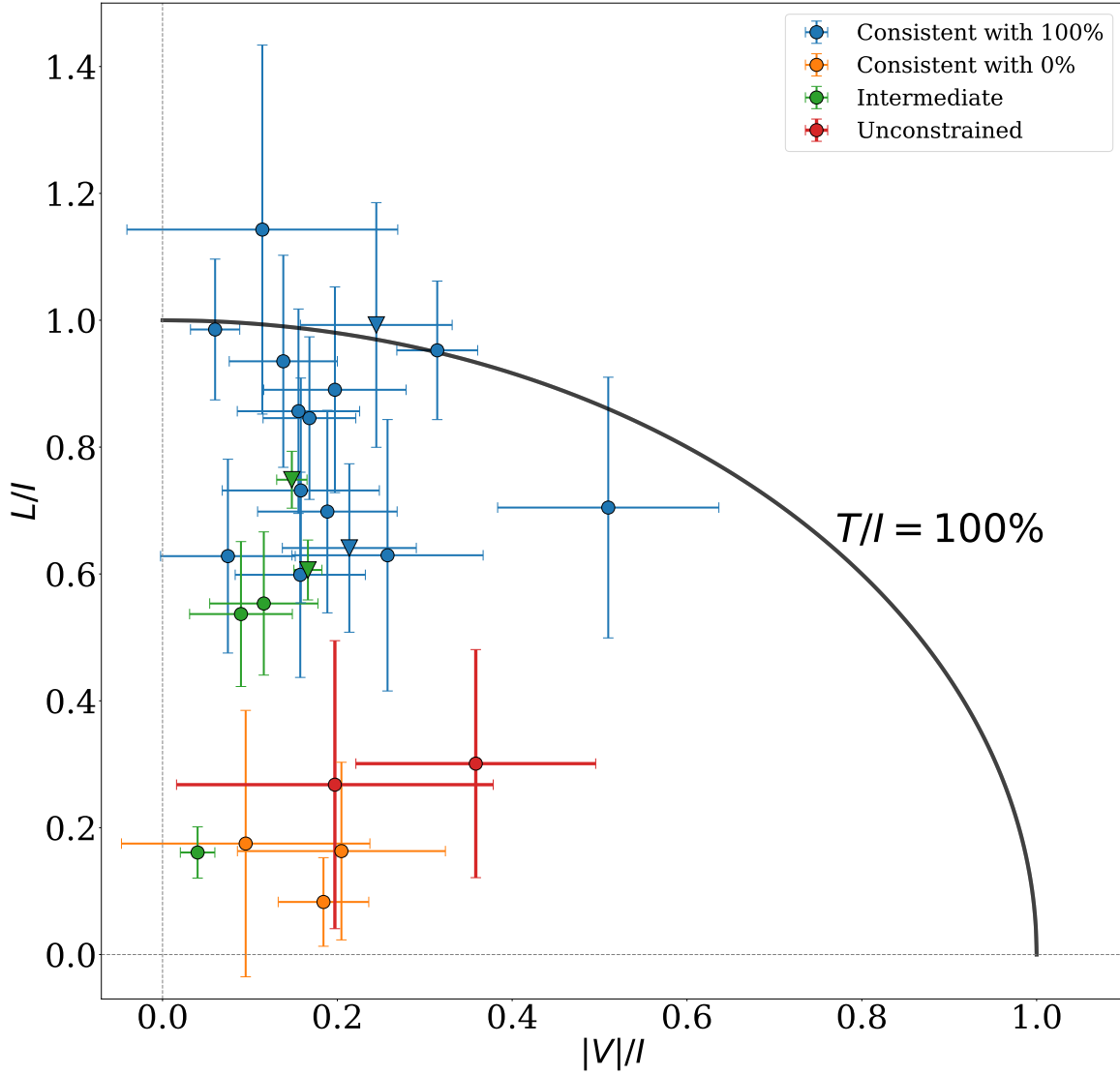


**Figure 3.** Linear and Absolute Value Circular Polarization for DSA-110 FRBs. Each FRB is color-coded by its polarization class as reported in Table 3. **Single Component** FRBs are shown as circles and **Multi-Component** FRBs are shown as triangles. The errorbars shown are  $1\sigma$  uncertainties. The black line indicates where the total-polarization fraction  $T/I = \sqrt{(|V|/I)^2 + (L/I)^2} = 100\%$ . While all **Consistent with 100%** (blue) and most **Intermediate** (green) FRBs have  $L/I > 50\%$ , FRB 20220121B and FRB 20220506D also show significant circular polarization. FRB 20220319D is the only FRB in either class with less than 50% total polarization. All **Consistent with 0%** FRBs (orange) have  $L/I$  and  $|V|/I$  below 25%.

**Table 3.** Polarization-based FRB subgroups from DSA-110 data.

|  | Consistent with 100%                 | Consistent with 0%              | Intermediate                    | Unconstrained                  |
|--|--------------------------------------|---------------------------------|---------------------------------|--------------------------------|
| Total Polarization<br>( $\sqrt{(L/I)^2 + (V/I)^2}$ ) | FRB 20220121B (1)                    |                                 |                                 |                                |
|  | FRB 20220204A (1i)                   |                                 |                                 |                                |
|  | FRB 20220208A (1a)                   |                                 |                                 |                                |
|  | FRB 20220307B (1)                    |                                 |                                 |                                |
|  | FRB 20220330D (1i)                   |                                 |                                 |                                |
|  | FRB 20220424E (1i)                   |                                 | FRB 20220319D (1i)              |                                |
|  | FRB 20220506D (1ia)                  | FRB 20220914A (1i)              | FRB 20220825A (1ia)             | FRB 20220801A (1ia)            |
|  | FRB 20220509G (1ia)                  | FRB 20220926A (1)               | FRB 20221101A (1a)              | FRB 20221002A (1)              |
|  | FRB 20220726A (1a)                   | FRB 20221027A (1i) <sup>†</sup> | <b>FRB 20220207C (2ia)</b>      |                                |
|  | FRB 20220831A (1a)                   |                                 | <b>FRB 20220310F (2ia)</b>      |                                |
|  | FRB 20220920A (1)                    |                                 |                                 |                                |
|  | FRB 20221012A (1) <sup>‡</sup>       |                                 |                                 |                                |
|  | FRB 20221029A (1i)                   |                                 |                                 |                                |
|  | <b>FRB 20220418A (3a)</b>            |                                 |                                 |                                |
|  | <b>FRB 20221101B (2)</b>             |                                 |                                 |                                |
| Linear Polarization<br>( $L/I$ )                     | FRB 20220121B (1)                    |                                 |                                 |                                |
|  | FRB 20220204A (1i)                   |                                 |                                 |                                |
|  | FRB 20220208A (1a)                   |                                 |                                 |                                |
|  | FRB 20220307B (1)                    |                                 |                                 |                                |
|  | FRB 20220330D (1i)                   |                                 |                                 |                                |
|  | FRB 20220424E (1i)                   | FRB 20220914A (1i)              | FRB 20220319D (1i)              |                                |
|  | FRB 20220506D (1ia)                  | FRB 20220926A (1)               | FRB 20220825A (1ia)             |                                |
|  | FRB 20220509G (1ia)                  | FRB 20221027A (1i) <sup>†</sup> | FRB 20221101A (1a)              | FRB 20221012A (1) <sup>‡</sup> |
|  | FRB 20220726A (1a)                   | FRB 20220801A (1ia)             | <b>FRB 20220207C (2ia)</b>      |                                |
|  | FRB 20220831A (1a)                   | FRB 20221002A (1)               | <b>FRB 20220310F (2ia)</b>      |                                |
|  | FRB 20220920A (1)                    |                                 |                                 |                                |
|  | FRB 20221029A (1i)                   |                                 |                                 |                                |
|  | <b>FRB 20220418A (3a)</b>            |                                 |                                 |                                |
|  | <b>FRB 20221101B (2)</b>             |                                 |                                 |                                |
|  | Circular Polarization<br>( $ V/I $ ) |                                 | FRB 20220121B (1)               |                                |
|  |                                      | FRB 20220204A (1i)              |                                 |                                |
|  |                                      | FRB 20220208A (1a)              |                                 |                                |
|  |                                      | FRB 20220307B (1)               |                                 |                                |
|  |                                      | FRB 20220330D (1i)              |                                 |                                |
|  |                                      | FRB 20220424E (1i)              |                                 |                                |
|  |                                      | FRB 20220509G (1ia)             |                                 |                                |
|  |                                      | FRB 20220726A (1a)              | FRB 20220121B (1)               |                                |
|  |                                      | FRB 20220920A (1)               | FRB 20220506D (1ia)             |                                |
|  |                                      | FRB 20221012A (1) <sup>‡</sup>  | FRB 20221027A (1i) <sup>†</sup> |                                |
|  |                                      | FRB 20221029A (1i)              | <b>FRB 20220207C (2ia)</b>      |                                |
|  |                                      | FRB 20220801A (1ia)             | <b>FRB 20220310F (2ia)</b>      |                                |
|  |                                      | FRB 20221002A (1)               | FRB 20220831A (1a)              |                                |
|  |                                      | FRB 20220914A (1i)              |                                 |                                |
|  |                                      | FRB 20220926A (1)               |                                 |                                |
|  |                                      | FRB 20220319D (1i)              |                                 |                                |
|  |                                      | FRB 20220825A (1ia)             |                                 |                                |
|  |                                      | FRB 20221101A (1a)              |                                 |                                |
|  |                                      | <b>FRB 20220418A (3a)</b>       |                                 |                                |
|  |                                      | <b>FRB 20221101B (2)</b>        |                                 |                                |

**Notes:** DSA-110 FRBs sorted into subgroups based on polarization significance as described in Section 3. Each burst is labeled with the number of resolved components, an “i” if the burst shows significant spectral striation, and an “a” if the burst shows significant scattering (G. Chen et al., in prep.). **Multi-Component** FRBs are boldfaced, while **Single-Component** FRBs are in regular font.

<sup>†</sup>FRB 20221027A is a unique FRB whose total polarization is **Consistent with 0%**, but which has **Intermediate** circular polarization. This is attributed to its insignificant linear polarization which adds noise to the total polarization estimate.

<sup>‡</sup>FRB 20221012A has a total polarization that is **Consistent with 100%** and a circular polarization that is **Consistent with 0%**, but its linear polarization is **Unconstrained**. From RM synthesis, we marginally detect an RM, although the peak in the RM spectrum has linear S/N below the  $9\sigma$  threshold as shown in Figure 20. This suggests there is significant linear polarization which contributes to the total, though we cannot make more constraining statements within our current classification scheme.

### 3.2.2. Circular Polarization

Circular polarization appears to be less common than linear polarization among the **Single Component** sample. Only two FRBs that are **Consistent with 100%** or **Intermediate** have  $|V|/I > 30\%$ : FRB 20220121B and FRB 20220506D. Both are **Consistent with 100%** and show no clear splitting of different signs of Stokes V. This is consistent with circular polarization originating through the propagation effects discussed above. A third FRB, FRB 20220801A, also has a high  $|V|/I$ , but falls into the **Unconstrained** subgroup, making any evident polarization difficult to confirm. We do not observe any changes in the sign of Stokes V within FRB 20220121B and FRB 20220506D, as are often observed at the centers of the main components in radio-pulsar APs (Radhakrishnan & Rankin 1990). Furthermore, while most **Single Component** FRBs appear to have negligible circular polarization (evident from both  $|V|/I$  fractions and polarized profiles in Figures 14-17), all four **Multi-Component** bursts appear to have significant circular polarization. We will explore this further in the next section.

The large fraction of FRBs that exhibit high linear polarization, as opposed to circular polarization, suggests that the intrinsic emission mechanism is often highly linearly polarized. Circular polarization and depolarization may then arise primarily from propagation effects. In this scenario, depolarization from the intrinsic mechanism due to unresolved micro or nano-second scale structure may be less significant than propagation effects, in contrast to pulsar radio emission (Mitra et al. 2015; Cordes 1976; Hankins et al. 2003). However, this claim cannot be confirmed without higher time resolution observations of FRBs.

The limited 187 MHz bandwidth and 972 kHz resolution<sup>7</sup> of the DSA-110 spectra prevent detailed fits of frequency-dependent FC models. Instead, by assuming FC is significant in the region of interest, we can estimate the magnetic-field strength from frequency-averaged quantities as follows (Gruzinov & Levin 2019). One can estimate the Faraday Conversion Measure (CM) from the root mean squared circular polarization of each FRB, assuming the circular emission arises from FC at a single magnetic field reversal:

$$\sqrt{\langle V(\lambda^2)^2 \rangle} = \sqrt{2(e^{-(\text{CM}\lambda^2)^2/2} - e^{-(\text{CM}\lambda^2)^2})} \quad (1)$$

The CM can be related to the RM and total magnetic field strength,  $B$ , by:

$$\text{CM} \approx B \sqrt{\text{RM} \left( \frac{8\pi^3 e^2}{m_e^3 c^4} \right)} \sim 10^{-2} \left( \frac{B}{1 \text{ G}} \right) \left( \frac{\text{RM}}{1 \text{ rad m}^{-2}} \right)^{1/2}, \quad (2)$$

where  $e$  is the electron charge,  $m_e$  is the electron mass, and  $c$  is the vacuum speed of light. For FRB 20220121B and FRB 20220506D, we measure root mean squared circular polarization  $\sqrt{\langle V(\lambda^2)^2 \rangle} \approx 50\%$  and  $40\%$ , corresponding to conversion measures  $\text{CM} \approx 10 \text{ m}^{-2}$  in both cases. Given their RMs of  $-4.60 \pm 15.48 \text{ rad m}^{-2}$  and  $-32.38 \pm 3.60 \text{ rad m}^{-2}$ , we estimate magnetic field strengths of  $B \approx 510 \text{ G}$  and  $150 \text{ G}$ , respectively. These high field strengths are not consistent with supernova-remnant and plerionic environments, including those of the FRBs associated with persistent radio sources (e.g., Vedantham & Ravi 2019). However, motivated by the likely FC observed during eclipses of the binary-system PSR B1744 – 24A (Li et al. 2023), the magnetized wind of a companion to the FRB progenitors is a reasonable possibility for the conversion site.

<sup>7</sup> Here we refer to the limited resolution of the spectra in Figures 14-17, which were binned by at least  $32 \times 30.4 \text{ kHz}$  channels to maximize frequency structure.

### 3.2.3. Depolarization

The DSA-110 sample reported here contains 3 **Single Component** FRBs that are **Consistent with 0%** and 3 that have **Intermediate** polarization. 9/16 FRBs in the published literature that have reported errorbars would also fall in these subgroups. Considering the circular polarization subgroups, only FRB 20221027A has an **Intermediate**  $|V|/I$  ( $> 3\sigma$ ) among FRBs with **Intermediate** total polarization<sup>8</sup>. The lack of circular polarization in bursts with low total polarization implies that FC effects are less common, which one expects to depolarize the burst while producing residual circular polarization.

RM variations across a scattering screen are also unlikely to be the dominant depolarization mechanism for the DSA-110 FRBs. The variation in RM is captured by  $\sigma_{\text{RM}}$ , the standard deviation of RM throughout the screen, and depolarization would be highly frequency dependent with the linear-polarization fraction of the form:

$$f_{\sigma_{\text{RM}}} = 1 - e^{-2\sigma_{\text{RM}}^2\lambda^4} \quad (3)$$

This model has been found to match observations of 8 repeating FRBs from 0.1–10 GHz, with  $\sigma_{\text{RM}}$  values from 0.12 rad m<sup>-2</sup> for FRB 20180916B to 218.9 rad m<sup>-2</sup> for FRB 20190520B (Feng et al. 2022b; Mckinven et al. 2023). However, for  $RM < 1000$  rad m<sup>-2</sup>, averaging over the DSA-110 frequency band (1.3–1.5 GHz) without RM correction is the dominant depolarization effect, which we quantify by:

$$f_{\text{avg}} = 1 - \sqrt{\langle \cos(RM\lambda^2) \rangle^2 + \langle \sin(RM\lambda^2) \rangle^2} \quad (4)$$

where  $\langle \rangle$  denotes the mean over frequency. Therefore, if we assume an FRB is intrinsically 100% polarized, we can write the observed polarization fraction as  $L/I \approx f_{\sigma_{\text{RM}}}(RM)f_{\text{avg}}(\sigma_{\text{RM}})$ ; note that channel bandwidth depolarization is negligible in this RM range (see Appendix I). Feng et al. (2022b) (see Figure 4) derives an empirical, linear relation between  $\sigma_{\text{RM}}$  and RM, which we adopt to write Equation 4 in terms of  $\sigma_{\text{RM}}$ . We apply this model to the average polarization of the three bursts with insufficient  $L/I$  for RM measurements: FRB 20220914A, FRB 20220926A, and FRB 20221027A. We find that  $\sigma_{\text{RM}} \approx 0.3 - 1.0$  rad m<sup>-2</sup> could produce the observed polarization fractions for FRB 20220914A and FRB 20220926A, while  $\sigma_{\text{RM}} \approx 0.3 - 3.0$  rad m<sup>-2</sup> could produce the polarization of FRB 20221027A. From Feng et al. (2022b), these correspond to  $RM \approx 200 - 900$  rad m<sup>-2</sup>, which should be detectable with the DSA-110 RM synthesis pipeline; however, no significant RM was found for these three FRBs. Low  $S/N$  could prevent detection, but the low  $\sigma_{\text{RM}}$  suggests that RM synthesis would recover nearly 100% linear polarization, making the maximized linear  $S/N$  in each burst  $\sim 20\sigma$  which exceeds the  $9\sigma$  detection threshold (see Appendix I).

We can perform a similar analysis for **Intermediate** FRBs, which do have RM measurements ranging from 10 – 4670 rad m<sup>2</sup>. We find that  $\sigma_{\text{RM}}$  in the range of 10–20 rad m<sup>-2</sup> would be required for these FRBs. Apart from FRB 20221101A, this is around an order of magnitude higher than expected from Feng et al. (2022b) for these RM magnitudes, and the  $\ll 1$  ms scattering timescales of the DSA-110 FRBs (G. Chen et al., in prep.). Furthermore, assuming a common origin for the scattering and depolarization, the implied magnetic-field variations in the scattering screen are likely to be

<sup>8</sup> With  $|V|/I = 18.4 \pm 5.2\%$ , FRB 20221027A’s linear polarization fraction is noise-dominated; therefore, its total polarization class (**Consistent with 0%**) is likely erroneous due to small errors in noise statistics. We will consider it as an **Intermediate** FRB for this discussion given its significant circular polarization fraction.

uncomfortably high, of order Gauss (Yang et al. 2022; Feng et al. 2022b, Section S4). A potential exception to these arguments is the event FRB 20220319D, as discussed in Appendix J.

The significant fraction of FRBs in the DSA-110 sample that are **Consistent with 0%** or **Intermediate** poses an interesting challenge to theory (Qu & Zhang 2023). The fact that depolarization has long been observed and puzzled over in pulsars, more significantly at high frequencies ( $> 1$  GHz) than low, (e.g., Manchester et al. 1973; Manchester 1971) should provide some hope that a common explanation may be found.

### 3.3. Multi-Component FRBs

4/25 of the DSA-110 sample exhibit multiple components on millisecond timescales<sup>9</sup>. FRB 20220418A and FRB 20221101B are **Consistent with 100% Polarization**, while FRB 20220207C and FRB 20220310F are **Intermediate**. In this section we explore the polarization properties of **Multi-Component** FRBs.

#### 3.3.1. Stable Polarization States

Both FRB 20220207C and FRB 20220310F have two sub-components exhibiting significant linear polarization with  $L/I > 50\%$ . Significant circular polarization ( $> 3\sigma$ ) is also evident, with  $|V|/I \approx 15\%$ . In FRB 20220207C, the first component has a flat PPA while the second fluctuates, although a  $\chi^2_{\nu}$  test finds this variation is not significant (see Appendix K for details). In contrast, FRB 20220310F displays a flat PPA in both components, separated by  $\sim 10^\circ$ . If both components originate from a fixed region in a rotating magnetosphere, this suggests negligible rotation over the approximately millisecond burst durations. A potentially better way to quantify a constraint on the rotation periods of progenitor objects is by assuming emission from coherent charge bunches, as motivated by this specific categorization (Wang et al. 2022a; Qu & Zhang 2023). For this analysis we assume a ‘thin’ bunch of charges, which aligns with the wide range of polarization properties observed in FRBs<sup>10</sup>. In this scenario, the burst duration must be much less than  $(\gamma\Omega)^{-1}$ , where  $\gamma \sim 100$  is the bunch Lorentz factor<sup>11</sup>, and  $\Omega$  is the rotation angular frequency. Applying this condition for the  $\sim 0.3$  ms duration of the first FRB 20220207C burst, we find required rotation periods  $\gg 30$  ms. Similarly, the sub-bursts in FRB 20220310F span  $\sim 0.2$  ms each, for which we find required rotation periods  $\gg 20$  ms under the same curvature radiation assumptions. These estimates are of particular interest since 30 ms roughly demarcates the boundary between millisecond pulsar (MSPs) and slow canonical pulsar (CPs) rotation periods (e.g. Lorimer 2008).

#### 3.3.2. Polarization Variation

What is most striking about these bursts is that the different components appear to have different polarization properties, an effect that persists for non-repeating FRBs from at least the Australian Square Kilometre Array Pathfinder (ASKAP; Cho et al. 2020; Day et al. 2020). In contrast, none of the 21 single-component FRBs had statistically significant PPA variability, suggesting negligible polarization evolution across the burst. The variations between the polarization properties of the

<sup>9</sup> We note that sub-microsecond-scale structures have been previously observed in FRBs (e.g., Majid et al. 2021; Nimmo et al. 2021, 2022), and indeed interesting structure within individual burst components is observed in some DSA-110 FRBs. We defer a high time resolution analysis of DSA-110 FRBs to future work.

<sup>10</sup> For details, see Figures 2, 4, 5, and 6 of Wang et al. (2022a)

<sup>11</sup> We assume  $\gamma \sim 100$  based on the DSA-110 observing frequency 1.4 GHz and the expected curvature radius of magnetic field lines around a neutron star,  $\rho \sim 10^{6-8}$  cm. Using Equation 18 of Qu & Zhang (2023),  $58 \lesssim \gamma \lesssim 270$  are reasonable approximations for a coherent curvature radiation scenario.

sub-components of FRB 20220207C, FRB 20220310F, FRB 20220418A, and FRB 20221101B defy a unified description. FRB 20220418A and FRB 20220207C exhibit multiple components with different polarization properties. FRB 20220207C's sub-components have very different profiles, although a  $\chi^2$  test finds the PPA variation is not significant. Beyond this, the first sub-component is **Consistent with 100%** linear polarization while the second has  $\sim 50\%$  linear polarization and  $\sim 20\%$  circular polarization. FRB 20220418A is less constrained: while the first sub-component has high linear polarization, the second is **Unconstrained** and the third is **Consistent with 0%** linear and circular polarization.

FRB 20220310F's sub-components have more comparable properties, with  $L/I$  of  $54.8 \pm 6.0\%$  and  $67.4 \pm 7.2\%$ , but while the circular-polarization fractions have a similar magnitude, the signs are opposite:  $V/I$  of  $-16.7 \pm 1.3\%$  and  $10.8 \pm 1.8\%$  respectively. Indeed, the polarization states of the two sub-components are individually well-defined, and the average locations of the two sub-components on the Poincaré sphere are almost orthogonal, with an angular separation of  $71 \pm 2$  degrees (Figure 4). These are reminiscent of emission in orthogonally polarized modes observed in several pulsars (Manchester et al. 1975; Stinebring et al. 1984). However, the change in sign of Stokes V between the two components is rarely if ever observed in multi-component pulsar APs (Han et al. 1998). Changes in the sign of Stokes V between components can potentially be interpreted as emission from different magnetic hemispheres, potentially implying rapid rotation of the progenitor (Johnston & Kramer 2019). Alternatively, the opposite signs in circular polarization may indicate that birefringence could be the cause of the split sub-components in FRB 20220310F (Suresh & Cordes 2019; Qu & Zhang 2023). While birefringent dispersive delay would require  $RM \approx 10^7 \text{ rad m}^{-2}$  to produce the observed 0.3 ms split in FRB 20220310F, birefringent refraction may be more plausible, requiring only  $RM \approx 10^{1-2} \text{ rad m}^{-2}$ . The closed loop formed on the Poincaré sphere by the polarization vector of the second component of FRB 20220310F is also reminiscent of the loop observed in the first component of FRB 20181112A by Cho et al. (2020), which was potentially ascribed to FC in a relativistic plasma. From equation 2, we estimate a magnetic field strength  $B \approx 150 \text{ G}$  would be required for FC, which is inconsistent with supernova-remnant and plerionic environments (e.g. Vedantham & Ravi 2019).

### 3.3.3. *RM Variation*

We observe a significant  $3.1\sigma$  variation in RM between the sub-components of FRB 20221101B ( $-13.1 \pm 10.5 \text{ rad m}^{-2}$  and  $-75.9 \pm 17.5 \text{ rad m}^{-2}$ ), and marginally significant  $1.7\sigma$  and  $2.7\sigma$  variations in FRB 20220207C ( $161.5 \pm 0.4 \text{ rad m}^{-2}$  and  $173.5 \pm 7.2 \text{ rad m}^{-2}$ ) and FRB 20220310F ( $10.1 \pm 0.6 \text{ rad m}^{-2}$  and  $13.7 \pm 1.2 \text{ rad m}^{-2}$ ), respectively. Figures 21-24 in Appendix M show the evolution of detected RM across all four **Multi-Component** FRBs. No RM was detected for any but the strongest sub-component of FRB 20220418A, and intra-component RM variations were not observed for any other DSA-110 FRB. This effect is commonly observed in the APs of radio pulsars when sufficient S/N is available (Ilie et al. 2019), with magnitudes up to several tens of  $\text{rad m}^{-2}$ , and is attributed to propagation effects in pulsar magnetospheres (e.g., Yang et al. 2023, Section 4.3). Similar propagation effects, if responsible for the RM variations we observe, may also be responsible for the multiple emission components as we only observe these effects (and significant variations in polarization state) for the FRBs that exhibit sub-components.

## 4. COMPARISONS

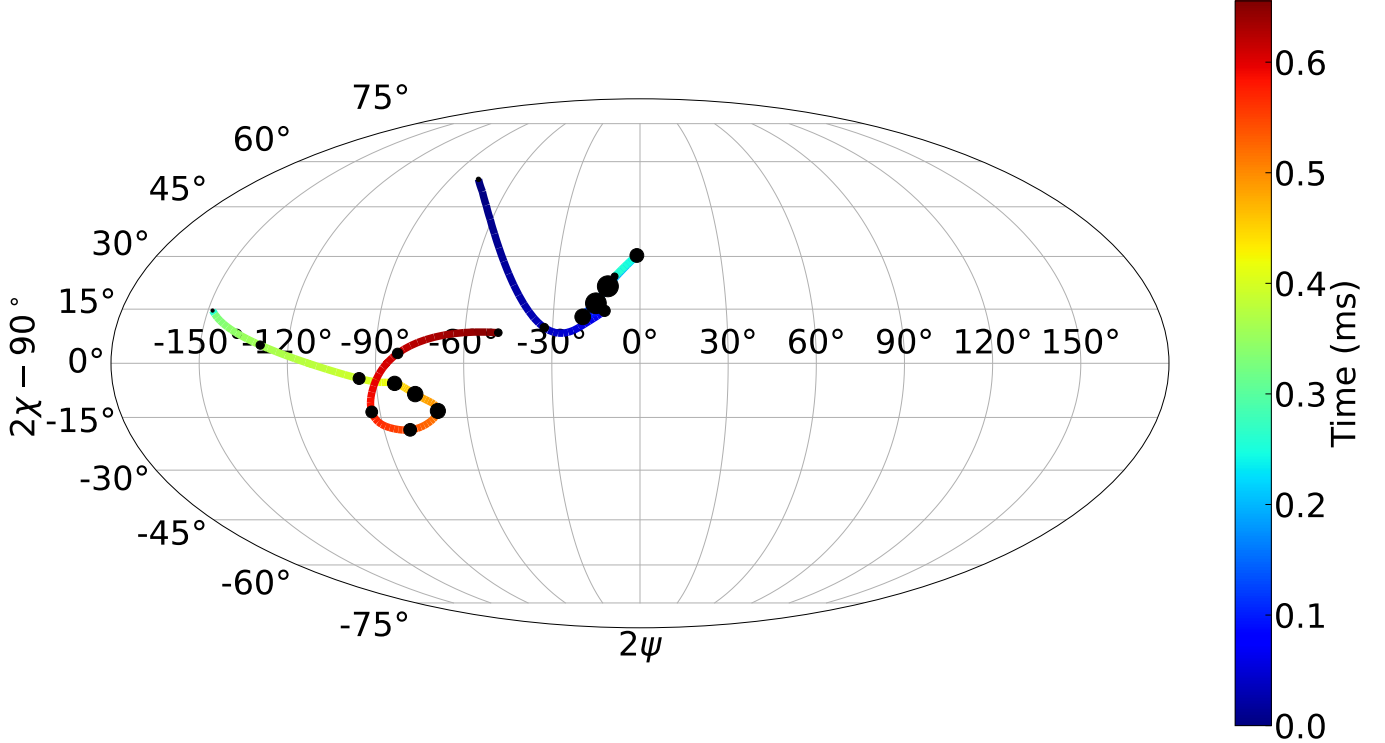


**Figure 4.** Projection of the polarization state of FRB 20220310F onto the Poincaré sphere. The position angle ( $\chi$ ) and longitude ( $\psi$ ) are related to the Stokes parameters by  $Q = \sin(2\psi) \sin(2\chi)$ ,  $U = \sin(2\psi) \cos(2\chi)$ , and  $V = \cos(2\psi)$ . Note the position angle axis has been shifted by  $90^\circ$  for ease of viewing. Data are displayed in windows of eight and ten  $32.768 \mu\text{s}$  samples for the first and second components of the burst.

The polarization properties of FRBs provide insight into the nature of FRB emission and FRB sources, as has been the case for pulsars. We therefore present comparisons between the polarization properties of FRB sub-samples, and between FRBs and Galactic pulsars, to search for similarities and differences. Although emission from FRBs and pulsars is vastly different in energy scale (e.g., Nimmo et al. 2021), common propagation effects in magnetospheres and near-source environments may impact the polarization properties. We augment the DSA-110 FRB sample with a literature sample of 38 FRB sources with polarization data, described in detail in Appendix A. The literature sample includes 19 repeating sources, for which we use the weighted mean of polarization measurements for the linear and circular fractions. When available, we use polarization measurements at L-band (1-2 GHz) for the literature sample in order to compare with the DSA-110 sample. A minimum  $S/N > 8\sigma$  is imposed on the literature sample of FRBs. For additional details, see Appendix A. The DSA-110 sample thus more than doubles the total number of non-repeating FRBs with polarization measurements. In Section 4.1 we compare properties of different FRB sub-samples, and assess any frequency dependent or other selection effects. We then compare FRB polarization properties with those of various subsets of the Galactic pulsar population in Section 4.2.

#### 4.1. Comparison between FRB sub-samples

In Figure 5 we compare the distributions of various FRB sub-samples in  $L/I$  and  $|V|/I$ . We consider the DSA-110 sample of 25 so far non-repeating events, along with published repeaters and non-repeaters, and measurements below 1 GHz. The literature sample contains 17 non-repeaters and

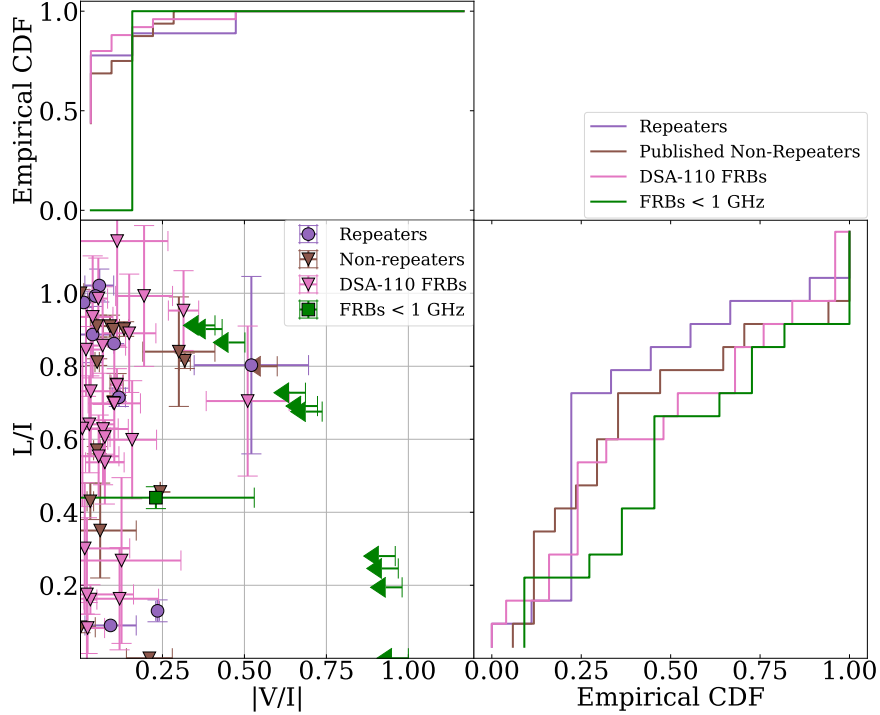


**Figure 5.** Comparison between the linear- and circular-polarization fractions of various FRB sub-samples. The top and right panels show empirical cumulative distribution functions (CDFs) for the DSA-110 sample (pink), published non-repeaters (brown), published repeaters (purple), and FRBs with measurements only at  $< 1$  GHz (green). Arrows indicate upper limits in  $|V/I|$  estimated from the measured values of  $L/I$ . See Appendix A for a summary of the literature data. In general, no significant differences between sub-samples are found.

9 repeaters with polarization measurements at L-band (1 - 2 GHz), while there are 10 repeaters and 1 non-repeater with measurements only at lower frequencies ( $< 1$  GHz). 6 repeaters have measurements at multiple frequencies, for which we use the L-band observations where available. 16 non-repeaters (1 below 1 GHz) and 8 repeaters (1 below 1 GHz) in the literature sample have circular polarization measurements. Kolmogorov-Smirnov (K-S) and Anderson-Darling (A-D) tests at 90% confidence (p-values below 10% reject the null hypothesis that the samples are drawn from the same distribution) reveal no significant differences in the distributions of DSA-110 and other FRBs in  $L/I$ . This holds when comparing with both previously published repeaters and non-repeaters, which themselves have no evident differences. We acknowledge however that this test is incomplete, and biases due to the resolution, sky coverage, and bandwidth of the DSA-110 survey may still exist. Further exploration of this however is outside the scope of this work, and we proceed on the assumption that such biases are negligible given the consistency of the DSA-110 sample with the published sample of FRBs.

A more detailed discussion is required to properly compare circular polarization. The circular polarization fraction can be defined either by averaging over the signed Stokes V fraction,  $V/I$ , or by taking the absolute value of Stokes V before averaging,  $|V|/I$ . The former preserves the sign (handedness) of circular polarization but neglects any significant sign changes across the burst. The latter accounts for sign changes, but introduces a bias which is not well-constrained. We provide both values for the DSA-110 bursts in Table 2, but most published FRBs use only  $V/I$  (e.g., Hilmarsson et al. 2021a; Cho et al. 2020). Therefore, we proceed by using  $V/I$  so that the sample is consistent,

taking the absolute value ( $|V/I|$ ) so that the already small sample is not further split by sign. With this definition, we find no significant difference when comparing the distribution of circular polarization of DSA-110 FRBs to previously detected non-repeaters. However, it is encouraged for future polarization surveys to report both  $V/I$  and  $|V/I|$ , as the latter is a more accurate representation of the magnitude of circular polarization. Furthermore,  $V/I$  and  $|V/I|$  cannot be accurately compared due to the bias in  $|V/I|$ . For example, using  $|V/I|$  for the DSA-110 sample and  $|V/I|$  for the published sample, we find significant difference between the populations with p-value 1.2%. We conclude that the DSA-110 sample is not biased in its polarization properties with respect to published FRBs, and that polarization fractions do not appear to be a viable means of distinguishing repeaters and non-repeaters (see also [Qu & Zhang 2023](#)).

We compare the sample of FRBs with polarization data at L-band to those measured at lower frequencies. No significant difference is found. This may suggest that other effects besides frequency-dependent stochastic RM depolarization ([Feng et al. 2022b](#); [Mckinven et al. 2023](#)) generally determine the polarization properties of the FRB population at different frequencies. Alternatively, if stochastic RM depolarization is dominant, this may imply that FRB progenitors can inhabit a wide variety of turbulent magneto-ionic environments. However, more robust conclusions would require a careful dissection of the population, for example into repeaters and non-repeaters; only two of the literature FRBs with polarization data reported below 1 GHz are apparent non-repeaters. We further note this method is primarily effective in characterizing the frequency-dependence of non-repeaters and repeaters detected in only one frequency band by analyzing the population as a whole. [Feng et al. \(2022b\)](#) and [Mckinven et al. \(2023\)](#) provide more detailed analyses of individual repeaters with measurements at multiple frequencies. For the remainder of the paper, we restrict the sample to the 18 non-repeaters and 9 repeaters with L-band polarization measurements.

#### 4.2. Comparison between FRBs and pulsars

We next compare the linear- and circular-polarization fractions of FRBs with the Galactic and Magellanic-Cloud pulsar populations. We include RRATs, noting that no circular polarization data are available for RRATs at the time of writing. Radio-loud magnetars are also included, and are grouped with Canonical Pulsars (CPs,  $P > 30$  ms) where necessary. We also consider both average-profile (AP) and single-pulse (SP) polarization fractions of pulsars.

Although the polarization properties of APs across the  $P - \dot{P}$  diagram are well characterized (see Appendix A for a summary of existing observations), only a few SP polarization studies of substantial pulsar samples exist (e.g., [Manchester et al. 1975](#); [Stinebring et al. 1984](#); [Mitra et al. 2016](#); [Mitra et al. 2023](#)). Among the non-recycled pulsar population, significant trends in SP and AP polarization are observed with the spin-down energy loss rate,  $\dot{E}$ . For high- $\dot{E}$  pulsars, both SPs and APs typically exhibit high polarization fractions, and valid rotating vector model (RVM; [Radhakrishnan & Cooke 1969](#)) fits can sometimes even be made to SPs. For lower- $\dot{E}$  pulsars, while SP polarization fractions remain high, AP polarization fractions decrease. The depolarization can have multiple causes: for example, a wider variance of polarization states of SPs, and SPs clustering into orthogonally polarized modes. These trends are driven by  $L/I$ ;  $|V/I|$  remains consistent with  $\dot{E}$  and between SPs and APs. Here we compare the FRB polarization fractions to a collation of AP polarization fractions obtained around 1.4 GHz from the literature, and to the polarization fractions of SPs obtained with the Meterwavelength Single-pulse Polarimetric Emission Survey (MSPES) at 333 MHz and 618 MHz. The results are shown in Figures 6 and 7.

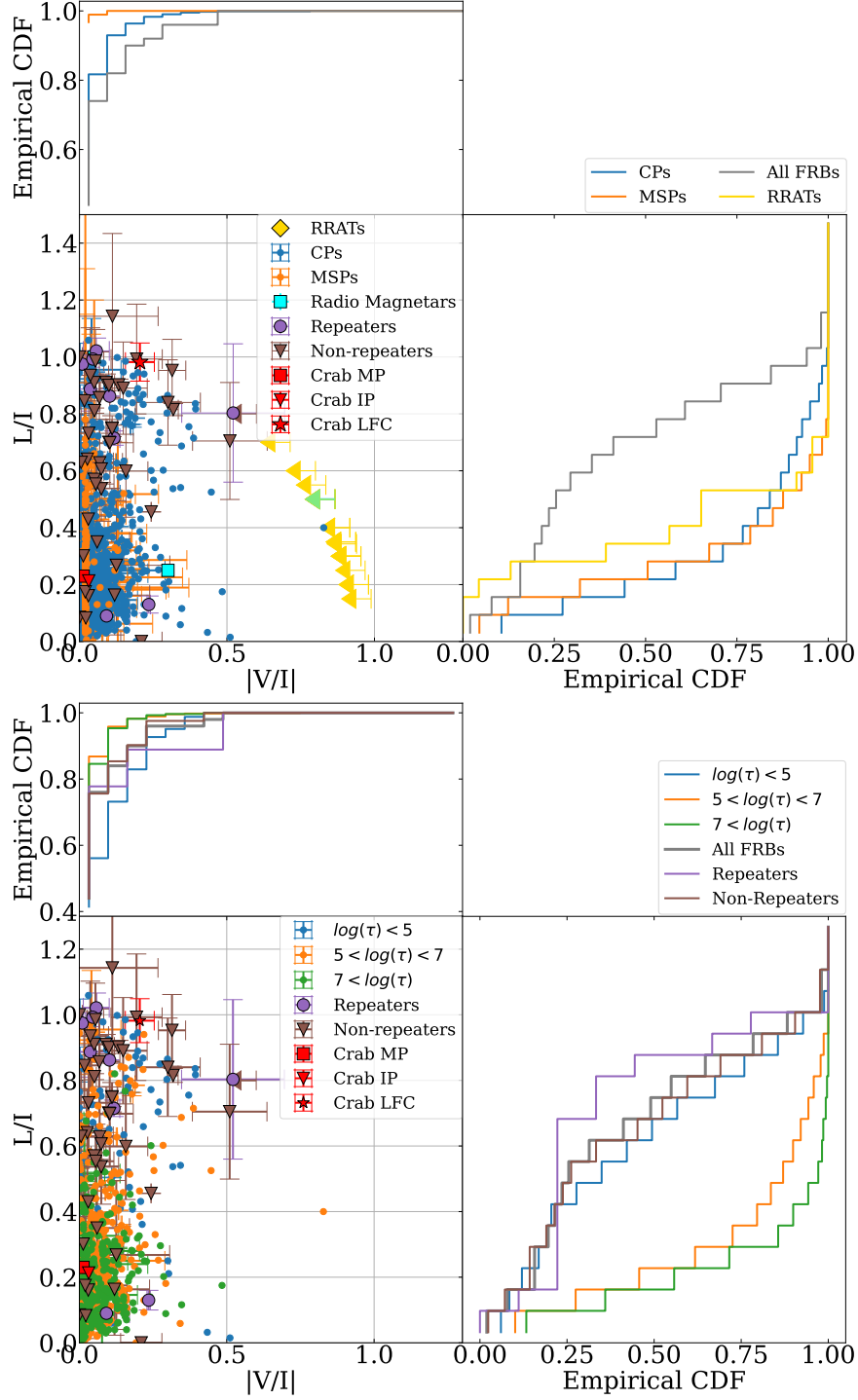


**Figure 6.** Comparison between the linear- and circular- polarization fractions of FRBs, pulsar APs, and RRATs. *Top:* FRBs (grey) are observed to have much higher linear-polarization fractions than MSPs (blue), CPs (orange) and RRATs (gold). Arrows indicate upper limits in  $|V/I|$  estimated from the measured values of  $L/I$ . Somewhat higher circular-polarization fractions are also observed for FRBs. *Bottom:* We compare FRBs with canonical pulsars ( $P > 30$  ms) with various characteristic ages. Young pulsars (blue) have remarkable similarity to FRBs (grey) in linear polarization, while older pulsars (orange, green) are more depolarized.

The distributions of polarization fractions of FRBs are largely dissimilar to those of pulsars. Pulsar APs and RRATs show characteristically smaller linear and circular polarization fractions than the FRB sample, both repeaters and non-repeaters. Of the 9 L-band repeaters we consider, only two have small ( $\lesssim 30\%$ )  $L/I$ , and the remainder have large ( $\gtrsim 70\%$ )  $L/I$ . Non-repeating FRBs have similar  $L/I$  and somewhat lower  $|V/I|$  than repeaters, though small number statistics may limit concrete statements regarding repeaters. Although RRATs have slightly higher  $L/I$  than pulsar APs, this difference is marginal in comparison to the FRB-AP difference. A KS test indicates that repeating FRBs, unlike the non-repeaters, are not significantly different from CPs in  $|V/I|$ . Although interpretation of this is limited by small-number statistics with only 7 repeaters with  $|V/I|$  measurements.

Remarkably, FRBs (in particular non-repeating sources) have similar distributions of  $L/I$  and  $|V|/I$  to the youngest (characteristic ages  $\tau_c < 10^5$  yr) pulsar APs. The polarization properties of young, high- $\dot{E}$  pulsars are known to be drastically different to the remainder of the pulsar population (Weltevrede & Johnston 2008), with high  $L/I$ , a lack of jumps in polarization position-angle and orthogonally polarized modes, and a close similarity between typical-SP and AP polarization profiles. The lack of depolarization in young pulsars is attributed to either magnetospheric propagation effects that cause only one of the modes (likely the  $O$ -mode) to be observed, or to the dominance of curvature radiation at high  $\dot{E}$  (resulting in  $\gamma$ -ray emission) that may change the radio emission mechanism. Young pulsars, with emission likely from high in the magnetosphere (Ravi et al. 2010), may prove to be useful analogs for the production of FRB radiation even if the specific radio emission mechanisms differ. As an example, we refer the reader to recent work by Lin et al. (2023) on the importance of both extreme emission heights and relativistic motion in giant pulses emitted by the Crab pulsar.

Finally, we find that the MSPES SP distributions of  $L/I$  and  $|V/I|$  are not consistent with the FRB distributions. The SP linear-polarization fractions are clustered around  $\sim 60\%$ , whereas the FRBs span a wider range of  $L/I$ . The SPs typically exhibit slightly higher values of  $|V/I|$  than FRBs. The MSPES sample only contains seven SP measurements for  $\dot{E} > 10^{34}$  ergs $^{-1}$ , a threshold above which significant polarization changes are observed.

## 5. CONCLUSIONS

We present a full-polarization analysis of the first 25 as yet non-repeating FRBs detected at 1.4 GHz with the DSA-110. This analysis includes a detailed description of data reduction and calibration for full-Stokes high time resolution data. We detect RMs for 20 FRBs, with magnitudes in the range  $4 - 4670$  rad m $^{-2}$ . We propose a classification according to polarization, S/N, and temporal properties. 15/25 DSA-110 FRBs are labeled as **Consistent with 100% Polarization**, 3/25 are labeled **Consistent with 0% Polarization**, 5/25 are **Intermediate**, and 2/25 have **Unconstrained** polarization properties due to their low S/N. Four FRBs that show multiple components on millisecond timescales are also unique in showing time-variable polarization properties, including RM.

We combine the DSA-110 sample with polarization measurements of previously published FRBs, and compare FRB sub-samples and FRBs with Galactic pulsars. We find no significant differences in the distributions of  $L/I$  and  $|V/I|$  between the DSA-110 sample and the published samples; neither is there a significant difference between the repeater and non-repeater samples. We find that FRBs are typically far more polarized than the average profiles of pulsars and span a wider range in polarization fractions than pulsar single pulses, which makes them remarkably similar to young (characteristic ages  $< 10^5$  yr) pulsars.

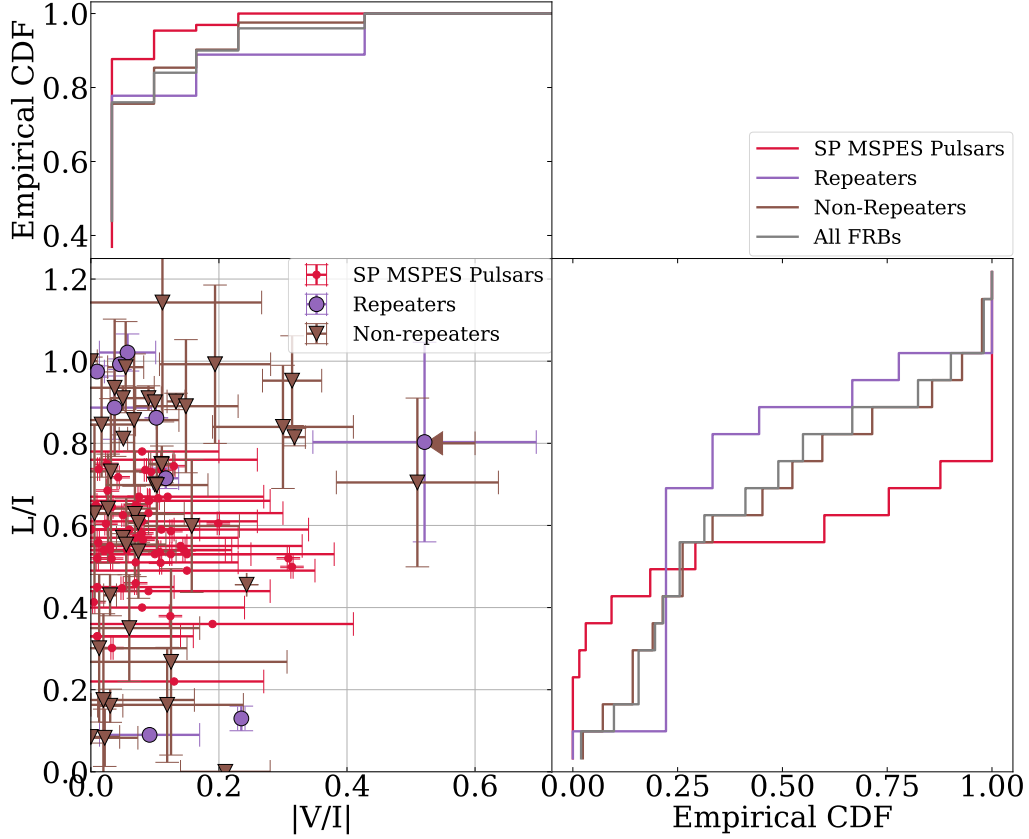


**Figure 7.** Comparison between the linear- and circular- polarization fractions of FRBs with pulsar single pulses (SPs). Pulsar SPs (red) have similar average linear polarization fraction ( $\sim 60\%$ ), but cover a narrower range than FRBs (grey). Arrows indicate upper limits in  $|V/I|$  estimated from the measured values of  $L/I$ .

We conclude the following.

1. The substantial fraction of highly linearly polarized FRBs (15/25 in the DSA-110 sample are **Consistent with 100%** and have  $L/I > 50\%$ ) suggests that the FRB emission mechanism is often intrinsically linearly polarized. In the full DSA-110 sample, statistically significant variations in PPA are observed in 3/25 events (2/13 **Consistent with 100%** events). This suggests modulation in some cases caused by a rapidly moving / rotating emission region.
2. Bursts with temporally separated components have variable polarization properties between the components. Of the 4/25 such DSA-110 events, three have variable linear-polarization PPAs and fractions, two have variable signs and magnitudes of Stokes V, and three exhibit evidence for time-variable RMs. Together this suggests that the emission sites responsible for the different components originate from different regions of a magnetosphere, and are potentially viewed along different sightlines through magnetized plasma.
3. The origins of circular polarization and depolarization in FRBs remain mysterious. Faraday conversion in a highly magnetized near-source medium could explain the observed  $|V|/I$  fractions. We disfavor bandwidth depolarization, RM scattering, and Faraday conversion as dominant depolarization mechanisms. We therefore have little evidence from polarimetry alone

for the generic presence of dense, highly magnetized, inhomogeneous near-source plasma environments. Depolarization due to the superposition of multiple short bursts is possible.

4. The strong similarity between the  $L/I$  distributions of FRBs and the average profiles (and likely also single pulses) of the youngest pulsars suggests that the radio emission from young pulsars may form a useful analog to probe at least the depolarization mechanisms of FRBs. We note that the abrupt jump in PA observed in FRB 20220207C and the near-orthogonal positions on the Poincaré sphere of the two components of FRB 20220310F are uncommon for young pulsars.

Polarization studies have great promise in identifying characteristics of FRB emission that may prove useful in testing emission-mechanism and progenitor models. At present, intrinsic emission-mechanism models favor high linear-polarization fractions, thus ascribing all other properties to propagation effects. In the future, studying FRB polarization properties in the context of other diagnostics of near-source environments, e.g., from accurate localizations, may be used to distinguish between intrinsic and extrinsic effects. At this point, we urge the further theoretical consideration of the intrinsic timescale(s) of FRB emission, and the causes of intrinsic depolarization. First, several of the DSA-110 FRBs are remarkably simple: the sample is characterized (21/25 events) by single emission components that are several tenths of a millisecond wide, with flat PPAs, and a wide range of linear-polarization fractions. We suggest that depolarization is likely intrinsic to the emission rather than a propagation effect; thus, the prospect of superposing several shorter bursts needs to be considered. At the same time, the existence of highly linearly polarized FRBs with flat PPAs over approx. millisecond timescales also requires an explanation. While not explored in this work, the scattering of FRBs over millisecond durations could be an alternate cause of flat PPAs. Third, our finding that multiple temporally separated emission components on approx. millisecond timescales tend to have different polarization properties poses an interesting additional challenge.

1 The authors would like to thank Jim Cordes, Dongzhi Li, Bing Zhang, Yuanhong Qu, Joel Weis-  
 2 berg, and Alexandra Mannings, for insightful and essential conversations on polarization theory and  
 3 direction on the analysis conducted, as well as Paul Bellan and Yang Zhang for a comprehensive  
 4 Plasma Physics course. We also thank Yi Feng, Dipanjan Mitra, Yuan-Pei Yang, Dylan Nelson,  
 5 Reshma Anna-Thomas, and an anonymous referee for useful comments and recommendations on  
 6 the early draft. This material is based upon work supported by the National Science Foundation  
 7 Graduate Research Fellowship under Grant No. DGE-1745301. The authors thank staff members  
 8 of the Owens Valley Radio Observatory and the Caltech radio group, including Kristen Bernasconi,  
 9 Stephanie Cha-Ramos, Sarah Harnach, Tom Klinefelter, Lori McGraw, Corey Posner, Andres Rizo,  
 10 Michael Virgin, Scott White, and Thomas Zentmyer. Their tireless efforts were instrumental to the  
 11 success of the DSA-110. The DSA-110 is supported by the National Science Foundation Mid-Scale  
 12 Innovations Program in Astronomical Sciences (MSIP) under grant AST-1836018.

## REFERENCES

- |  |   |
|--|---|
| <p>Amiri, M., Andersen, B. C., Bandura, K., et al.<br/>     2021, <i>The Astrophysical Journal Supplement</i><br/>     Series, 257, 59, doi: <a href="https://doi.org/10.3847/1538-4365/ac33ab">10.3847/1538-4365/ac33ab</a></p> | <p>Andersen, B., Bandura, K., Bhardwaj, M., et al.<br/>     2019, <i>The Astrophysical Journal Letters</i>, 885,<br/>     L24</p> |
|--|---|

- Anna-Thomas, R., Connor, L., Dai, S., et al. 2023a, *Science*, 380, 599
- . 2023b, Magnetic field reversal in the turbulent environment around a repeating fast radio burst. <https://arxiv.org/abs/2202.11112>
- Bannister, K. W., Deller, A. T., Phillips, C., et al. 2019, *Science*, 365, 565
- Beloborodov, A. M. 2021, *The Astrophysical Journal Letters*, 922, L7
- Beniamini, P., Kumar, P., & Narayan, R. 2022, *Monthly Notices of the Royal Astronomical Society*, 510, 4654
- Beniamini, P., Wadiasingh, Z., & Metzger, B. D. 2020, *Monthly Notices of the Royal Astronomical Society*, 496, 3390
- Bhandari, S., Keane, E., Barr, E., et al. 2018, *Monthly Notices of the Royal Astronomical Society*, 475, 1427
- Bhandari, S., Bannister, K. W., Lenc, E., et al. 2020, *The Astrophysical Journal Letters*, 901, L20
- Bhandari, S., Gordon, A. C., Scott, D. R., et al. 2023, *ApJ*, 948, 67, doi: [10.3847/1538-4357/acc178](https://doi.org/10.3847/1538-4357/acc178)
- Bhardwaj, M., Gaensler, B., Kaspi, V., et al. 2021, *The Astrophysical Journal Letters*, 910, L18
- Brentjens, M. A., & De Bruyn, A. 2005, *Astronomy & Astrophysics*, 441, 1217
- Burke, B. F., Graham-Smith, F., & Wilkinson, P. N. 2019, *An introduction to radio astronomy* (Cambridge University Press)
- Burn, B. 1966, *Monthly Notices of the Royal Astronomical Society*, 133, 67
- Caleb, M., Keane, E., Van Straten, W., et al. 2018, *Monthly Notices of the Royal Astronomical Society*, 478, 2046
- Caleb, M., van Straten, W., Keane, E., et al. 2019, *Monthly Notices of the Royal Astronomical Society*, 487, 1191
- Cameron, A. D., Li, D., Hobbs, G., et al. 2020, *Monthly Notices of the Royal Astronomical Society*, 495, 3515
- Camilo, F., Reynolds, J., Johnston, S., Halpern, J., & Ransom, S. 2008, *The Astrophysical Journal*, 679, 681
- Camilo, F., Reynolds, J., Johnston, S., et al. 2007, *The Astrophysical Journal*, 659, L37
- Chatterjee, S., Law, C. J., Wharton, R. S., et al. 2017, *Nature*, 541, 58, doi: [10.1038/nature20797](https://doi.org/10.1038/nature20797)
- Cho, H., Macquart, J.-P., Shannon, R. M., et al. 2020, *The Astrophysical Journal Letters*, 891, L38
- Condon, J. J., & Ransom, S. M. 2016, *Essential radio astronomy*, Vol. 2 (Princeton University Press)
- Connor, L., van Leeuwen, J., Oostrum, L., et al. 2020, *Monthly Notices of the Royal Astronomical Society*, 499, 4716
- Cordes, J. 1976, *The Astrophysical Journal*, 210, 780
- Day, C. K., Deller, A. T., Shannon, R. M., et al. 2020, *MNRAS*, 497, 3335, doi: [10.1093/mnras/staa2138](https://doi.org/10.1093/mnras/staa2138)
- Everett, J., & Weisberg, J. 2001, *The Astrophysical Journal*, 553, 341
- Falcke, H., & Rezzolla, L. 2014, *A&A*, 562, A137, doi: [10.1051/0004-6361/201321996](https://doi.org/10.1051/0004-6361/201321996)
- Feng, Y., Zhang, Y.-K., Li, D., et al. 2022a, arXiv preprint arXiv:2212.05873
- Feng, Y., Li, D., Yang, Y.-P., et al. 2022b, *Science*, 375, 1266
- Fonseca, E., Andersen, B., Bhardwaj, M., et al. 2020, *The Astrophysical Journal Letters*, 891, L6
- Gordon, A. C., Fong, W.-f., Kilpatrick, C. D., et al. 2023, arXiv e-prints, arXiv:2302.05465, doi: [10.48550/arXiv.2302.05465](https://doi.org/10.48550/arXiv.2302.05465)
- Gould, D., & Lyne, A. 1998, *Monthly Notices of the Royal Astronomical Society*, 301, 235
- Gruzinov, A., & Levin, Y. 2019, *The Astrophysical Journal*, 876, 74
- Gu, W.-M., Dong, Y.-Z., Liu, T., Ma, R., & Wang, J. 2016, *ApJL*, 823, L28, doi: [10.3847/2041-8205/823/2/L28](https://doi.org/10.3847/2041-8205/823/2/L28)
- Han, J. L., Manchester, R. N., Xu, R. X., & Qiao, G. J. 1998, *MNRAS*, 300, 373, doi: [10.1046/j.1365-8711.1998.01869.x](https://doi.org/10.1046/j.1365-8711.1998.01869.x)
- Hankins, T., Kern, J., Weatherall, J., & Eilek, J. 2003, *Nature*, 422, 141
- Heald, G. 2008, *Proceedings of the International Astronomical Union*, 4, 591–602, doi: [10.1017/S1743921309031421](https://doi.org/10.1017/S1743921309031421)
- Heiles, C., Perillat, P., Nolan, M., et al. 2001, *Publications of the Astronomical Society of the Pacific*, 113, 1274
- Hewitt, D. M., Hessels, J. W. T., Ould-Boukattine, O. S., et al. 2023, *MNRAS*, 526, 2039, doi: [10.1093/mnras/stad2847](https://doi.org/10.1093/mnras/stad2847)

- Hilmarsson, G., Spitler, L., Main, R., & Li, D. 2021a, *Monthly Notices of the Royal Astronomical Society*, 508, 5354
- Hilmarsson, G., Michilli, D., Spitler, L., et al. 2021b, *The Astrophysical Journal Letters*, 908, L10
- Ilie, C. D., Johnston, S., & Weltevrede, P. 2019, *MNRAS*, 483, 2778, doi: [10.1093/mnras/sty3315](https://doi.org/10.1093/mnras/sty3315)
- Jiang, J.-C., Wang, W.-Y., Xu, H., et al. 2022, *Research in Astronomy and Astrophysics*, 22, 124003
- Johnston, S., & Kerr, M. 2018, *Monthly Notices of the Royal Astronomical Society*, 474, 4629
- Johnston, S., & Kramer, M. 2019, *MNRAS*, 490, 4565, doi: [10.1093/mnras/stz2865](https://doi.org/10.1093/mnras/stz2865)
- Johnston, S., Parthasarathy, A., Main, R., et al. 2022, *Monthly Notices of the Royal Astronomical Society*, 509, 5209
- Karastergiou, A., Hotan, A., Van Straten, W., McLaughlin, M., & Ord, S. 2009, *Monthly Notices of the Royal Astronomical Society: Letters*, 396, L95
- Keane, E., Johnston, S., Bhandari, S., et al. 2016, *Nature*, 530, 453
- Keane, E. F., McLaughlin, M. A., & . 2011, *Rotating Radio Transients*. <https://arxiv.org/abs/1109.6896>
- Kirsten, F., Marcote, B., Nimmo, K., et al. 2022, *Nature*, 602, 585, doi: [10.1038/s41586-021-04354-w](https://doi.org/10.1038/s41586-021-04354-w)
- Kirsten, F., Ould-Boukattine, O., Herrmann, W., et al. 2023, *arXiv e-prints*, arXiv:2306.15505, doi: [10.48550/arXiv.2306.15505](https://doi.org/10.48550/arXiv.2306.15505)
- Kramer, M., Stappers, B., Jessner, A., Lyne, A., & Jordan, C. 2007, *Monthly Notices of the Royal Astronomical Society*, 377, 107
- Kumar, P., Shannon, R. M., Lower, M. E., et al. 2022, *Monthly Notices of the Royal Astronomical Society*, 512, 3400
- Kumar, P., Luo, R., Price, D. C., et al. 2023, *arXiv preprint arXiv:2304.01763*
- Law, C. J., Sharma, K., Ravi, V., et al. 2023, *arXiv e-prints*, arXiv:2307.03344, doi: [10.48550/arXiv.2307.03344](https://doi.org/10.48550/arXiv.2307.03344)
- Levin, L., Bailes, M., Bates, S., et al. 2010, *The Astrophysical Journal Letters*, 721, L33
- . 2012, *Monthly Notices of the Royal Astronomical Society*, 422, 2489
- Li, C., Lin, L., Xiong, S., et al. 2021, *Nature Astronomy*, 5, 378
- Li, D., Bilous, A., Ransom, S., Main, R., & Yang, Y.-P. 2022, *arXiv preprint arXiv:2205.07917*
- Li, D., Bilous, A., Ransom, S., Main, R., & Yang, Y.-P. 2023, *Nature*, 618, 484, doi: [10.1038/s41586-023-05983-z](https://doi.org/10.1038/s41586-023-05983-z)
- Lin, R., van Kerkwijk, M. H., Main, R., et al. 2023, *ApJ*, 945, 115, doi: [10.3847/1538-4357/acba95](https://doi.org/10.3847/1538-4357/acba95)
- Lorimer, D. R. 2008, *Living reviews in relativity*, 11, 1
- Luan, J., & Goldreich, P. 2014, *ApJL*, 785, L26, doi: [10.1088/2041-8205/785/2/L26](https://doi.org/10.1088/2041-8205/785/2/L26)
- Luo, R., Wang, B., Men, Y., et al. 2020, *Nature*, 586, 693
- Lyubarsky, Y. 2014, *Monthly Notices of the Royal Astronomical Society: Letters*, 442, L9
- Macquart, J.-P., Prochaska, J., McQuinn, M., et al. 2020, *Nature*, 581, 391
- Majid, W. A., Pearlman, A. B., Prince, T. A., et al. 2021, *ApJL*, 919, L6, doi: [10.3847/2041-8213/ac1921](https://doi.org/10.3847/2041-8213/ac1921)
- Manchester, R. N. 1971, *Astrophysical Journal Supplement*, vol. 23, p. 283 (1971), 23, 283
- Manchester, R. N., Taylor, J. H., & Huguenin, G. R. 1973, *ApJL*, 179, L7, doi: [10.1086/181105](https://doi.org/10.1086/181105)
- . 1975, *ApJ*, 196, 83, doi: [10.1086/153395](https://doi.org/10.1086/153395)
- Mannings, A. G., Fong, W.-f., Simha, S., et al. 2021, *The Astrophysical Journal*, 917, 75
- Mannings, A. G., Pakmor, R., Prochaska, J. X., et al. 2022, *arXiv preprint arXiv:2209.15113*
- Mardia, K. V. 1972, *Statistics of directional data.*, *Probability and mathematical statistics* (Academic Press). <https://search.ebscohost.com/login.aspx?direct=true&AuthType=ip,sso&db=catalog09073a&AN=cit.oai.edge.caltech.folio.ebsco.com.fs00001057.73b39503.802d.4a13.939f.ea01212e06c5&site=eds-live&scope=site&custid=s8984125>
- Mardia, K. V., & Jupp, P. E. 2000, *Directional statistics.*, *Wiley series in probability and statistics* (J. Wiley). <https://search.ebscohost.com/login.aspx?direct=true&AuthType=ip,sso&db=catalog09073a&AN=cit.oai.edge.caltech.folio.ebsco.com.fs00001057.7399d9f8.d802.4ce0.8701.5afe7b791172&site=eds-live&scope=site&custid=s8984125>

- Mardia, K. V., & Zemroch, P. J. 1975a, *Journal of the Royal Statistical Society. Series C (Applied Statistics)*, 24, 268.  
<http://www.jstor.org/stable/2346578>
- . 1975b, *Journal of the Royal Statistical Society. Series C (Applied Statistics)*, 24, 147.  
<http://www.jstor.org/stable/2346721>
- Masui, K., Lin, H.-H., Sievers, J., et al. 2015, *Nature*, 528, 523
- Mckinven, R. 2022, PhD thesis, University of Toronto (Canada)
- McKinven, R., & Chime/Frb Collaboration. 2022, *The Astronomer's Telegram*, 15679, 1
- Mckinven, R., Michilli, D., Masui, K., et al. 2021, *The Astrophysical Journal*, 920, 138
- Mckinven, R., Gaensler, B., Michilli, D., et al. 2023, arXiv preprint arXiv:2302.08386
- Melrose, D., & Macquart, J.-P. 1998, *The Astrophysical Journal*, 505, 921
- Metzger, B. D., Margalit, B., & Sironi, L. 2019, *MNRAS*, 485, 4091, doi: [10.1093/mnras/stz700](https://doi.org/10.1093/mnras/stz700)
- Metzger, B. D., Margalit, B., & Sironi, L. 2019, *Monthly Notices of the Royal Astronomical Society*, 485, 4091
- Michilli, D., Seymour, A., Hessels, J., et al. 2018, *Nature*, 553, 182
- Mitra, D., Arjunwadkar, M., & Rankin, J. M. 2015, *The Astrophysical Journal*, 806, 236
- Mitra, D., Basu, R., Maciesiak, K., et al. 2016, *The Astrophysical Journal*, 833, 28
- Mitra, D., Melikidze, G. I., & Basu, R. 2023, arXiv e-prints, arXiv:2306.02537, doi: [10.48550/arXiv.2306.02537](https://doi.org/10.48550/arXiv.2306.02537)
- Morrell, T. E., & Law, C. J. 2022, DSA-110 Event Archive, 0.0.1.  
<https://github.com/dsa110/dsa110-archive>
- Naghizadeh-Khouei, J., & Clarke, D. 1993, *Astronomy and Astrophysics*, Vol. 274, p. 968 (1993), 274, 968
- Nimmo, K., Hessels, J., Keimpema, A., et al. 2021, *Nature Astronomy*, 5, 594
- Nimmo, K., Hessels, J., Kirsten, F., et al. 2022, *Nature Astronomy*, 6, 393
- Olszanski, T. E., Mitra, D., & Rankin, J. M. 2019, *Monthly Notices of the Royal Astronomical Society*, 489, 1543
- Oslowski, S., Shannon, R., Ravi, V., et al. 2019, *Monthly Notices of the Royal Astronomical Society*, 488, 868
- Oswald, L. S., Karastergiou, A., & Johnston, S. 2023, *MNRAS*, doi: [10.1093/mnras/stad2271](https://doi.org/10.1093/mnras/stad2271)
- Pastor-Marazuela, I., van Leeuwen, J., Bilous, A., et al. 2022, arXiv preprint arXiv:2202.08002
- Perley, R. A., & Butler, B. J. 2013, *The Astrophysical Journal Supplement Series*, 206, 16, doi: [10.1088/0067-0049/206/2/16](https://doi.org/10.1088/0067-0049/206/2/16)
- . 2017, *The Astrophysical Journal Supplement Series*, 230, 7
- Petroff, E. 2017, arXiv preprint arXiv:1709.02189
- Petroff, E., & Yaron, O. 2020, *Transient Name Server AstroNote*, 160, 1
- Petroff, E., Bailes, M., Barr, E., et al. 2015, *Monthly Notices of the Royal Astronomical Society*, 447, 246
- Petroff, E., Barr, E., Jameson, A., et al. 2016, arXiv preprint arXiv:1601.03547
- Petroff, E., Burke-Spolaor, S., Keane, E., et al. 2017, *Monthly Notices of the Royal Astronomical Society*, 469, 4465
- Plavin, A., Paragi, Z., Marcote, B., et al. 2022, *Monthly Notices of the Royal Astronomical Society*, 511, 6033
- Pleunis, Z., Good, D. C., Kaspi, V. M., et al. 2021, *The Astrophysical Journal*, 923, 1
- Prochaska, J. X., Macquart, J.-P., McQuinn, M., et al. 2019, *Science*, 366, 231
- Purcell, C. R., Van Eck, C. L., West, J., Sun, X. H., & Gaensler, B. M. 2020, RM-Tools: Rotation measure (RM) synthesis and Stokes QU-fitting, *Astrophysics Source Code Library*, record ascl:2005.003. <http://ascl.net/2005.003>
- Qu, Y., & Zhang, B. 2023, arXiv preprint arXiv:2302.09697
- Radhakrishnan, V., & Cooke, D. J. 1969, *Astrophys. Lett.*, 3, 225
- Radhakrishnan, V., & Rankin, J. M. 1990, *ApJ*, 352, 258, doi: [10.1086/168531](https://doi.org/10.1086/168531)
- Rao, J. S. 1972, *Zeitschrift für Wahrscheinlichkeitstheorie und Verwandte Gebiete*, 22, 33 .  
<https://search.ebscohost.com/login.aspx?direct=true&AuthType=ip,sso&db=edsajs&AN=edsajs.DCE18EFE&site=eds-live&scope=site&custid=s8984125>
- Ravi, V., & Lasky, P. D. 2016, arXiv e-prints, arXiv:1601.06131, doi: [10.48550/arXiv.1601.06131](https://doi.org/10.48550/arXiv.1601.06131)

- Ravi, V., Manchester, R. N., & Hobbs, G. 2010, *ApJL*, 716, L85, doi: [10.1088/2041-8205/716/1/L85](https://doi.org/10.1088/2041-8205/716/1/L85)
- Ravi, V., Shannon, R., Bailes, M., et al. 2016, *Science*, 354, 1249
- Ravi, V., Catha, M., Chen, G., et al. 2022, Deep Synoptic Array science I: discovery of the host galaxy of FRB 20220912A. <https://arxiv.org/abs/2211.09049>
- . 2023, arXiv preprint arXiv:2301.01000
- Robishaw, T., & Heiles, C. 2021, in *The WSPC Handbook of Astronomical Instrumentation (WORLD SCIENTIFIC)*, 127–158, doi: [10.1142/9789811203770\\_0006](https://doi.org/10.1142/9789811203770_0006)
- Roy, J., Chengalur, J. N., & Pen, U.-L. 2018, *ApJ*, 864, 160, doi: [10.3847/1538-4357/aad815](https://doi.org/10.3847/1538-4357/aad815)
- Schnitzeler, D., & Lee, K. 2015, *Monthly Notices of the Royal Astronomical Society: Letters*, 447, L26
- Serylak, M., Johnston, S., Kramer, M., et al. 2021, *Monthly Notices of the Royal Astronomical Society*, 505, 4483
- Sharma, K., Somalwar, J., Law, C., et al. 2023, *ApJ*, 950, 175, doi: [10.3847/1538-4357/acf1d](https://doi.org/10.3847/1538-4357/acf1d)
- Sherman, M. B., Connor, L., Ravi, V., et al. 2023, *The Astrophysical Journal Letters*, 957, L8
- Simmons, J., & Stewart, B. 1985, *Astronomy and Astrophysics*, 142, 100
- Spiewak, R., Bailes, M., Miles, M. T., et al. 2022, *Publications of the Astronomical Society of Australia*, 39, doi: [10.1017/pasa.2022.19](https://doi.org/10.1017/pasa.2022.19)
- Stinebring, D. R., Cordes, J. M., Rankin, J. M., Weisberg, J. M., & Boriakoff, V. 1984, *ApJS*, 55, 247, doi: [10.1086/190954](https://doi.org/10.1086/190954)
- Suresh, A., & Cordes, J. M. 2019, *The Astrophysical Journal*, 870, 29
- Thompson, A. R., Moran, J. M., & Swenson, G. W. 2017, *Interferometry and synthesis in radio astronomy (Springer Nature)*
- Totani, T. 2013, *PASJ*, 65, L12, doi: [10.1093/pasj/65.5.L12](https://doi.org/10.1093/pasj/65.5.L12)
- van Leeuwen, J., Kooistra, E., Oostrum, L., et al. 2022, arXiv preprint arXiv:2205.12362
- Van Straten, W., Manchester, R., Johnston, S., & Reynolds, J. 2010, *Publications of the Astronomical Society of Australia*, 27, 104
- Vedantham, H., & Ravi, V. 2019, *Monthly Notices of the Royal Astronomical Society: Letters*, 485, L78
- Wahl, H., McLaughlin, M., Gentile, P., et al. 2022, *The Astrophysical Journal*, 926, 168
- Wang, W.-Y., Jiang, J.-C., Lee, K., Xu, R., & Zhang, B. 2022a, *Monthly Notices of the Royal Astronomical Society*, 517, 5080
- Wang, W.-Y., Yang, Y.-P., Niu, C.-H., Xu, R., & Zhang, B. 2022b, *The Astrophysical Journal*, 927, 105
- Weisberg, J., Cordes, J., Lundgren, S., et al. 1999, *The Astrophysical Journal Supplement Series*, 121, 171
- Weisberg, J. M., Cordes, J. M., Lundgren, S. C., et al. 1999, *ApJS*, 121, 171, doi: [10.1086/313189](https://doi.org/10.1086/313189)
- Weltevrede, P., & Johnston, S. 2008, *Monthly Notices of the Royal Astronomical Society*, 391, 1210
- Xie, J., Wang, J., Wang, N., et al. 2022, *The Astrophysical Journal Letters*, 940, L21
- Xu, H., Niu, J. R., Chen, P., et al. 2022, *Nature*, 609, 685, doi: [10.1038/s41586-022-05071-8](https://doi.org/10.1038/s41586-022-05071-8)
- Xu, H., Niu, J., Chen, P., et al. 2022, *Nature*, 609, 685
- Yan, W. M., Manchester, R. N., van Straten, W., et al. 2011, *MNRAS*, 414, 2087, doi: [10.1111/j.1365-2966.2011.18522.x](https://doi.org/10.1111/j.1365-2966.2011.18522.x)
- Yang, Y.-P., Lu, W., Feng, Y., Zhang, B., & Li, D. 2022, *ApJL*, 928, L16, doi: [10.3847/2041-8213/ac5f46](https://doi.org/10.3847/2041-8213/ac5f46)
- Yang, Y.-P., Xu, S., & Zhang, B. 2023, *MNRAS*, 520, 2039, doi: [10.1093/mnras/stad168](https://doi.org/10.1093/mnras/stad168)
- Zhang, B. 2022a, arXiv preprint arXiv:2212.03972
- . 2022b, *The Astrophysical Journal*, 925, 53, doi: [10.3847/1538-4357/ac3979](https://doi.org/10.3847/1538-4357/ac3979)
- Zhang, Y.-K., Li, D., Zhang, B., et al. 2023, *ApJ*, 955, 142, doi: [10.3847/1538-4357/aced0b](https://doi.org/10.3847/1538-4357/aced0b)

## APPENDIX

## A. LITERATURE SAMPLES OF POLARIZATION OBSERVATIONS OF FRBS AND PULSARS

Previous analyses have yielded either RM or polarization measurements for at least 38 FRBs at time of writing; this sample was compiled using the Transient Name Server<sup>12</sup> (TNS), the FRB Catalog<sup>13</sup> (FRBcat), and the Canadian Hydrogen Intensity Mapping Experiment (CHIME) FRB Catalog 1<sup>14</sup> (Petroff & Yaron (2020), (Petroff et al. 2016; Amiri et al. 2021)). FRB polarization is often reported without uncertainties due to low resolution or low S/N that makes constraining the polarization difficult. In addition there is no standard method of computing the polarization fraction due to the wide range of morphologies in FRBs, and this should be held in mind when comparing polarimetry from multiple surveys. The FRBs in the literature sample compiled here were detected through the Apertif survey with the Westerbork Synthesis Radio Telescope (WSRT) and the Australian Square Kilometer Array Pathfinder (ASKAP) survey, as well as observations with the Parkes Telescope, CHIME, Green Bank Telescope, and Arecibo Observatory. Recent studies have observed frequency-dependent de-polarization thought to be the result of stochastic RM variations within a scattering screen (Feng et al. 2022b; Mckinven et al. 2023). A subset of 11 FRBs in this sample have polarization measurements at lower ( $< 1$  GHz) frequencies.

Table 4 summarizes the polarization properties of each burst from the literature. Of the 38 bursts, 19 are repeaters, 34 have RM measurements, 15 have spectroscopic or photometric redshift measurements (9 repeaters, 6 non-repeaters), 25 have reported L-band linear polarization measurements, 11 have linear polarization measurements below 1 GHz, and 26 have reported circular polarization measurements. Below we describe the selection criteria and process for the FRB RMs used here:

1. Only RM measurements published before a 2023 April 10 cutoff date are considered for this sample.
2. For non-repeaters and repeaters with only 1 RM measurement, we use the available measurement.
3. For FRBs with RM measurements in the TNS or FRBcat databases, we defer to the catalogued value to maximize sample consistency.
4. For repeaters with multiple RM measurements, we use the weighted mean, with the reciprocal of the errors as weights.

We make three exceptions based on the observed RM behavior:

- FRB 20190208A shows a secular evolution in RM which follows a ‘U’ shaped curve (Mckinven et al. 2023). Therefore, we use the most recent RM value rather than the weighted mean.
- FRB 20190231B has multiple RM measurements from Mckinven et al. (2023); however, CHIME reports difficulty in distinguishing RM detections near 0 from instrumental leakage. Therefore,

<sup>12</sup> <https://www.wis-tns.org/>

<sup>13</sup> <https://www.frbcat.org/>

<sup>14</sup> <https://www.chime-frb.ca/catalog>

we use the RM measurement with the lowest uncertainty to minimize propagation of any leakage errors.

- FRB 20191117A has 2 RM measurements from [Mckinven et al. \(2023\)](#) separated by  $\sim 9 \text{ rad m}^{-2}$ , but it is unclear with only 2 bursts whether this variation is stochastic or secular. Therefore, we use the value with the smallest error to avoid improperly combining secularly evolved RMs.

We make three additional exceptions based on the conventions in the available literature; in cases where RM measurements are commonly compared to a well-constrained ‘accepted’ value which has not yet been superseded in accuracy, we use this accepted value. This affects the following FRBs:

- FRB 20121102A (e.g., [Plavin et al. 2022](#); [Michilli et al. 2018](#); [Hilmarsson et al. 2021b](#)); the value from [Plavin et al. \(2022\)](#) is used as it pre-dates other RM measurements and has a low relative error. However, since [Sherman et al. \(2023\)](#) compares the logarithm of the RM, deviations of the RM within an order of magnitude make little change to the analysis, and do not affect the analysis in this paper at all.
- FRB 20200120E (e.g., [Bhardwaj et al. 2021](#); [Nimmo et al. 2021](#)); we use the value from the first detected burst in [Bhardwaj et al. \(2021\)](#).
- FRB 20201124A (e.g., [Hilmarsson et al. 2021a](#); [Kumar et al. 2022](#)) we use the weighted mean value from [Hilmarsson et al. \(2021a\)](#)

We acknowledge that these constraints are not complete; secularly time-varying RMs are not properly represented either by the weighted mean or the value with the lowest error. In addition, while the weighted mean incorporates the signal-to-noise of individual bursts via the uncertainties, limitations due to the intrinsic bandwidth of the FRB are not explicitly accounted for. We proceed with our analysis, reasonably assuming that the reported RM’s uncertainty properly quantifies the limitations of the measurement system. We leave additional revisions for variable RMs to future work.

We furthermore describe the selection criteria and process for the FRB polarization fractions used here:

1. Only polarization measurements published before the 2023 April 10 cutoff date are considered for this sample.
2. For non-repeaters and repeaters with only 1 polarization fraction measurement, we use the available measurement. If the polarization is reported for individual sub-components of the same burst, we use the weighted mean of the sub-components.
3. A minimum signal-to-noise  $S/N > 8\sigma$  is imposed on all non-repeaters and individual bursts from repeaters included in this sample.
4. For FRBs with polarization measurements in the TNS or FRBcat databases, we defer to the catalogued value to maximize sample consistency.
5. For repeaters with multiple polarization measurements, we use the weighted mean, with the reciprocal of the errors as weights. If measurements are available at multiple frequencies, we use the L-band (1-2 GHz) if available. Otherwise, the observation with the nearest frequency below 1 GHz.

6. If only the signed circular polarization ( $V/I$ ) is reported, then the absolute value circular polarization ( $|V|/I$ ) is taken as the absolute value ( $|V/I|$ ) (for further details, see Section 4). We make this condition given that most FRBs in the literature were reported with no  $|V|/I$  measurement. If both  $L/I$  and  $V/I$  are reported but the total polarization  $\sqrt{L^2 + V^2}/I$  is not explicitly stated, the total polarization is calculated as  $\sqrt{(L/I)^2 + (V/I)^2}$ .

Expanding on criteria 3, the minimum  $S/N > 8\sigma$  applies both to non-repeaters and to the individual bursts of repeaters included in the reported weighted average polarization fractions. Many studies fail to report the S/N of FRB detections (e.g. Feng et al. 2022b,a). In these cases, we estimate the S/N as the reported flux density  $S$  divided by the radiometer noise RMS  $\sigma_S$  of the detector (e.g. Condon & Ransom 2016). If neither the S/N nor  $S$  are reported, we have chosen to include the FRB in our sample under the assumption that a reasonable detection threshold was used in the original survey.

As noted above, these selection criteria are not complete, as the weighted mean does not fully capture secularly time-varying polarization properties. We maintain the average FRB polarization fractions are sufficient for the cumulative distribution analysis presented here, and leave a fully time-dependent study to future work.

In the main text, we compare FRB properties to a sample of 1445 Galactic (and Magellanic Cloud) pulsars with published polarimetry of APs: 1305 canonical pulsars (CPs) with periods  $P > 30$  ms, 137 millisecond pulsars (MSPs,) with periods  $P < 30$  ms, and 3 magnetars and 22 RRATs with published polarization or RM data at L-band. These are compiled from Johnston et al. (2022), Serylak et al. (2021), Wahl et al. (2022), Spiewak et al. (2022), Cameron et al. (2020), Olszanski et al. (2019), Weisberg et al. (1999), Weisberg et al. (1999), Johnston & Kerr (2018), Yan et al. (2011), Gould & Lyne (1998), Kramer et al. (2007), Camilo et al. (2007), Camilo et al. (2008), Levin et al. (2012), Levin et al. (2010), Keane et al. (2011), Caleb et al. (2019), Karastergiou et al. (2009), Xie et al. (2022). We use the following criteria and process for selecting the pulsar polarimetry and RM data:

1. Only polarization measurements published before the 2023 April 10 cutoff date are considered for this sample.
2. For each pulsar, we use the polarization fractions from the average profiles (APs) (except for the MSPES single-pulse sample discussed in Section 4).
3. Most pulsars are published with both  $|V|/I$  and  $V/I$ ; we record both values and use the absolute value of  $V/I$  for consistency as discussed in Section 4.
4. If multiple RM or polarization fractions are reported, the most recent measurement is used.

We note here that, as for the FRB literature sample, these criteria are not complete, as they do not capture time-varying RMs or polarization fractions in pulsars. A weighted average of measurements is not used for pulsars given the large amount of available data. Additionally, the most recent average profile is more well-constrained, and using average profile polarization fractions consistent the current literature on pulsar polarimetry. The average profile polarization fractions are sufficient for the analysis presented in this work, and we leave a fully time-dependent discussion to future work.

**Table 4.** Previously Published FRB Sample Polarization Properties

| FRB Names                    | Polarization Telescope/<br>Frequency | L/I                        | V/I                        | Polarization Reference | RM (rad m <sup>-2</sup> )       | RM Reference | DM <sup>‡</sup> (pc cm <sup>-3</sup> ) |
|------------------------------|--------------------------------------|----------------------------|----------------------------|------------------------|---------------------------------|--------------|--|
| FRB 20201020A                | Apertif/1375.0                       | –                          | –                          | –                      | 110.0 ± 69.0                    | 1            | 398.59 ± 0.08                          |
| FRB 20191108A                | Apertif/1375.0                       | 70.0%                      | 10.0%                      | 2                      | 474.0 ± 3.0                     | 3            | 588.1 ± 0.1                            |
| <b>FRB 20190711A</b>         | ASKAP/1297.5                         | 97.48 ± 1.39% <sup>†</sup> | 0.96 ± 1.15% <sup>†</sup>  | 4                      | 9.0 ± 2.0                       | 4            | 593.1 ± 0.4                            |
| FRB 20190611B                | ASKAP/1297.5                         | 81.5 ± 2.1% <sup>†</sup>   | 31.8 ± 1.7% <sup>†</sup>   | 4                      | 20.0 ± 4.0                      | 4            | 321.4 ± 0.2                            |
| FRB 20190608B                | ASKAP/1297.5                         | 91.0 ± 3.0%                | 9.0 ± 2.0%                 | 4                      | 353.0 ± 2.0                     | 4            | 338.7 ± 0.5                            |
| FRB 20181112A                | ASKAP/1297.5                         | 90.0%                      | 10.0%                      | 5                      | 10.9 ± 0.9                      | 5            | 589.27 ± 0.03                          |
| FRB 20180924B                | ASKAP/1297.5                         | 90.2 ± 2.0%                | 13.3 ± 1.4%                | 4                      | 14.0 ± 1.0                      | 6            | 361.42 ± 0.06                          |
| FRB 20180311A                | Parkes/1382.0                        | 75.0 ± 3.0%                | 11.0 ± 2.0%                | 7                      | 4.8 ± 7.3                       | 7            | 1570.9 ± 0.5                           |
| FRB 20171209A                | Parkes/1382.0                        | 100.0 ± 1.0%               | 0.0 ± 1.0%                 | 7                      | 121.6 ± 4.2                     | 7            | 1457.4 ± 0.03                          |
| FRB 20150807A                | Parkes/1382.0                        | 80.0 ± 1.0%                | –                          | 8                      | 12.0 ± 0.7                      | 8            | 226.5 ± 0.1                            |
| FRB 20150418A                | Parkes/1382.0                        | 8.5 ± 1.5%                 | 0.0 ± 4.5%                 | 9                      | 36.0 ± 52.0                     | 9            | 776.2 ± 0.5                            |
| FRB 20150215A                | Parkes/1382.0                        | 43.0 ± 5.0%                | 3.0 ± 1.0%                 | 10                     | 1.5 ± 10.5                      | 10           | 1105.6 ± 0.8                           |
| <b>FRB 20190604A</b>         | CHIME/600.0                          | 91.2 ± 8.1%                | –                          | 11                     | –20.0 ± 1.0                     | 12           | 553.18 ± 3.23                          |
| <b>FRB 20190303A</b>         | FAST/1250.0                          | 88.7 ± 7.7% <sup>†</sup>   | 3.7 ± 5.8% <sup>†</sup>    | 13                     | –499.0 ± 0.7                    | 11           | 223.21 ± 3.23                          |
| FRB 20190102C                | ASKAP/1297.5                         | 81.14 ± 0.91% <sup>†</sup> | 5.08 ± 0.66% <sup>†</sup>  | 4                      | –110.0 ± 1.0                    | 14           | 363.6 ± 0.3                            |
| <b>FRB 20180916.J0158+65</b> | Effelsburg/1700.0                    | 102.1 ± 4.5% <sup>†</sup>  | 5.7 ± 4.4% <sup>†</sup>    | 15                     | –114.6 ± 0.6                    | 16           | 347.76 ± 1.62                          |
| FRB 20180714A                | Parkes/1382.0                        | 91.0 ± 3.0%                | 5.0 ± 2.0%                 | 7                      | –25.9 ± 5.9                     | 7            | 1467.92 ± 0.3                          |
| FRB 20160102A                | Parkes/1382.0                        | 84.0 ± 15.0%               | 30.0 ± 11.0%               | 17                     | –220.6 ± 6.4                    | 17           | 2596.1 ± 0.3                           |
| FRB 20110523A                | GBT/800.0                            | 44.0 ± 3.0%                | 23.0 ± 30.0%               | 18                     | –186.1 ± 1.4                    | 18           | 623.3 ± 0.06                           |
| <b>FRB 20121102A</b>         | Effelsburg,<br>FAST/1700,1250.0      | 13.0 ± 3.0%                | 23.5 ± 0.6% <sup>†</sup>   | 19,20                  | 127000.0 ± 800.0                | 19           | 557 ± 2                                |
| FRB 20191001A                | ASKAP/1297.5                         | 57.0 ± 1.0%                | 5.0 ± 1.0%                 | 21                     | 55.5 ± 9.0                      | 21           | 506.92 ± 0.04                          |
| <b>FRB 20201124A</b>         | Effelsburg,<br>FAST/1360.0,1250.0    | 86.21 ± 0.01% <sup>†</sup> | 10.23 ± 0.01% <sup>†</sup> | 13,22,23,31            | –601.0 ± 11.1 <sup>†</sup>      | 22           | 410.83 ± 3.23                          |
| FRB 20180309A                | Parkes/ 1382.0                       | 45.56 ± 0.06%              | 24.33 ± 0.05%              | 7                      | –                               | –            | 263.42 ± 0.01                          |
| <b>FRB 20200120E</b>         | Effelsburg/1400.0                    | 99.3 ± 1.3% <sup>†</sup>   | 4.5 ± 0.9% <sup>†</sup>    | 30                     | –29.8 ± 5.0                     | 24           | 88.96 ± 1.62                           |
| FRB 20151230A                | Parkes/1352.0                        | 35.0 ± 13.0%               | 6.0 ± 11.0%                | 25                     | –                               | –            | 960.4 ± 0.5                            |
| FRB 20140514A                | Parkes/1352.0                        | 0.0%                       | 21.0 ± 7.0%                | 26                     | –                               | –            | 562.7 ± 0.6                            |
| <b>FRB 20190520B</b>         | GBT/1450.0                           | 9.0%                       | 9.83 ± 0.68% <sup>†</sup>  | 27,20                  | –11000.0 ± 13100.0 <sup>†</sup> | 27           | 1202 ± 10                              |
| <b>FRB 20220912A</b>         | FAST/1400.0                          | 80.3 ± 24.3% <sup>†</sup>  | 5.2 ± 0.2% <sup>†</sup>    | 28                     | 0.6 ± 0.1                       | 29           | 219.46 ± 0.04                          |
| <b>FRB 20180814A</b>         | CHIME/600.0                          | 69.1 ± 4.7%                | –                          | 11                     | 699.8 ± 1.0                     | 11           | 190.86 ± 3.23                          |
| <b>FRB 20181030A</b>         | CHIME/600.0                          | 72.75 ± 2.22% <sup>†</sup> | –                          | 11                     | 36.6 ± 0.2 <sup>†</sup>         | 11           | 101.9 ± 1.62                           |
| <b>FRB 20181119A</b>         | CHIME/600.0                          | 67.58 ± 2.76% <sup>†</sup> | –                          | 11                     | 1340.0 ± 2.0 <sup>†</sup>       | 11           | 368.79 ± 6.47                          |
| <b>FRB 20190222A</b>         | CHIME/600.0                          | 24.61 ± 0.58%              | –                          | 11                     | 571.0 ± 1.7                     | 11           | 462.6 ± 3.23                           |
| <b>FRB 20190208A</b>         | CHIME/600.0                          | 86.52 ± 1.03% <sup>†</sup> | –                          | 11                     | 36.3 ± 0.7                      | 11           | 579.06 ± 3.23                          |
| <b>FRB 20190213B</b>         | CHIME/600.0                          | 90.19 ± 2.68% <sup>†</sup> | –                          | 11                     | –3.63 ± 0.41                    | 11           | 302.47 ± 1.62                          |
| <b>FRB 20180908B</b>         | CHIME/600.0                          | 0.0%                       | –                          | 11                     | 0.18                            | 11           | 197.33 ± 3.23                          |
| <b>FRB 20190117A</b>         | CHIME/600.0                          | 19.44 ± 0.40% <sup>†</sup> | –                          | 11                     | 76.31 ± 0.40                    | 11           | 393.05 ± 1.62                          |
| <b>FRB 20190417A</b>         | FAST/1250.0                          | 71.5 ± 2.5%                | 11.7 ± 2.0%                | 13                     | 4429.8 ± 3.5                    | 11           | 1378.11 ± 6.47                         |
| <b>FRB 20190907A</b>         | CHIME/600.0                          | 28.0%                      | –                          | 11                     | –                               | –            | 307.32 ± 3.23                          |

**Notes:** Observation and polarization information for the compiled sample of previously published FRBs. The telescope and system observing frequency are those used for the polarization measurements. Names in boldface are repeaters, while non-boldfaced FRBs are non-repeating as of April 10th, 2023. For FRB 20220912A, the RM is that reported by CHIME while the polarization was measured from the DSA-110 detections. For repeaters with multiple RM or polarization measurements, values are the weighted average of observations. The sample was compiled with the use of the Transient Name Server (TNS), the FRB Catalog (FRBcat), and the Canadian Hydrogen Intensity Mapping Experiment (CHIME) FRB Catalog 1 (Petroff & Yaron (2020), Petroff et al. (2016), Amiri et al. (2021)). FRB 20180301 was excluded from this literature sample due to its inconsistent RM and L-band polarization properties, which are not accurately described by average values (Luo et al. 2020; Kumar et al. 2023). While Zhang et al. (2023) and Anna-Thomas et al. (2023a) (a later version of Anna-Thomas et al. (2023b)) presented additional polarization data, they were released after the data cutoff date and are excluded from this sample.

<sup>†</sup>Weighted mean of multiple bursts; <sup>‡</sup>DM values are from the TNS catalog

Citations are listed below: (1)Pastor-Marazuela et al. (2022) (2)Connor et al. (2020) (3)van Leeuwen et al. (2022) (4)Day et al. (2020) (5)Prochaska et al. (2019) (6)Bannister et al. (2019) (7)Osłowski et al. (2019) (8)Ravi et al. (2016) (9)Keane et al. (2016) (10)Petroff et al. (2017) (11)Mckinven et al. (2023) (12)Fonseca et al. (2020) (13)Feng et al. (2022b) (14)Macquart et al. (2020) (15)Nimmo et al. (2021) (16)Andersen et al. (2019) (17)Caleb et al. (2018) (18)Masui et al. (2015) (19)Plavin et al. (2022) (20)Feng et al. (2022a) (21)Bhandari et al. (2020) (22)Hilmarsson et al. (2021a) (23)Jiang et al. (2022) (24)Bhardwaj et al. (2021) (25)Bhandari et al. (2018) (26)Petroff et al. (2015) (27)Anna-Thomas et al. (2023b) (28)Ravi et al. (2023) (29)McKinven & Chime/Frb Collaboration (2022) (30)Nimmo et al. (2022) (31)Xu et al. (2022)

B. DSA-110 VOLTAGE DATA MODEL AND POLARIZATION PROCESSING

All polarization analysis of DSA-110 FRBs detected during the commissioning observations reported on herein, and the calibration of these data, are accomplished using automatically triggered voltage dumps. This refers to the storage of 61440 contiguous post-channelization complex (i.e., undetected) spectra for each antenna, with a time-resolution of 32.768  $\mu\text{s}$ . The spectra consist of voltage measurements in two polarization channels for each of 63 antennas, in 6144 channels of 30.52 kHz width centered on 1405 MHz. Each complex sample is stored with 4-bit resolution for the real and imaginary parts. The four most significant bits are chosen using channel-dependent coefficients determined from the mean bandpass shapes of each antenna/polarization pair. For FRB data, the triggers are generated such that the arrival times of the bursts at 1498.75 MHz (the upper limit of the sampled band) correspond to exactly 0.5 s into the voltage dumps. Each voltage dump is stored in raw binary format, and is accompanied by a json header that includes all relevant descriptive information.

The voltage dumps are processed using a custom full-polarization beamforming pipeline (*dsa110-bbproc*). Post-correlation beamforming is implemented (Roy et al. 2018) with the addition of both auto- and cross-correlation terms to mitigate quantization noise in applying per-antenna beamforming weights. For FRB data, the weights are determined from visibility data on bright bandpass calibrators typically within 12 hr of detection. For voltage dumps on the continuum-source calibrators 3C48 and 3C286, the weights are determined from visibility data on the calibrators themselves. Ultimately, filterbank-format files are generated for each Stokes parameter by synthesizing beams in the directions of interest for each voltage dump. The polarization and Faraday-rotation definitions adopted here are summarized in Appendix C.

The *dsa110-pol* module was developed to calculate FRB polarization and RM parameters offline from the polarized filterbank data. Major processing steps are as follows:

1. Polarimetric calibration is applied using the formalism described in Appendix D. The stability of the calibration solutions is justified in Appendix E, and critical assumptions on leakage are justified in Appendix F.
2. Full-polarization spectra for each FRB are generated by optimally averaging over the burst temporal profiles (Appendix H).
3. RM estimation then proceeds on these spectra as described in Appendix I. If a significant RM is detected, the Stokes parameters are corrected for this RM.
4. Then, the total ( $T$ ), linear ( $L$ ) and circular ( $C$ ) polarization spectra, as well as polarization position angle ( $\chi$ ) are computed. The average polarization fractions, referred to as  $L/I$ ,  $|V|/I$  and  $\sqrt{L^2 + V^2}/I$ , are calculated as the weighted mean of  $L_{\text{unbias}}(t)/I(t)$ ,  $C(t)/I(t)$ , and  $T(t)/I(t)$  across the FWHM of the burst using the optimal weights (Appendix H). In addition, the sign-dependent circular polarization fraction  $V/I$  is computed as the weighted mean of  $V(t)/I(t)$  across the burst. The mean position angle  $\chi$  is calculated with a similar weighted mean across the FWHM.

### C. POLARIZATION AND FARADAY ROTATION BACKGROUND

The polarization of light is defined by the correlation properties of components of the propagating electric field. In a linear basis, where  $V_A$  and  $V_B$  refer to orthogonal linear components of the electric field, the Stokes parameters are one representation of the polarization state:

$$I = \frac{1}{2}(\langle V_A V_A^* \rangle + \langle V_B V_B^* \rangle) \quad (\text{C1})$$

$$Q = \frac{1}{2}(\langle V_A V_A^* \rangle - \langle V_B V_B^* \rangle) \quad (\text{C2})$$

$$U = \text{Re}\{\langle V_A V_B^* \rangle\} \quad (\text{C3})$$

$$V = -\text{Im}\{\langle V_A V_B^* \rangle\} \quad (\text{C4})$$

The DSA-110 uses the IAU/IEEE convention that  $V > 0$  is right-hand polarization, while  $V < 0$  is left-hand polarization (Van Straten et al. 2010). The linear, circular, and total polarization fractions as a function of time are computed as:

$$\frac{L_{\text{unbias}}(t)}{I(t)} = \begin{cases} \sqrt{L(t)^2 - \sigma^2}/I(t), & \text{for } \frac{L(t)}{\sigma} > 1 \\ 0, & \text{o/w} \end{cases} \quad (\text{C5})$$

$$\frac{C(t)}{I(t)} = \sqrt{V(t)^2}/I(t) \quad (\text{C6})$$

$$\frac{T(t)}{I(t)} = \sqrt{L_{\text{unbias}}(t) + V(t)^2}/I(t) \quad (\text{C7})$$

where  $L_{\text{unbias}}(t)$  is the unbiased linear polarization following Simmons & Stewart (1985) and Everett & Weisberg (2001), and  $L(t) = \sqrt{Q(t)^2 + U(t)^2}$ <sup>15</sup>. These are averaged across a burst to estimate the average polarization fractions. For all sources,  $T \leq I$ ; in unpolarized sources,  $T = 0$ . In partially polarized sources,  $T = pI < I$ , where  $p$  is the polarization fraction. Finally, the position angle  $\chi$  defines the phase difference between linearly polarized components:

$$\chi = 0.5 \tan^{-1}\left(\frac{U}{Q}\right) = 0.5 \angle P \quad (\text{C8})$$

where  $P = Q + iU$  is the linear polarization vector. Errors in the position angle are estimated using a Monte Carlo simulation of 100 boxcar pulses with  $\chi = 0$  and unity off-pulse standard deviation. The resulting error as a function of linear-polarization S/N is well-fit by a piecewise exponential with scale  $28\sigma$  for  $S/N > 19\sigma$ , and  $10\sigma$  for  $S/N \leq 19\sigma$ . Figure 8 shows the results of the simulation and best fit piecewise exponential; note these results imply that the Naghizadeh-Khouei & Clarke (1993) PA distribution significantly under-estimates the error, particularly for  $S/N > 6\sigma$ .

<sup>15</sup> Note we adopt the convention used in equations 10 and 16 of Simmons & Stewart (1985) due to ambiguity in the unbiasing factor reported in Everett & Weisberg (2001).

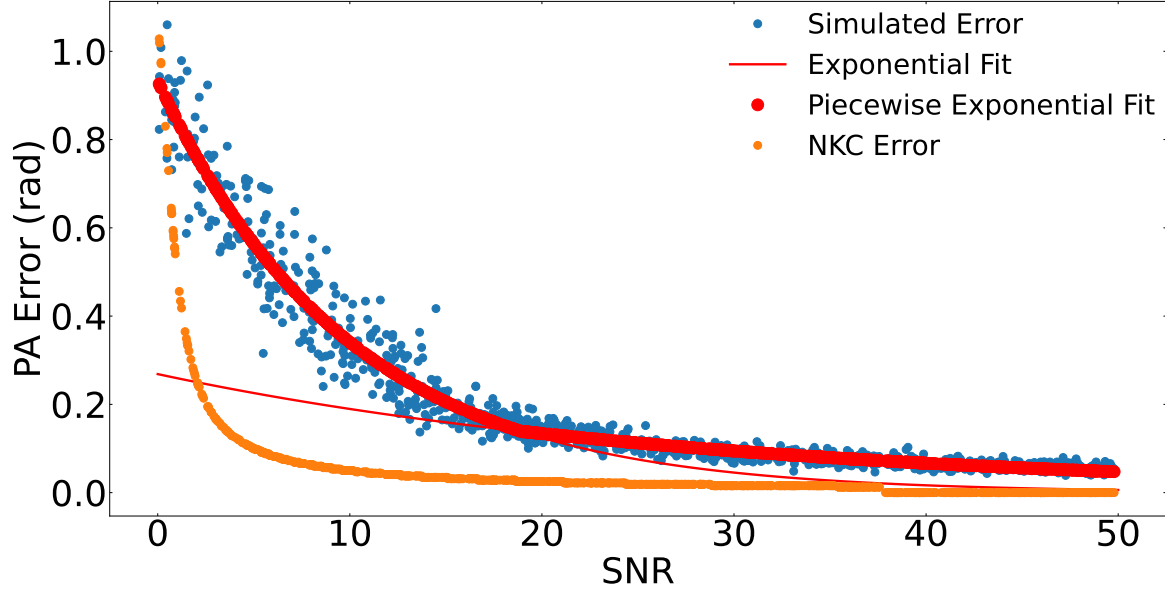


**Figure 8.** Simulated error in the linear polarization position angle (PA), as a function of linear-polarization S/N. See text for details of the simulation. The simulated error (blue) is taken as the standard deviation of the PA across the width of each boxcar pulse. The red lines indicate the piecewise exponential fit of the simulated error, while the red markers show the resulting error for each trial when computed using the fit. The error derived from the PA distribution of [Naghizadeh-Khouei & Clarke \(1993\)](#), shown in orange, appears to underestimate the error, especially at high S/N.

A different dispersion relation applies to orthogonal circularly polarized components for propagation through a plasma-filled region with a magnetic field, resulting in a rotation of the position angle of linearly polarized radiation. The position angle changes as a function of squared wavelength such that the RM is defined as:

$$\text{RM} = \frac{d\chi}{d\lambda^2} \quad (\text{C9})$$

The RM characterizes the integrated line of sight magnetic field  $\bar{B}_{\parallel}$  that induces this rotation, weighted by the plasma electron number density  $n_e$ :

$$\text{RM} = 0.81 \int \frac{n_e B_{\parallel}}{(1+z(l))^2} dl \quad (\text{C10})$$

where  $z$  is the redshift of the dispersive material. Note that the  $\bar{\phantom{x}}$  indicates the field is averaged over the line-of-sight. In general, the RM has contributions from an FRB's host galaxy, the intergalactic medium (IGM), the Milky Way's circumgalactic medium (CGM) and interstellar medium (ISM), and the Earth's ionosphere due to the magnetic fields in these regions. This can, in addition to changing the magnitude of the RM, change the sign due to the direction dependence of the magnetic field. If the same plasma is assumed to contribute to both dispersion and RM:

$$\text{DM} = \int_l^0 \frac{n_e}{1+z(l)} dl \quad (\text{C11})$$

the average line-of-sight magnetic field can be estimated as:

$$\bar{B}_{\parallel} [\mu\text{G}] \approx \frac{\text{RM}}{0.81 \cdot \text{DM}} (1+z) \quad (\text{C12})$$

Recent analyses imply a correlation between host RM (RM with contributions from the ionosphere, ISM, and IGM subtracted) and DM, implying that this approximation is reasonable (Mannings et al. 2022). We refer to position angle after correcting for RM as the polarization position angle (PPA;  $\chi_0$ ), while PA, or  $\chi$ , refer to the position angle measured without RM correction.

#### D. DERIVATION OF JONES MATRIX AND PARALLACTIC ANGLE CALIBRATION FOR DSA-110

An effective Jones matrix for the coherently combined DSA-110 must be used to calibrate polarized observations, as described by, e.g., Robishaw & Heiles (2021). Calibration with a fully-defined Jones matrix accounts for cross-coupling between the orthogonal linearly polarized receptors, as well as gain and phase differences between the receptors (Heiles et al. 2001). Here we will choose a Cartesian basis aligned with the linearly polarized receptors. For the DSA-110, we operate in the ‘ideal feed’ assumption, that is, that there is zero cross-coupling between receptors. This requires that differences in gain or phase between the X and Y feeds are the dominant instrumental effect, which results in mixing among Stokes parameters. A difference between the X and Y gain will mix Stokes I and Q creating apparent linear polarization. A difference in phase corresponds to a time delay  $\Delta t \approx \phi(\nu)(2\pi\nu)^{-1}$  between the X and Y feeds. This mixes Stokes U and V and creates residual circular polarization. Quantitatively, for the arbitrary Jones matrix below consisting of four complex terms:

$$J(\nu) = \begin{bmatrix} g_{xx}(\nu) & g_{xy}(\nu) \\ g_{yx}(\nu) & g_{yy}(\nu) \end{bmatrix} \quad (\text{D13})$$

we assume  $|g_{xy}(\nu)| = |g_{yx}(\nu)| = 0$ . We further simplify this by assuming  $g_{yy}(\nu)$  is real and parameterize in terms of the absolute gain in the Y receptor,  $|g_{yy}(\nu)|$ , the ratio of the magnitudes of X and Y gains,  $r(\nu) = |g_{xx}(\nu)|/|g_{yy}(\nu)|$ , and the phase difference between the X and Y receptors,  $\phi(\nu)$ . The Jones matrix is then simplified to:

$$J(\nu) = \begin{bmatrix} r(\nu)|g_{yy}(\nu)|e^{i\phi(\nu)} & 0 \\ 0 & |g_{yy}(\nu)| \end{bmatrix} \quad (\text{D14})$$

One can estimate  $r$  by observing a known unpolarized source and assuming  $Q = U = V = 0$ . Similarly, one estimates  $\phi$  by observing a known linearly polarized source and assuming  $V = 0$ . For DSA-110 observations, 3C48 was periodically observed as the unpolarized calibrator to estimate  $r(\nu)$ , while 3C286 was observed as the linearly polarized calibrator to estimate  $\phi(\nu)$ . Given the fixed declination ( $71.6^\circ$ ) of the DSA-110 commissioning survey, the affect of sky position on polarization calibration is left to future work. For this work, it is reasonable to assume that a single set of

calibrators, 3C48 and 3C286, is sufficient for a constant pointing. At our 1.4 GHz observing frequency, 3C48 is known to be weakly polarized ( $\sim 0.5\%$ ), which we assume is acceptable for use as an unpolarized calibrator within the error of the DSA-110<sup>16</sup> (Perley & Butler 2013). 3C286 is known to have 9.5% linear polarization at 1.4 GHz, making it suitable as a linearly polarized calibrator (Perley & Butler 2013). The absolute gain in the Y receptor,  $|g_{yy}(\nu)|$ , is estimated using 3C48 by comparing the observed flux to the polynomial fit (after correcting for the measured RM<sup>17</sup> of  $-68 \text{ rad m}^{-2}$  and estimated parallactic angle) defined by Perley & Butler (2017).  $r(\nu)$ ,  $\phi(\nu)$ , and  $|g_{yy}(\nu)|$  were determined after averaging over spurious peaks in Stokes parameters for each source as function of frequency, downsampling in frequency, then interpolating back to native resolution. For FRB observations, we calibrate by applying the inverse Jones matrix to the observed Stokes parameters, effectively setting the gain and phase of the X and Y feeds equal and minimizing the mixing of Stokes parameters.

Absolute position angles cannot be estimated with the current DSA-110 pipeline, as it would require tracking a calibrator source over a wide range of parallactic angles which the DSA-110, as a transit instrument, is not currently equipped for. In this work, an attempt to derive absolute position angle estimates by treating the DSA-110 as a single antenna; following Thompson et al. (2017) (Chapter 4), the elevation and azimuth of the array for a given FRB are estimated using the RA,  $\alpha$ , and declination,  $\delta$ , of the detected beam and observation time LST:

$$\sin(\theta) = \sin(b_{\text{DSA}}) \sin(\delta) + \cos(b_{\text{DSA}}) \cos(\delta) \cos(\text{LST} - \alpha) \quad (\text{D15})$$

$$\sin(\phi + (b - 125)\delta\theta_b) = -\frac{\cos(\delta) \sin(\text{LST} - \alpha)}{\cos(\theta)} \quad (\text{D16})$$

where  $l_{\text{DSA}}$  and  $b_{\text{DSA}}$  are the longitude and latitude of the DSA-110 (Owens Valley).  $b$  is the detected beam and  $\delta\theta_b = 14''$  is the synthesized beamwidth. The parallactic angle  $\chi_{\text{par}}$  is then estimated as:

$$\sin(\chi_{\text{par}}) = -\frac{\sin(\phi) \cos(b_{\text{DSA}})}{\cos(\delta)} \quad (\text{D17})$$

and can be applied as a correction  $\chi_{\text{cal}} = \chi_0 + \chi_{\text{par}}$ .

## E. CALIBRATION STABILITY WITH TIME AND PRIMARY-BEAM LOCATION

Four epochs of calibration observations were taken during the survey to apply to the sample of FRBs reported in this paper. Table 5 summarizes each observation. Each observation consists of multiple voltage dumps during the calibration-source transit. The transits nearest the center of the primary beam were used to derive Jones matrix parameters at each epoch. Figure 9 shows the Jones matrix solutions as a function of frequency for each epoch. From this, it is clear that the solution is stable, with standard deviation across epoch of 0.2%, 0.1 rad, and 3.6% for  $r(\nu)$ ,  $\phi(\nu)$ , and  $|g_{yy}(\nu)|$ , respectively. Given this stability, the solutions were averaged together over all epochs and filtered in the frequency domain with a first order Savitsky-Golay filter, and this average solution was then used to calibrate all FRBs detected. The outlier  $|g_{yy}(\nu)|$  solution from the 2022 April 14

<sup>16</sup> In Appendix F we verify this assumption through leakage polarization tests. For additional information on polarized calibrators, see documentation for the Very Large Array (VLA) at <https://science.nrao.edu/facilities/vla/docs/manuals/obsguide/modes/pol>.

<sup>17</sup> Note the RM of 3C48 is measured at higher frequencies (1.6–30 GHz, or 1–18 cm wavelengths) where the polarization fraction is higher (Perley & Butler 2013).

observation was investigated and attributed to a software error which prevented the measurement set from being properly saved. The beamformer weights for this observation were therefore not gain calibrated resulting in a vertical offset in the measured Stokes parameters. Following the correction of this issue, no outliers were identified in subsequent calibration solutions, as shown in Figure 9. We therefore do not include the  $|g_{yy}(\nu)|$  value from the 2022 April 14 observation in the average  $|g_{yy}(\nu)|$  solution or the standard deviation reported above.

**Table 5.** Polarization Calibration Observations and Jones Matrix Parameters

| 3C48 observation name (Beam)              | MJD       | 3C286 observation name (Beam) | MJD       | $\langle r(\nu) \rangle$ | $\langle \phi(\nu) \rangle$ | $\langle  g_{yy}(\nu)  \rangle$ |
|---|-----------|-------------------------------|-----------|--------------------------|-----------------------------|---------------------------------|
| <b>2022/04/14, 2022/05/24 Observation</b> |           |                               |           |                          |                             |                                 |
| kkz (46)                                  | 59683.829 | dnz (18)                      | 59723.215 | $1.00 \pm 0.04$          | $2.09 \pm 0.14$             | $1.48 \pm 0.06$                 |
| ane (197)                                 | 59683.837 | fvr (57)                      | 59723.217 |                          |                             |                                 |
| <b>bjz</b> (110)                          | 59572.309 | <b>kus</b> (135)              | 59723.221 |                          |                             |                                 |
|   |           | oxr (174)                     | 59723.223 |                          |                             |                                 |
| <b>2022/09/14 Observation</b>             |           |                               |           |                          |                             |                                 |
| <b>lck</b> (107)                          | 59835.417 | mph (44)                      | 59835.908 | $0.99 \pm 0.02$          | $2.11 \pm 0.20$             | $1.86 \pm 0.02$                 |
| bxc (182)                                 | 59835.422 | <b>tnh</b> (122)              | 59835.912 |                          |                             |                                 |
|   |           | ezb (200)                     | 59835.916 |                          |                             |                                 |
| <b>2022/10/21 Observation</b>             |           |                               |           |                          |                             |                                 |
| xtu (47)                                  | 59872.313 | gbf (45)                      | 59872.807 | $1.00 \pm 0.03$          | $2.15 \pm 0.12$             | $1.78 \pm 0.04$                 |
| <b>eit</b> (123)                          | 59872.317 | <b>lrp</b> (123)              | 59872.811 |                          |                             |                                 |
| jvp (198)                                 | 59872.321 | fml (201)                     | 59872.815 |                          |                             |                                 |
| <b>2022/11/23 Observation</b>             |           |                               |           |                          |                             |                                 |
| xxc (22)                                  | 59906.219 | quh (19)                      | 59906.713 | $1.00 \pm 0.03$          | $2.29 \pm 0.11$             | $1.80 \pm 0.04$                 |
| fjr (72)                                  | 59906.222 | xnr (71)                      | 59906.716 |                          |                             |                                 |
| <b>mia</b> (123)                          | 59906.224 | <b>wtw</b> (123)              | 59906.718 |                          |                             |                                 |
| xol (173)                                 | 59906.227 | vxo (175)                     | 59906.721 |                          |                             |                                 |
| wsj (223)                                 | 59906.230 | hwj (227)                     | 59906.724 |                          |                             |                                 |

**Notes:** Labels in bold are those nearest the center beam and are used to derive the Jones parameters in the last three columns.  $\langle \rangle$  indicates the average value over frequency.

In addition to long-term stability, stability across the primary beam was estimated by using multiple Jones solutions from each epoch to calibrate the adjacent voltage dumps during the transits of 3C48 and 3C286. For each epoch, the gain solutions  $r(\nu)$  and  $|g_{yy}(\nu)|$  were taken as piecewise polynomial fits, while the phase solution  $\phi(\nu)$  was taken as the median value across the band in order to reduce the impact of noise. The calibration is deemed stable if there is no systematic change in the resulting polarization fraction and position angle as a function of each source’s location within the primary beam. No significant variations in the recovered polarization properties, including RM, for 3C48 and 3C286 were observed. We therefore proceeded to use the beam-center voltage dumps to derive calibration parameters.

## F. CALIBRATION LEAKAGE ESTIMATES

In the above method, the off-diagonal terms characterizing leakage between the orthogonal receptors are assumed negligible, meaning that calibrated data will be uncertain up to the true magnitude of

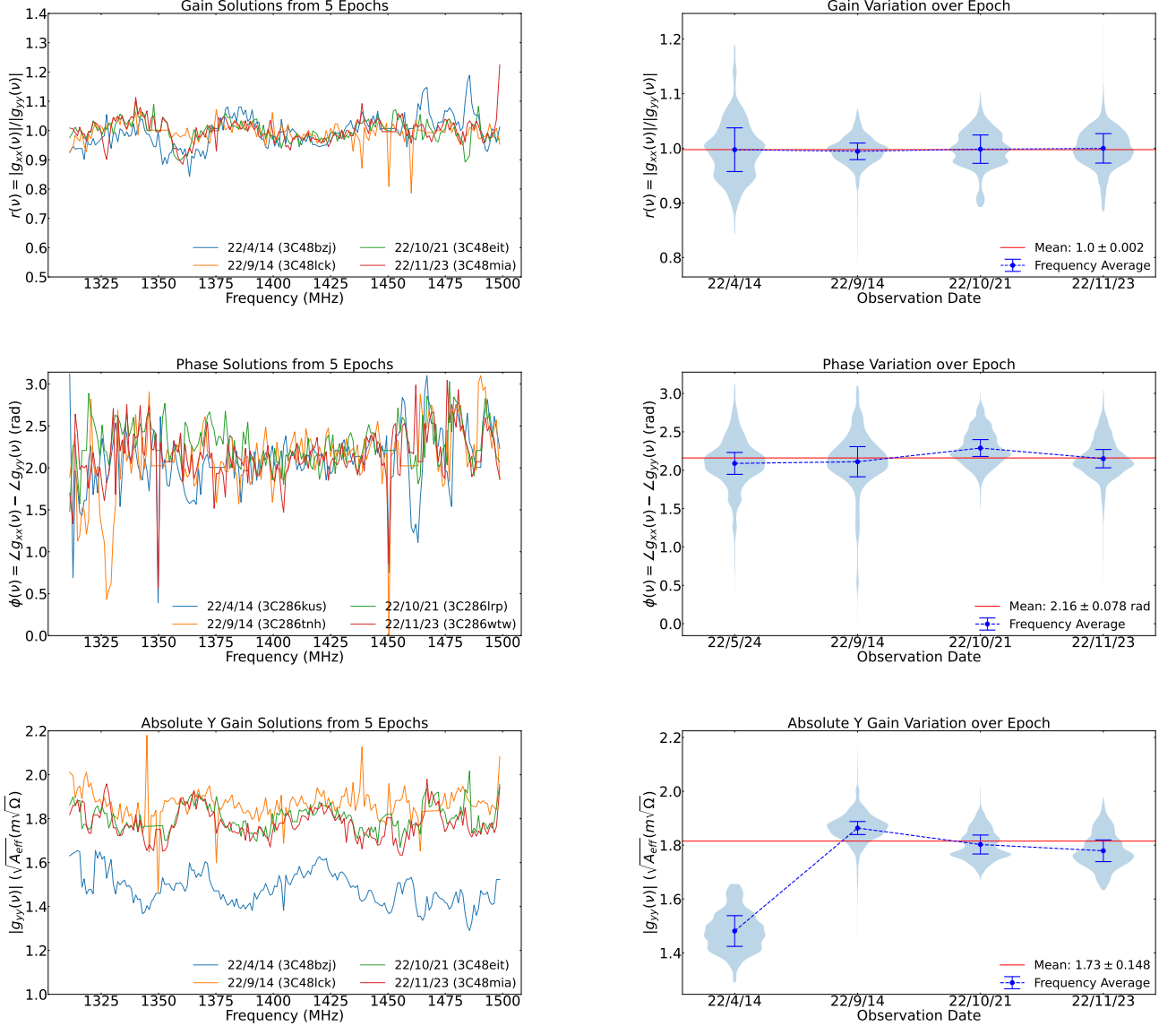


**Figure 9.** Jones matrix solutions on four epochs. *Left:* Frequency dependent  $r(\nu)$ ,  $\phi(\nu)$ , and  $|g_{yy}(\nu)|$  after removing birdies, downsampling and interpolating. *Right:* Solutions averaged over frequency for each observation. The violin plots show the distribution of the frequency dependent points while the red line shows the average value over all epochs.

these terms. The above calibration corrects leakage between Stokes I and Q and between U and V. The leakage terms cannot be explicitly solved for without the observation of additional polarized sources over a wide range of position angles; this is not feasible with the DSA-110. Leakage between the other pairs of Stokes parameters is instead estimated by again calibrating adjacent voltage dumps on 3C48 and 3C286 on each observation epoch as described in the previous section. The remaining Q, U, and V fractions in calibrated 3C48 observations then estimate the remaining I leakage. Subtracting these leakages and the expected 9.6% linear polarization at position angle of  $\chi = 33^\circ$  from calibrated 3C286

then allows for other leakage terms to be estimated. Specifically, the residual linear polarization above the expected 9.6% then corresponds to leakage from V into Q or U; the residual circular polarization is likewise leakage from Q and U into V. One can visualize this with the Mueller polarization matrix formalism (Heiles et al. 2001). The I-Q, I-U, I-V leakages then roughly estimate the first row and first column of the Mueller matrix, while QU-V and V-QU roughly estimate the other off-diagonal terms, and the diagonal terms are derived from  $r(\nu)$ ,  $\phi(\nu)$ , and  $|g_{yy}(\nu)|$ . While the matrix cannot be explicitly solved based on the 3C48 and 3C286 observations available, the leakage estimates reported here offer order of magnitude estimates.

Error bars are estimated by taking the standard error and subtracting the systematic standard error from beams within each voltage dump in which the source was not present, which characterizes the thermal noise. Leakage values for each epoch are summarized in Figure 10; the maximum leakage observed is 1.6% between I and U. This is within acceptable limits and justifies the ideal feed assumption above.

### G. EXAMPLE OF POLARIZATION CALIBRATION WITH PULSAR J1935+1616

In Section 2, we presented the functioning polarization pipeline using the stacked profile of J1935+1616 shown in Figure 1. Here we further compute  $L/I$ ,  $|V|/I$ , and  $V/I$  for each of the 26 pulses and for the folded profile to compare to the measured values from Gould & Lyne (1998). The linear polarization of the folded profile is  $L/I = 14.6 \pm 5.6\%$ , which is lower than the expected 18% but agrees within the  $1\sigma$  errorbar. The absolute value circular polarization is  $|V|/I = 16.9 \pm 5.7\%$  which is also within  $1\sigma$  of the expected 15%. The signed circular polarization,  $-2.5 \pm 21.6\%$  agrees with expected 2% within  $1\sigma$  despite the opposite sign. From the pulse profiles in Figure 1 it is clear that this difference in sign is stochastic rather than a sign error in calibration<sup>18</sup>. From this we conclude that there is good agreement between the DSA-110 polarization measurement of J1935+16 and expectation and find no significant systematic errors to apply. Figure 11 shows the polarization fractions of each of the 26 pulses as well as those of the average profiles. Note the low expected RM,  $-2.3 \pm 0.5 \text{ rad m}^{-2}$ , and the low detected linear-polarization S/N prevent a confident RM measurement for verification.

### H. OPTIMAL SPECTRAL ESTIMATION

After calibration of each FRB, full-Stokes spectra are calculated by averaging over the burst time series. In order to prevent inclusion of noise in the spectrum, a window around each burst is first manually defined to contain all apparent emission components, over which the average spectrum is computed. Ideally, the pulse would then be weighted using the variance at each time step. These variances are estimated as the inverse of the frequency averaged S/N at each time step, i.e., the temporal profile of the burst. Previous studies have used a Gaussian fit and similar functions to estimate pulse profiles. However, the large variety in burst morphology among FRBs implies a Gaussian may not offer a reasonable fit. The pulse profile is determined by first averaging the total-intensity dynamic spectrum over frequency, then downsampling and linear interpolating to the desired time resolution to eliminate stochasticity and insignificant mid-pulse structure. Finally, to remove artifacts in due to the interpolation, the profile is filtered with a third-order Savitsky-Golay

<sup>18</sup> In this paper we adopt the IAU/IEE convention for Stokes V, in which  $V > 0$  is right-handed and  $V < 0$  is left-handed. Gould & Lyne (1998) use the PSR/IEE convention which has the opposite definition. Therefore, we have flipped the sign of Stokes V in both the EPN profile in Figure 1 and the expected  $V/I$  so that both are in the IAU/IEE convention for more accurate comparison.

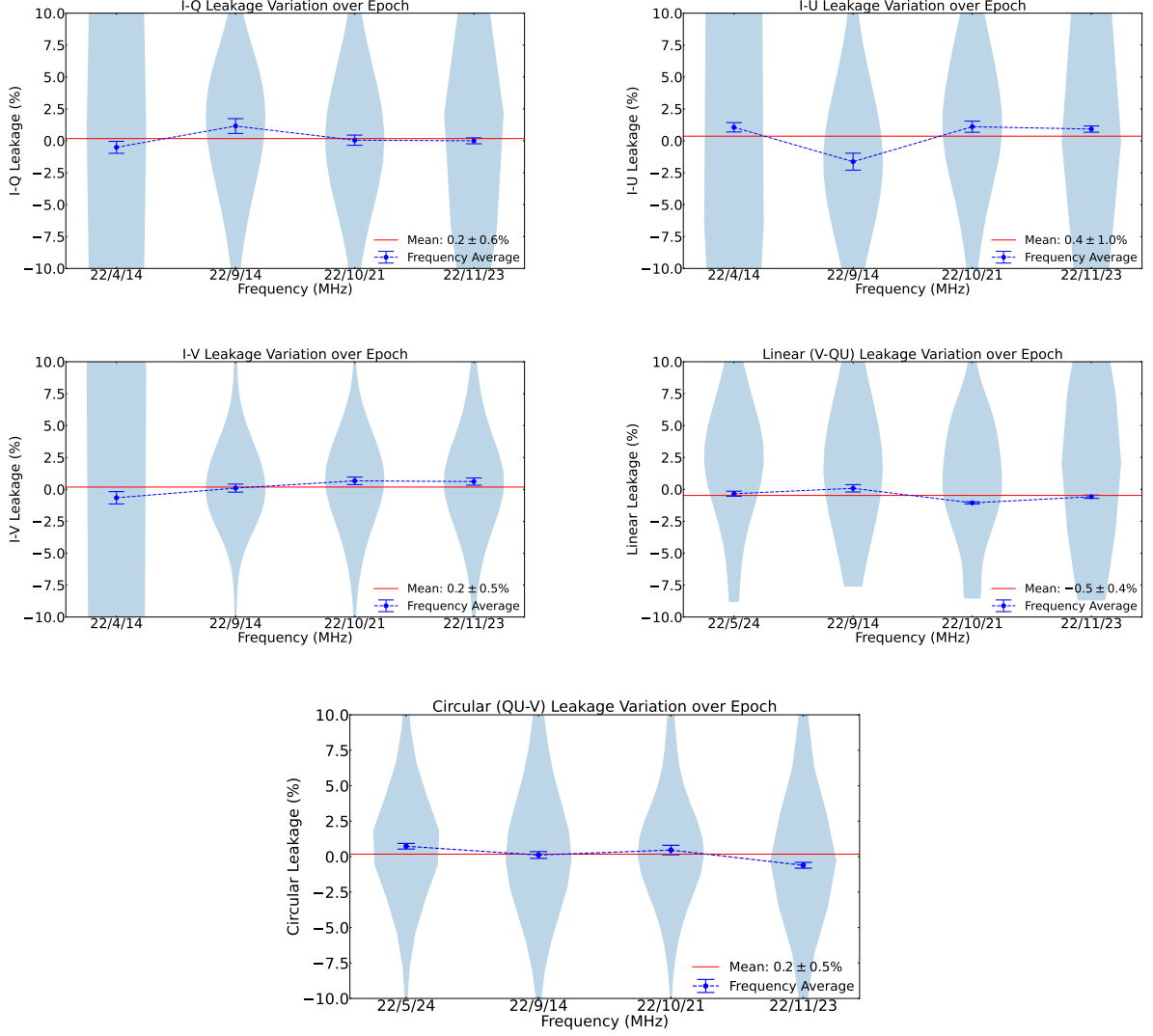


**Figure 10.** Violin plots of leakage estimates. The mean values are shown as markers, while the distributions are values from all calibrated voltage dumps and all frequency channels in each observation.

filter, with the filter width chosen specific to each burst. The profile is set to zero outside of the burst window defined above. The spectrum can then be computed as a weighted sum of the time series within the defined window using the profile as weights.

### I. DETAILED RM SYNTHESIS DERIVATION AND S/N METHOD ERROR

What follows is a detailed derivation of the RM Synthesis method and its variation, the S/N Method, utilized in this paper (Heald 2008; Brentjens & De Bruyn 2005; Burn 1966). In the discrete case, Burn (1966) estimates the Faraday dispersion function (FDF) as the Fourier transform of the observed linear polarization vector  $P_{\text{obs}}(\lambda^2) = Q_{\text{obs}}(\lambda^2) + iU_{\text{obs}}(\lambda^2)$  from  $\lambda^2$  space to RM space:

$$\hat{F}(\text{RM}) = \frac{1}{N_{\lambda^2}} \sum_{\lambda^2} P_{\text{obs}}(\lambda^2) W(\lambda^2) e^{-2i\text{RM}(\lambda^2 - \lambda_0^2)} \quad (\text{I18})$$

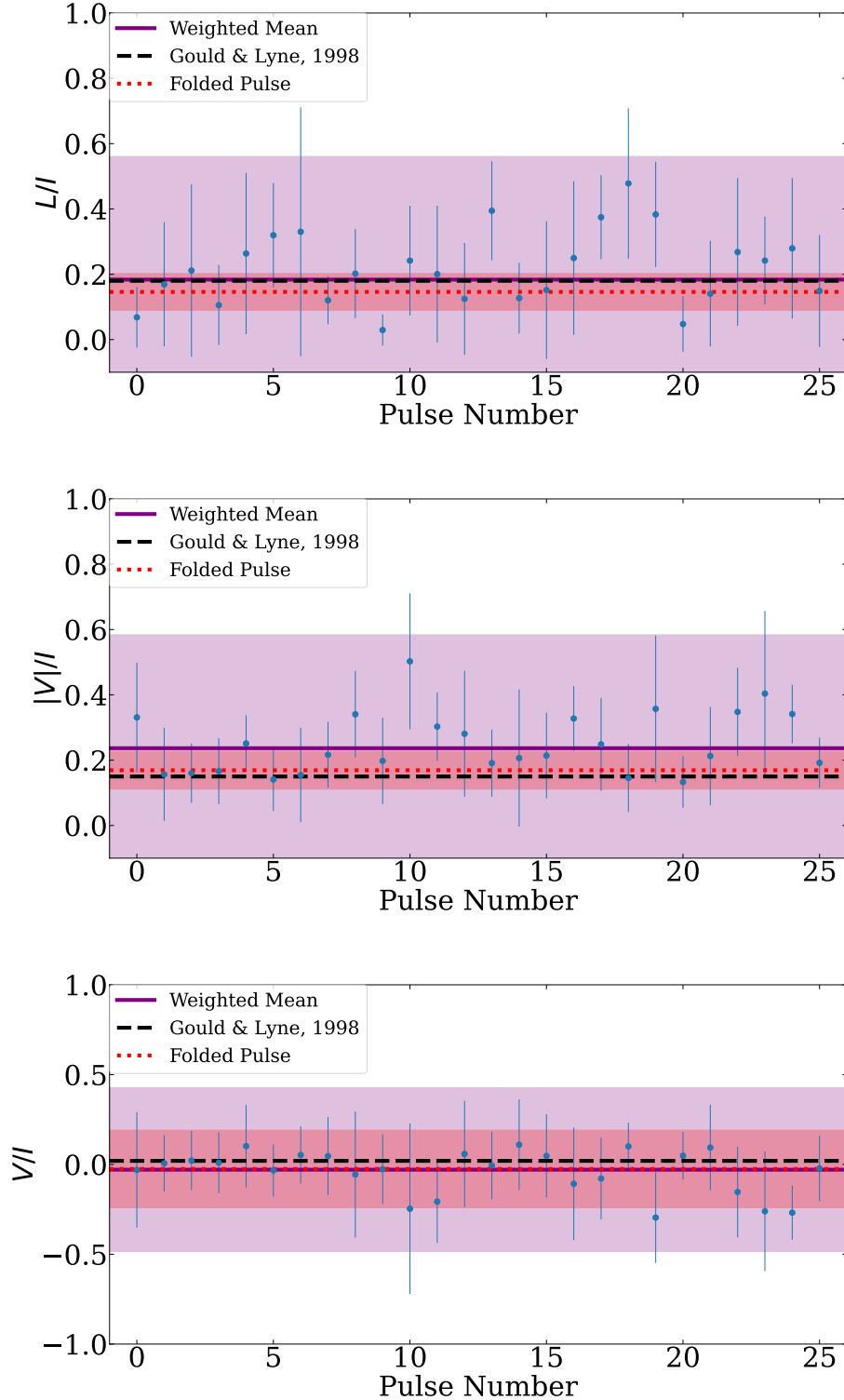


**Figure 11.** Linear (*top*), absolute value circular (*middle*), and signed circular polarization (*bottom*) measurements of J1935+1616. Polarization fractions for individual pulses are shown in blue, and the weighted mean is shown in purple, with the shaded area indicating the weighted error. The expected polarization fractions from Gould & Lyne (1998) (18%, 15%, and 2% from top to bottom) are shown in black. The linear and absolute value circular polarization fractions measured from the folded profiles, shown in red, are in good agreement with expectation within the  $1\sigma$  errorbar.

where  $\lambda_0$  is the mean of the  $\lambda^2$  axis, and  $W(\lambda^2)$  are weights applied to the spectra. Note that  $Q_{\text{obs}}(\lambda^2)$  and  $U_{\text{obs}}(\lambda^2)$  are the optimally weighted spectra of Q and U as described above.  $\hat{F}(\text{RM})$  is proportional to the linear polarization for a given RM correction, and this can therefore be interpreted as a linear polarization maximization method. The most probable value of the RM then occurs where  $\hat{F}(\text{RM})$  peaks; a parabola is fit to an oversampled RM range around the peak and its maximum taken to be the RM estimate. An error on this value is estimated as the full-width at half-max (FWHM) of the RM spread function (RMSF), divided by the linear-polarization S/N:

$$\sigma_{\text{RM1}} = \frac{\text{FWHM}\sigma_L}{\max(\hat{F}(\text{RM}))} \quad (\text{I19})$$

where  $\sigma_L$  is the off-peak standard deviation in the linear-polarization signal,  $|P(t)|$ , after applying the ideal spectral weights described in the previous section. Sources here are assumed to be ‘Faraday thin’, meaning that for a small emitting volume, the amount of Faraday rotation that can occur is strictly limited; each FRB with significant RM is then assumed to have a dispersion function that peaks at only one value (e.g., Brentjens & De Bruyn 2005).

RM synthesis is first performed with the *RM-tools* package<sup>19</sup>, a Python implementation which also uses ‘cleaning’ to minimize sidelobes in the RM spectrum (Purcell et al. 2020). In order to exercise more control over the trial RM range, resolution, and synthesis method, an RM synthesis pipeline was implemented within the *dsa110-pol* library as *faradaycal*. In this function, the RM range and resolution can be specified, and since synthesis is implemented by brute force without optimization, the trial RM range can be arbitrarily wide and fine, and within arbitrary limits. Following synthesis with *RM-tools*, *faradaycal* is run on a fine RM trial grid ( $10^6$  trial RMs from  $\pm 10^6 \text{ rad m}^{-2}$  for a resolution  $2 \text{ rad m}^{-2}$ ). A smaller region of  $\pm 1000 \text{ rad m}^{-2}$  is then defined around the peak in the FDF and run with 5000 trial RMs for a resolution of  $0.4 \text{ rad m}^{-2}$  to obtain a better estimate.

The traditional RM synthesis methods described above operate on the time-averaged spectrum of an FRB, and therefore neglect any time-variation in polarization properties that could warp the measured RM. To address this, an additional RM synthesis function, *faradaycal\_SNR* has been implemented within the *dsa110-pol* library. Rather than operating on the time-averaged spectrum, *faradaycal\_SNR* instead applies for each trial RM de-rotation at each time-step within the burst as shown below:

$$P_{\text{RM}}(t, \lambda^2) = P_{\text{obs}}(t, \lambda^2)(\lambda^2)e^{-2i\text{RM}(\lambda^2 - \lambda_0^2)} \quad (\text{I20})$$

The linear-polarization S/N for each trial RM,  $\hat{F}_{\text{S/N}}$ , is then calculated by averaging  $|P_{\text{RM}}(t, \lambda^2)|$  over frequency, then taking the weighted average over the pulse, using the ideal spectral weights. The detected RM is taken to be the RM such that  $\hat{F}_{\text{S/N}}$  is maximized. This not only includes the time dependence of polarization properties, but also more closely matches how RM calibration is applied, i.e. de-rotation is applied at each time step. However, this method, referred to as the ‘S/N Method’ is more computationally expensive, and can therefore only be run on the smaller RM range of  $\pm 1000 \text{ rad m}^{-2}$  around the peak determined from running *faradaycal*. In addition to obtaining the RM through synthesis with the time averaged S/N, the S/N method is performed on the spectrum at each timestep within the burst to investigate any time dependence on sub-millisecond timescales.

<sup>19</sup> <https://github.com/CIRADA-Tools/RM-Tools>

Brentjens & De Bruyn (2005) estimate the error in RM determined from RM synthesis to be equivalent to that estimated from QU-fitting, shown below, in the limit of high S/N:

$$\sigma_{\text{RM}} = \frac{\sqrt{3}\sigma}{4|P|(\lambda_{\text{max}}^2 - \lambda_{\text{min}}^2)} \quad (\text{I21})$$

where  $|P|$  is the linear polarization at the peak RM, and  $\sigma$  is the root-mean-squared (RMS) noise in the Q and U maps. However, many of the FRBs detected in this sample have low S/N, and this error is likely an underestimate. A more conservative error is estimated through a small simulation, in which 100 top-hat pulses are simulated at linear-polarization S/N trials between 1,2,...,20. The RM is then estimated for each trial and the error taken to be the standard deviation of all trials. The results of this simulation, as well as the error estimate from Brentjens & De Bruyn (2005) are shown in Figure 12. From this, it is clear that there is higher scatter in RM than implied by the formula above. Since a  $9\sigma$  threshold is imposed on the peak  $\hat{F}_{\text{S/N}}$  based on the linear-polarization S/N needed to clearly resolve a peak in the RM spectrum<sup>20</sup>, an exponential of the form:

$$\sigma_{\text{RM2}} = Ae^{B\hat{F}_{\text{S/N}}} \quad (\text{I22})$$

is fit to the simulated error above  $\sim 6\sigma$ . A least-squares fit results in best-fit parameters  $A = 35.17$ ,  $B = -0.08$ . This exponential is shown in Figure 12.

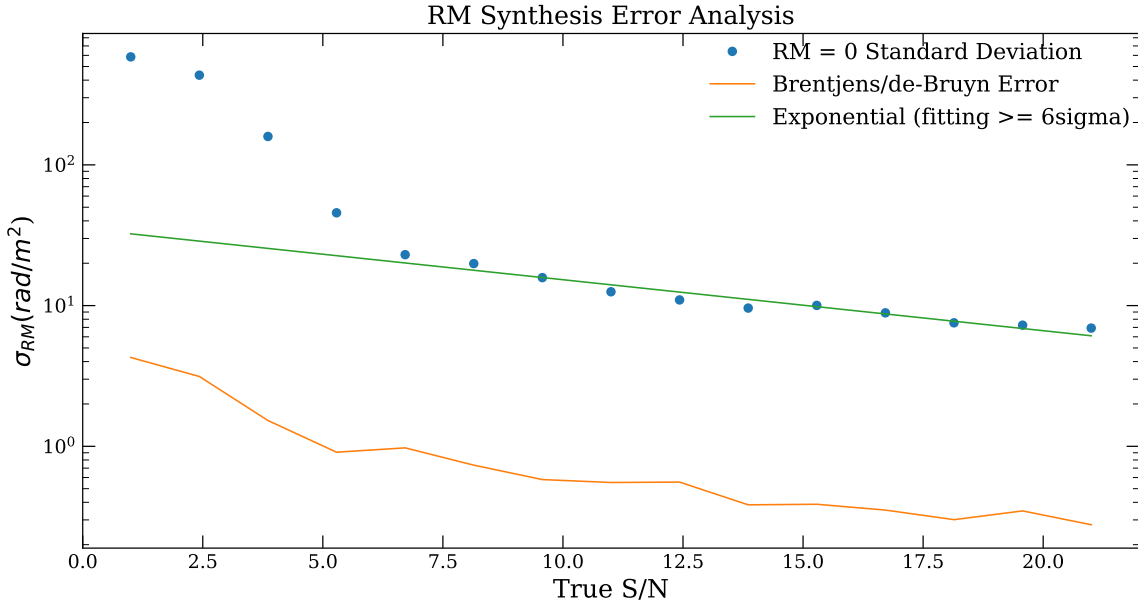


**Figure 12.** Simulated error in the recovered RM through RM Synthesis, as a function of linear-polarization S/N. See text for details of the simulation. For each true S/N, the mean analytic RM-uncertainty estimate from Brentjens & De Bruyn (2005) is shown as an orange curve. The blue points show the standard deviations of the recovered RMs, which are fit by the green line.

<sup>20</sup> Note this threshold is determined through trial and error and was still subject to visual scrutiny in the reported results.

We apply the standard RM synthesis methods to each FRB on the full range of sensitivity from  $\pm 10^6 \text{ rad m}^{-2}$ . This range was estimated following the method outlined by [Mckinven et al. \(2021\)](#), which computes the maximum RM before the PA,  $\chi$  can change significantly due to Faraday rotation. The change in PA that can occur within a frequency channel is given by [Burke et al. \(2019\)](#):

$$\Delta\chi = \frac{-2\text{RM}c^2\Delta\nu}{\nu_c^3} \quad (\text{I23})$$

where  $\Delta\nu$  is the width of each frequency channel and  $\nu_c$  is the center frequency. The fraction of the initial polarization as a function of RM is then [Schnitzeler & Lee \(2015\)](#):

$$f = \frac{\sin(\Delta\chi)}{\Delta\chi} \quad (\text{I24})$$

Figure 13 shows a plot of  $f$  as a function of trial RM. The DSA-110's high frequency resolution means that it is sensitive to RM rotation up to  $\text{RM}_{\text{max}} = 9.6_{-1.8}^{+2.0} \times 10^5 \text{ rad m}^{-2}$ , making it well-equipped to detect RM's larger than the current maximum (FRB 20121102, which has an RM on the order of  $\sim 10^5 \text{ rad m}^{-2}$ ) ([Hilmarsson et al. 2021b](#)).

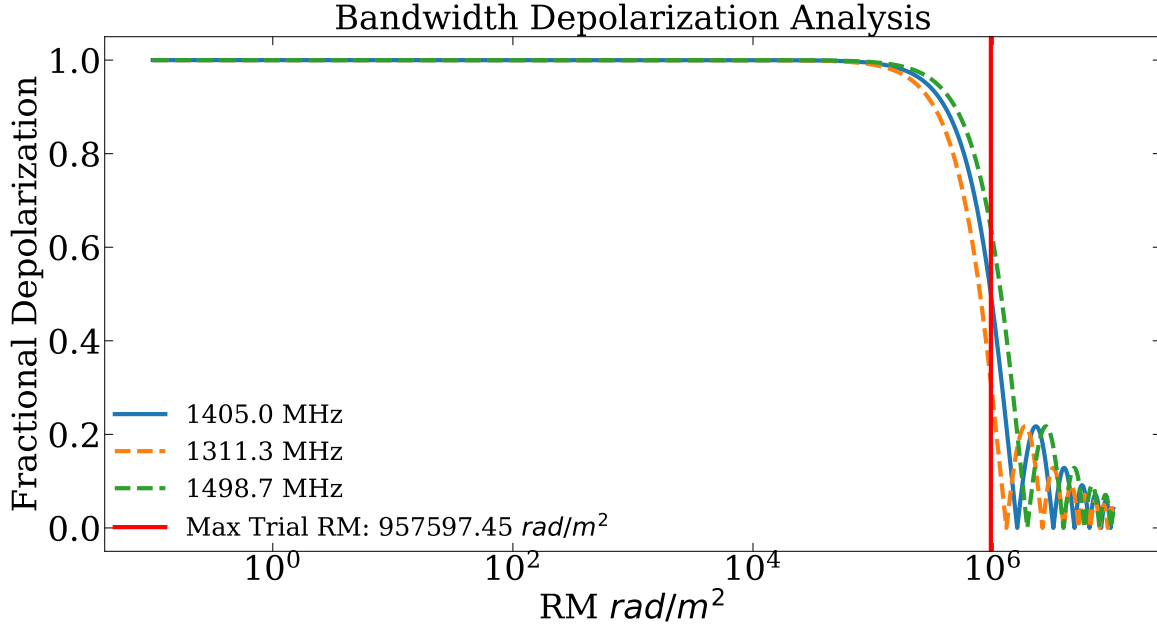


**Figure 13.** Fractional depolarization the DSA-110 as a function of RM, for different frequencies within the DSA-110 band.

## J. AN RM-SCATTERING SCENARIO FOR FRB 20220319D (MARK)

Recall that for FRB 20220319D,  $\text{DM}_{\text{host}}$  and therefore  $\bar{B}_{\parallel}$  could not be accurately estimated given its close proximity to the Milky Way ([Ravi et al. 2023](#)). One can instead place limits on the host magnetic field by assuming the derived  $\sigma_{\text{RM}}$  and using a scattering timescale,  $\tau_s$ , assuming that all

depolarization is due to stochastic RM variation. A detailed derivation is described in the supplementary material of [Feng et al. \(2022b\)](#), and a short summary is provided here.

If all refractive scattering is contributed by a screen within the host galaxy at a distance  $R$  from the source, the scattering timescale  $\tau_s$  is related to the refraction angle  $\theta_s$  by:

$$\tau_s \approx \frac{R\theta_s^2}{2c} \quad (\text{J25})$$

The spatial scale of fluctuations in the electron density causing this refraction is then:

$$l_{\text{scat}} \approx \theta_s R \approx \sqrt{2c\tau_s R} \quad (\text{J26})$$

If it is further assumed that the screen has stochastic RM variations with standard deviation  $\sigma_{\text{RM}}$  around mean  $|\text{RM}_{\text{scat}}|$ , they can be written as:

$$\sigma_{\text{RM}} \approx \sqrt{\frac{R}{l_{\text{scat}}}} |\text{RM}_{\text{scat}}|. \quad (\text{J27})$$

$|\text{RM}_{\text{scat}}|$  is created by a perturbation in the electron-density or magnetic field. Assume for simplicity that only the electron density  $n_e$  is perturbed so that:

$$\sigma_{\text{RM}} \approx \sqrt{Rl_{\text{scat}}} \frac{r_e^2}{2\pi e} \bar{B}_{\parallel} \delta n_e \quad (\text{J28})$$

where  $r_e$  is the classical electron radius, and  $e$  is the electron charge. Solving for  $\bar{B}_{\parallel} \delta n_e$ ,

$$\bar{B}_{\parallel} \delta n_e \approx \frac{2\pi\sigma_{\text{RM}}e}{r_e^2(2c\tau_s R^3)^{1/4}}. \quad (\text{J29})$$

In FRB 20220319D's case, the low  $\text{DM} = 110.95 \text{ pc cm}^{-3}$  suggests the scattering screen is not located near the source. Assume instead that  $R \sim 1 \text{ kpc}$ . Consider first taking the estimated  $\sigma_{\text{RM}} = 20.81 \text{ rad m}^{-2}$ , and the upper limit on scattering derived for FRB 20220319D,  $\tau_s \leq 0.061 \text{ ms}$  ([Ravi et al. 2023](#)). This results in a lower limit of  $\bar{B}_{\parallel} \delta n_e \gtrsim 139.9 \mu\text{G cm}^{-3}$ . For electron-density variations of order  $\delta n_e \sim 0.01 - 0.1 \text{ cm}^{-3}$  (estimated from  $\text{DM}$  and  $R$ ), this would require a magnetic field  $\bar{B}_{\parallel} \lesssim 1399.0 - 13989.5 \mu\text{G}$ , which would be relatively high compared to the typical ISM magnetic field, but consistent with a dense (e.g., star-forming) intervening environment.

Alternatively, [Feng et al. \(2022b\)](#) identifies a correlation of  $\sigma_{\text{RM}}$  with  $|\text{RM}|$  that can be approximated by  $|\text{RM}| \propto 100\sigma_{\text{RM}}$ . Following this rule, a more likely value for FRB 20220319D would be  $\sigma_{\text{RM}} \approx 0.73 \text{ rad m}^{-2}$ , implying the intrinsic emission is not 100% polarized<sup>21</sup>. Under this assumption, the upper limit becomes  $\bar{B}_{\parallel} \delta n_e \gtrsim 4.9 \mu\text{G cm}^{-3}$ . Again using electron-density variations of order  $\delta n_e \sim 0.01 - 0.1 \text{ cm}^{-3}$ , this would require a magnetic field  $\bar{B}_{\parallel} \lesssim 73.9 - 739.5 \mu\text{G}$ . Although this is still large, it is more easily achievable in a Milky Way-like environment. The two scenarios give insignificant mean  $|\text{RM}_{\text{scat}}| \ll \text{RM}$ , equal to  $3.9 \times 10^{-3} \text{ rad m}^{-2}$  and  $0.1 \times 10^{-3} \text{ rad m}^{-2}$ , respectively. In summary, an RM scattering scenario for the depolarization of FRB 20220319D is likely more plausible than for other DSA-110 FRBs, but would nonetheless require an unusually dense and magnetized intervening system.

<sup>21</sup> The RM value used here is derived from as host galaxy contribution to the RM, which is derived in the companion paper, [Sherman et al. \(2023\)](#)

## K. PPA VARIATION ANALYSIS

To estimate the significance of PPA ( $\chi_0$ ) variations, we conduct a variation of the  $\chi^2$  test that can be applied to circular data. For this we follow methods described in [Mardia & Jupp \(2000\)](#), which we refer to as MJ2000 (see also [Mardia 1972](#); [Rao 1972](#); [Mardia & Zemroch 1975a,b](#), and [NCSS Technical Procedures Documentation<sup>22</sup>](#)). To determine if the PPA is constant, we assume a null hypothesis (H0) that the PPA is distributed as a von Mises random variable with mean angle  $\hat{\mu}$  and concentration parameter  $\hat{\kappa}$ . For each FRB, we estimate  $\hat{\mu}$  from the set of PPA  $\{\chi_{0,i}\}$  in time bins with linear  $S/N > 3\sigma$  using equations 2.2.1-2.2.4 in MJ2000:

$$\hat{\mu} = \begin{cases} \tan^{-1}(\frac{\bar{S}}{\bar{C}}), & \text{for } \bar{C} \geq 0 \\ \tan^{-1}(\frac{\bar{S}}{\bar{C}}) + \pi, & \text{for } \bar{C} < 0 \end{cases} \quad (\text{K30})$$

where  $\bar{C}$  and  $\bar{S}$  are defined as:

$$\bar{C} = \frac{\sum \sigma_{\chi_{0,i}}^{-2} \cos(\chi_{0,i})}{\sum \sigma_{\chi_{0,i}}^{-2}} \quad (\text{K31})$$

$$\bar{S} = \frac{\sum \sigma_{\chi_{0,i}}^{-2} \sin(\chi_{0,i})}{\sum \sigma_{\chi_{0,i}}^{-2}} \quad (\text{K32})$$

where  $\{\sigma_{\chi_{0,i}}\}$  are the uncertainties on each PA sample. From MJ2000 equation 5.3.5, the maximum likelihood estimate of  $\hat{\kappa}$  is defined by the condition:

$$\frac{I_0(\hat{\kappa})}{I_1(\hat{\kappa})} = \bar{R} \quad (\text{K33})$$

where  $\bar{R} = \sqrt{\bar{C}^2 + \bar{S}^2}$  and  $I_d$  is the  $d^{\text{th}}$  order modified Bessel function of the first kind. We use a spline linear interpolation to numerically solve for  $\hat{\kappa}$ . Finally the Score test statistic, which we refer to as  $\chi_{\mathcal{L}}^2$ , is given by:

$$\chi_{\mathcal{L}}^2 = \begin{cases} 2N\hat{\kappa}(\bar{R}_{\hat{\mu}} - \bar{C}_{\hat{\mu}})(1 - (4N\hat{\kappa}\frac{I_0(\hat{\kappa})}{I_1(\hat{\kappa})})^{-1}), & \text{for } N < 5 \\ 4N\frac{\bar{R}_{\hat{\mu}}^2 - \bar{C}_{\hat{\mu}}^2}{2 - \bar{C}_{\hat{\mu}}^2}, & \text{for } N \geq 5, \bar{C}_{\hat{\mu}} \leq 2/3 \\ \frac{2N}{1 + \bar{C}_{\hat{\mu}}^2 + 3n^{-1}} \ln(\frac{1 - \bar{C}_{\hat{\mu}}^2}{1 - \bar{R}_{\hat{\mu}}^2}), & \text{for } N \geq 5, \bar{C}_{\hat{\mu}} > 2/3 \end{cases} \quad (\text{K34})$$

where  $N$  is the number of PPA samples and we define:

$$\bar{C}_{\hat{\mu}} = N^{-1} \sum \cos(\chi_{0,i} - \hat{\mu}) \quad (\text{K35})$$

$$\bar{S}_{\hat{\mu}} = N^{-1} \sum \sin(\chi_{0,i} - \hat{\mu}) \quad (\text{K36})$$

$$\bar{R}_{\hat{\mu}} = \sqrt{\bar{S}_{\hat{\mu}}^2 + \bar{C}_{\hat{\mu}}^2} \quad (\text{K37})$$

<sup>22</sup> [https://www.ncss.com/wp-content/themes/ncss/pdf/Procedures/NCSS/Circular\\_Data\\_Analysis.pdf](https://www.ncss.com/wp-content/themes/ncss/pdf/Procedures/NCSS/Circular_Data_Analysis.pdf)

Through Monte Carlo simulations, we verify that  $\chi^2_{\perp}$  follows a  $\chi^2$  distribution with one degree of freedom, and use this to compute a p-value for each FRB's  $\chi^2_{\perp}$  estimate.

After computing  $\chi^2_{\perp}$  for each FRB, we find no significant PPA variations at the 90% level or beyond. From visual inspection of some bursts, for example FRB 20220207C and FRB 20220310F (see Figures 14-17), that show evidence of variation without being identified as significant, we infer that the large PPA uncertainties and small N prevent rejection of the null hypothesis. We follow-up this analysis by computing the maximum difference in PPA across each FRB and its significance, following a similar method to Jiang et al. (2022, (Appendix C)). With this we find a maximum  $3.8\sigma$  PPA change across FRB 20220310F, which supports the mode change discussed in Section 3. A less significant  $2\sigma$  PPA change is observed for FRB 20220207C, supporting the  $\chi^2_{\perp}$  result that its PPA variation is not significant.

#### L. SUMMARY PLOTS FOR 25 DSA-110 FRBS

#### M. RM TIME EVOLUTION PLOTS FOR MULTICOMPONENT FRBS

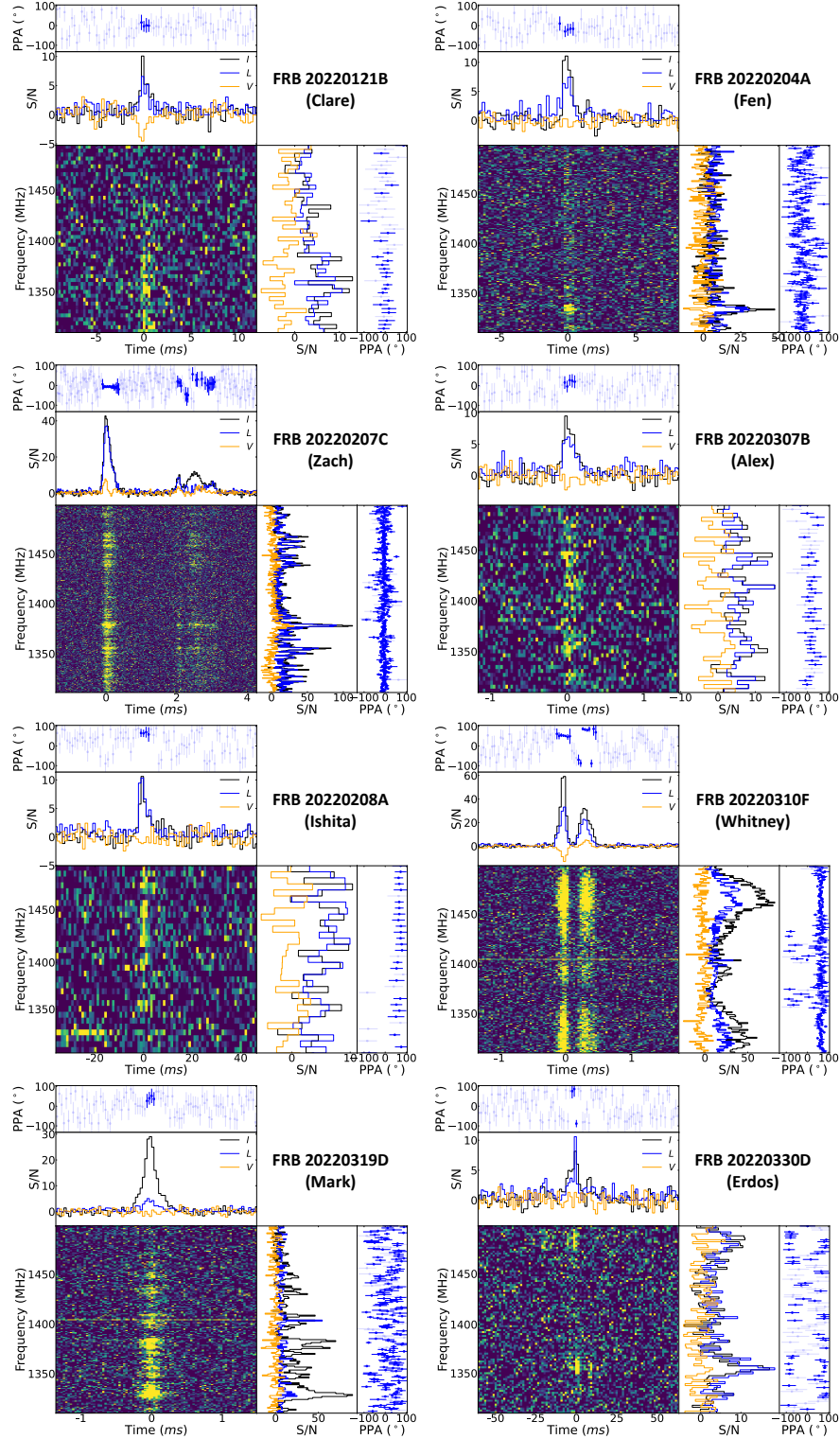


**Figure 14.** Summary of polarization data for each DSA-110 FRB. For each FRB, from top, we show the PPA (with  $1\sigma$  errorbars) measured after correcting for RM, and frequency averaged time series of Stokes  $I$ ,  $L$ , and  $V$ . The PPA is highlighted in bins with linear-polarization  $S/N > 3\sigma$ . The dynamic spectrum is shown at center, to the right of which are shown optimally summed spectra (Appendix H) and the spectrally resolved PPA with  $> 3\sigma$  bins highlighted. For FRBs with no measured RM, the PA without RM correction, rather than the PPA is shown.

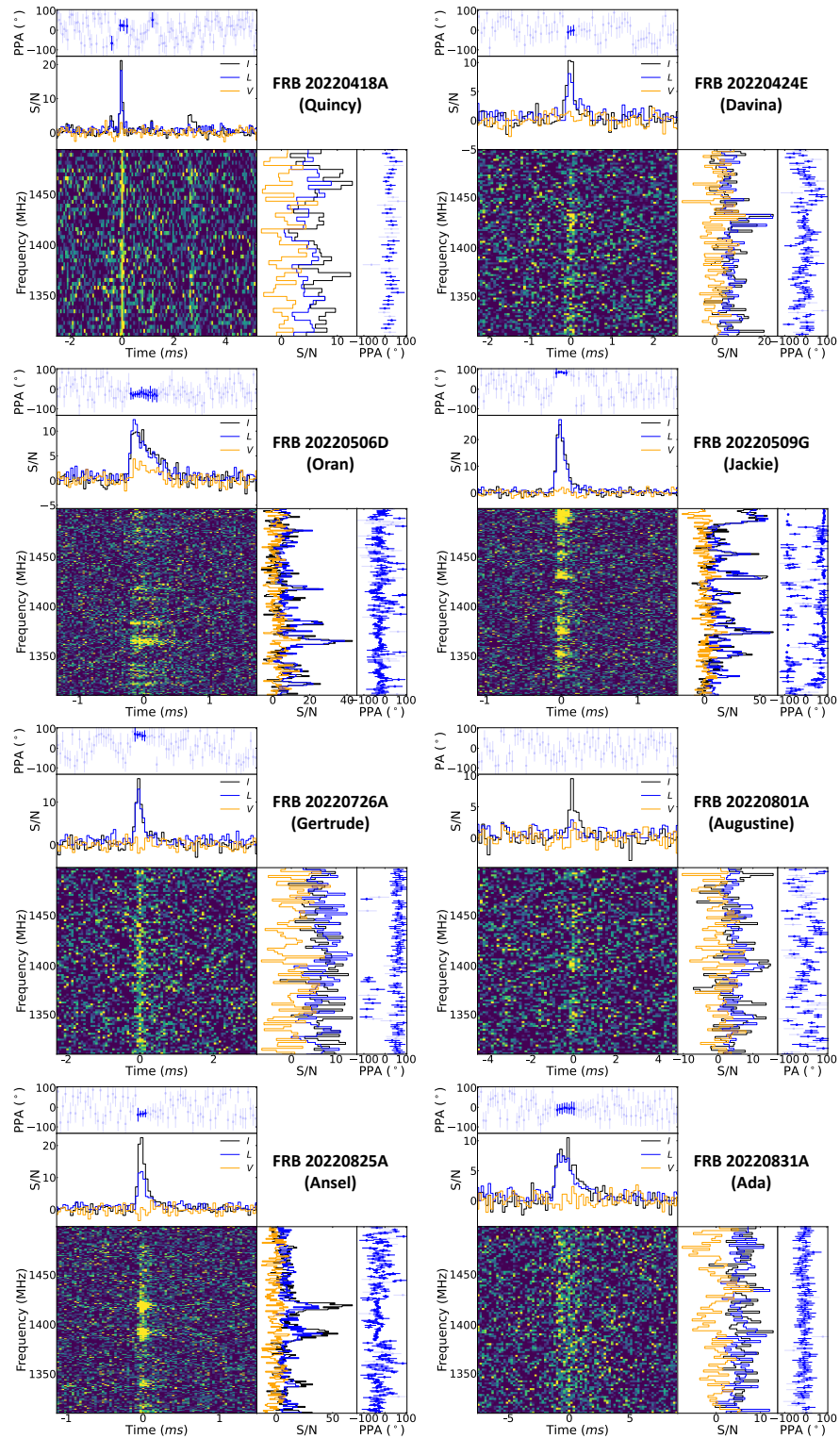


Figure 15. Same as Figure 14

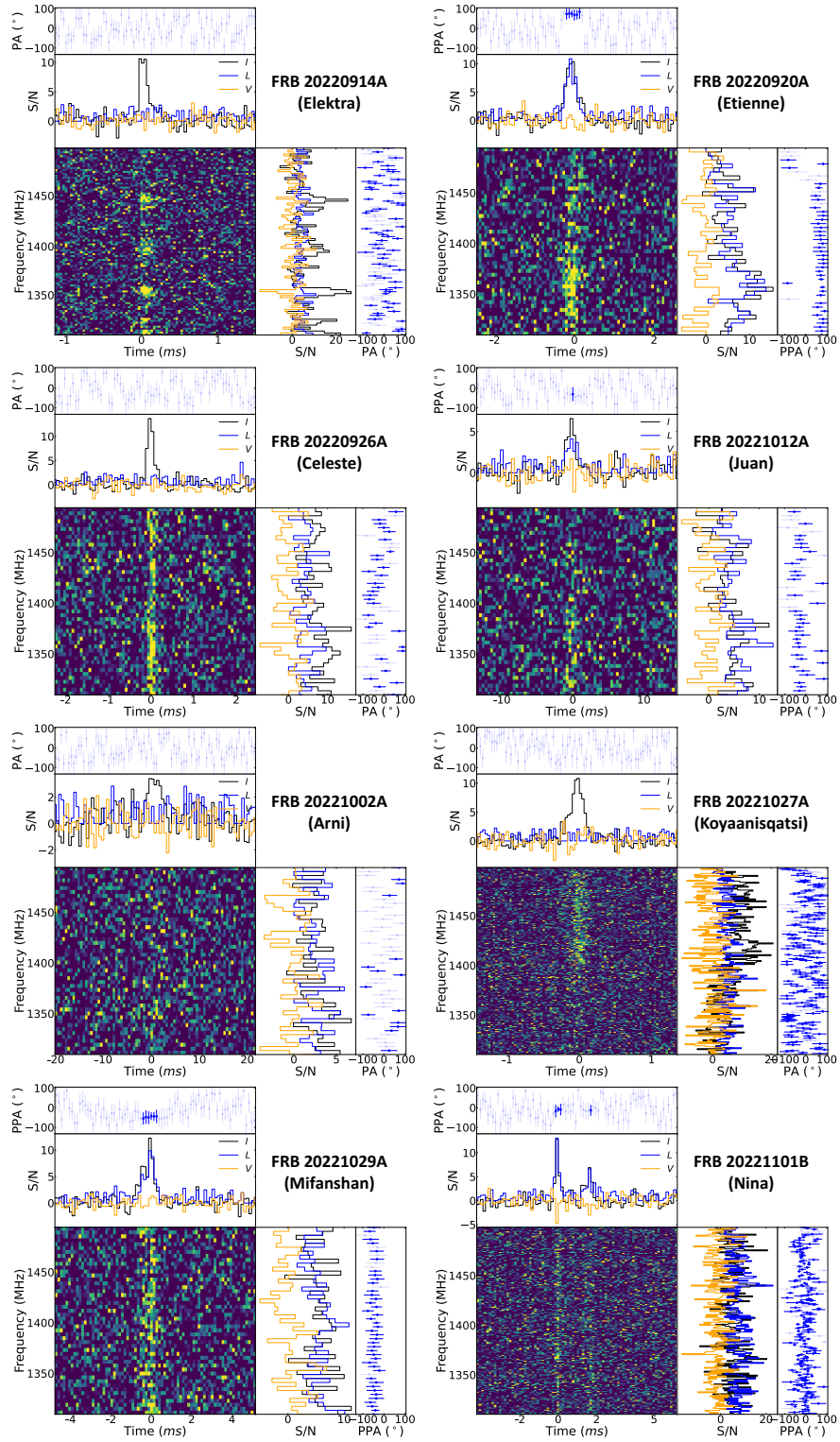
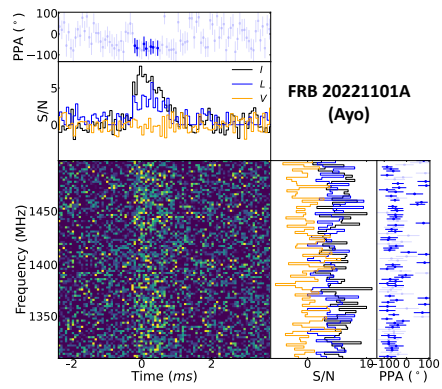
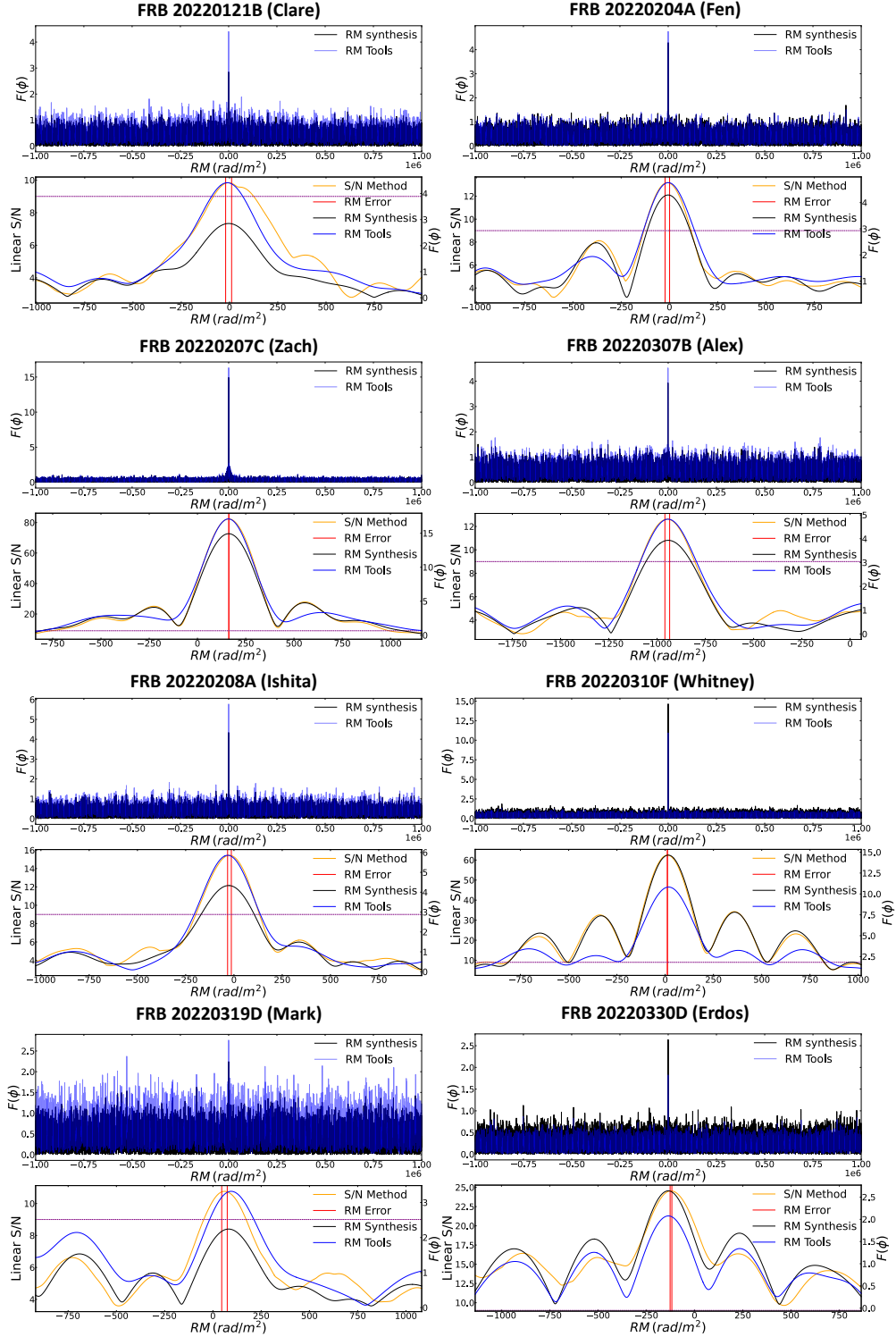


Figure 16. Same as Figure 14



**Figure 17.** Same as Figure 14



**Figure 18.** Summary of RM data on each FRB with significant detection. For each FRB, the top panel shows the RM spectra evaluated over the full range of sensitivity using two different methods (Appendix I), and the bottom panel shows a detailed analysis of the S/N of the peak. The horizontal purple line indicates the  $9\sigma$  significance threshold applied to the S/N Method spectrum (yellow).

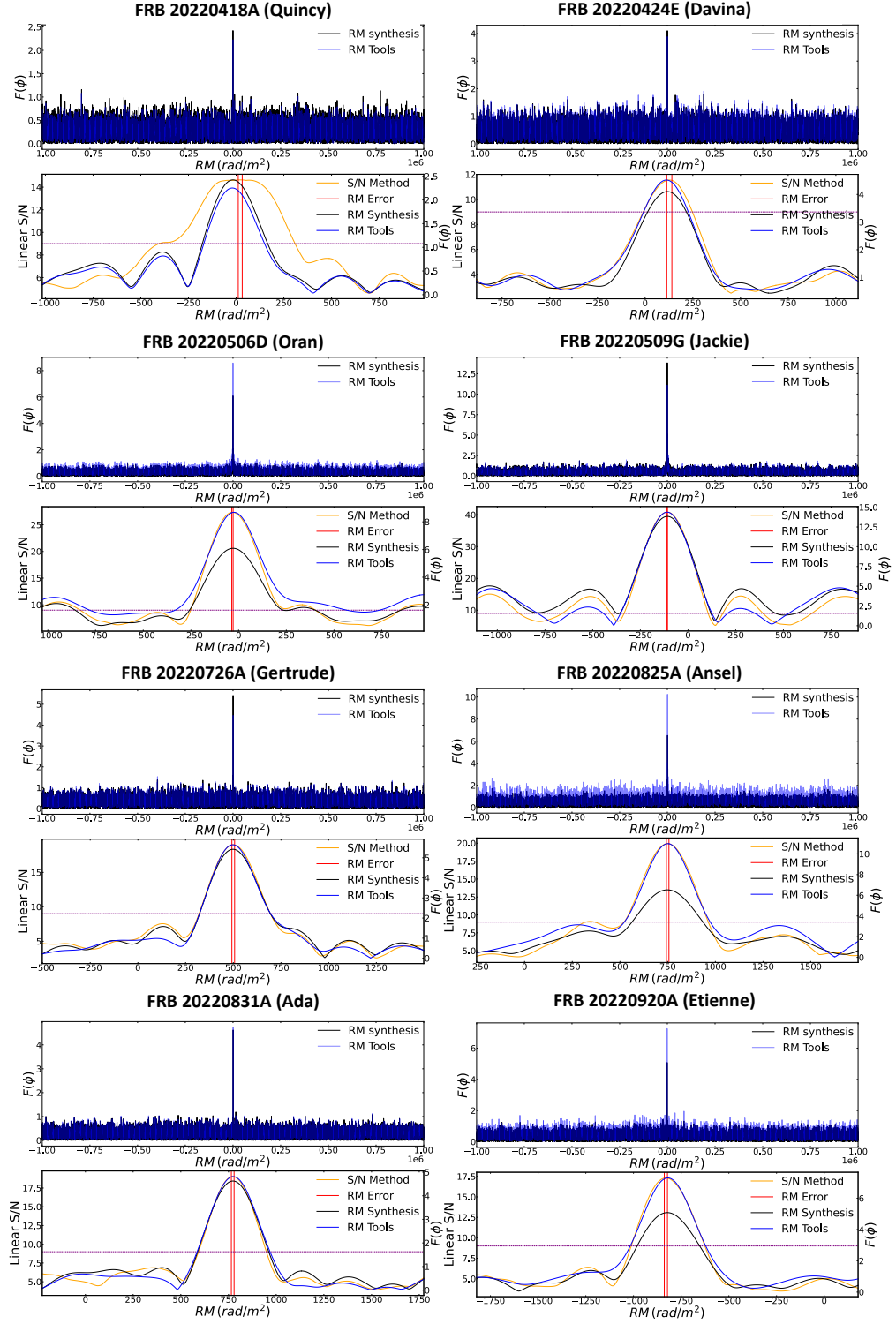


Figure 19. Same as Figure 18

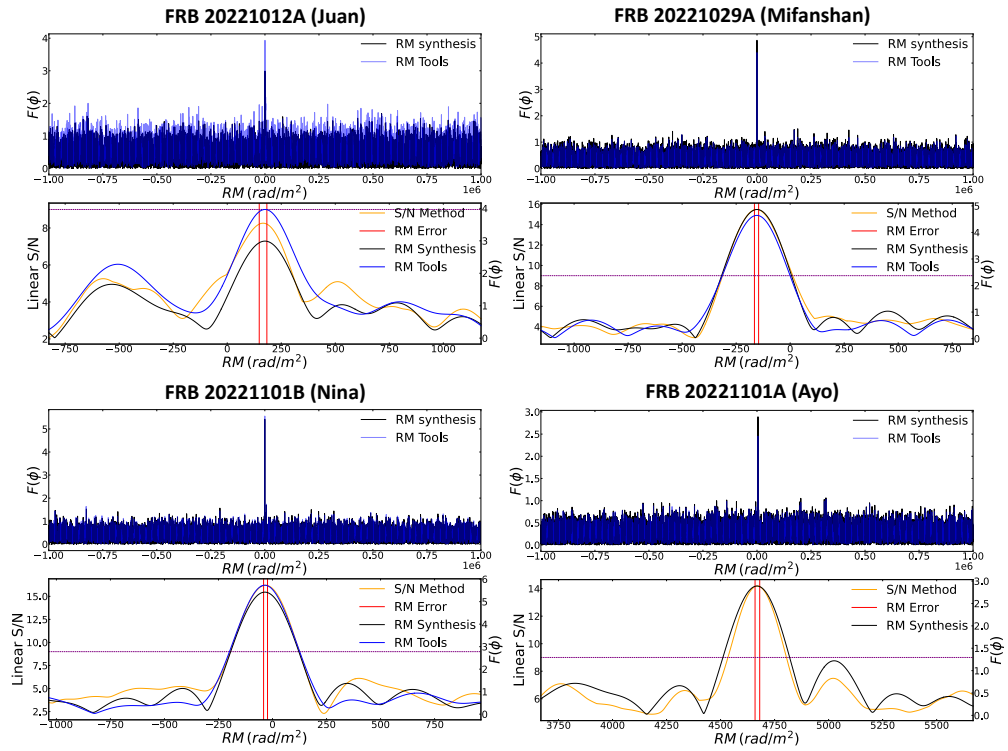
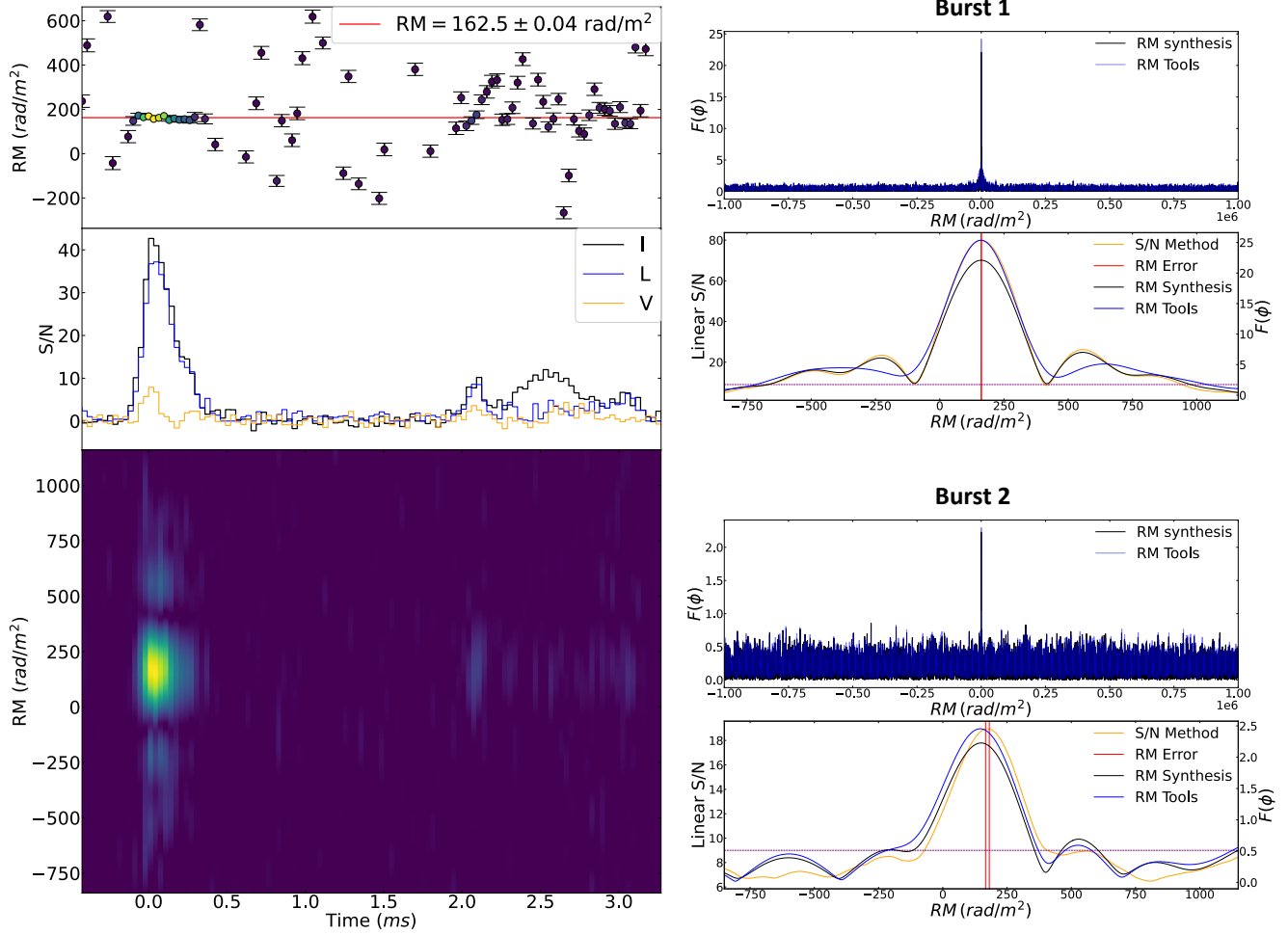
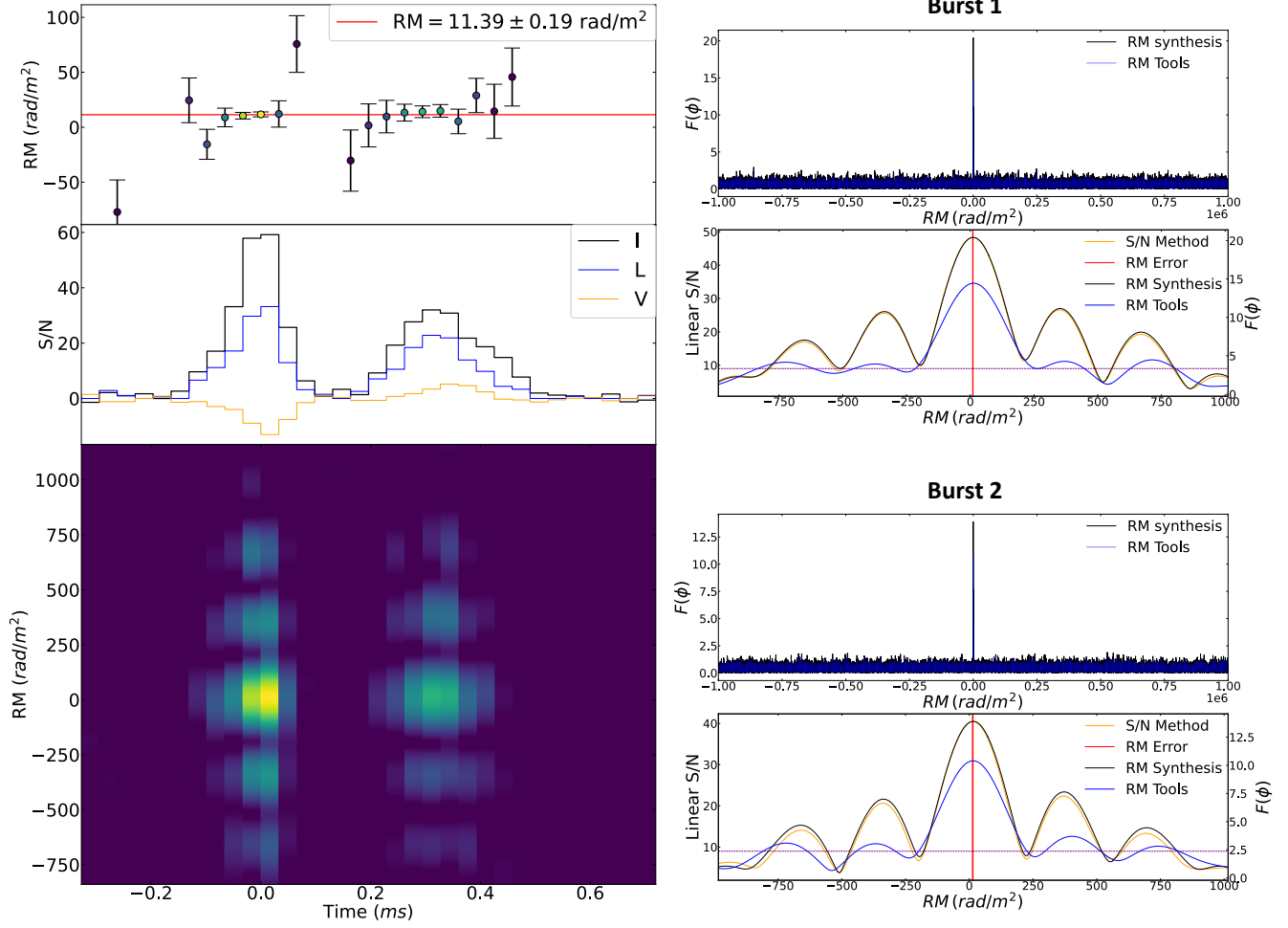


Figure 20. Same as Figure 18



**Figure 21.** Time evolution of RM in FRB 20220207C; *Right:* The top plot shows the measured RM from the S/N method for each time bin; the polarized profile showing Stokes I (black), linear polarization (blue) and circular polarization (orange) is shown in the middle plot. The bottom plot shows the RM spectrum in each time bin, referred to as the Rotation Measure Transform. In the top plot, the color of each point corresponds to the peak S/N in the RM spectrum for that time bin, and correlates with the colormap in the RM transform. The red line is drawn at the average RM value from both sub-components,  $162.48 \pm 0.04 \text{ rad m}^{-2}$ . *Right:* The RM synthesis summary plots are shown for sub-bursts 1 (top) and 2 (bottom) individually. See the caption for Figure 18 for a description of each trace in the RM synthesis plots.



**Figure 22.** Same as Figure 21 for FRB 20220310F. The red line is drawn at the average RM value from both sub-components,  $11.4 \pm 0.2 \text{ rad m}^{-2}$ .

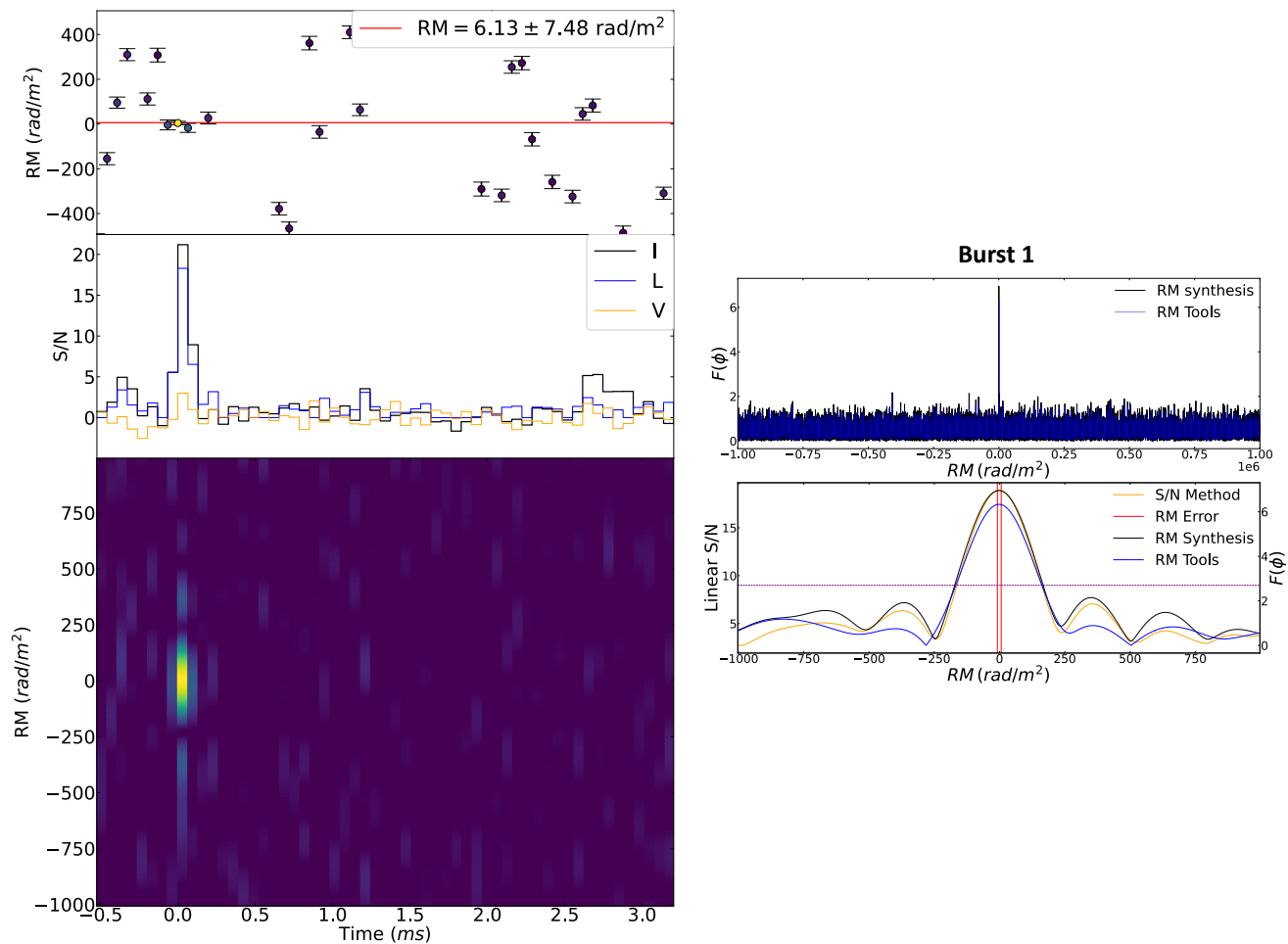


**Figure 23.** Same as Figure 21 for FRB 20220418A. The red line is drawn at the average RM value from all sub-components,  $6.1 \pm 7.5 \text{ rad m}^{-2}$ . For the individual components, a significant RM is found only for the first.

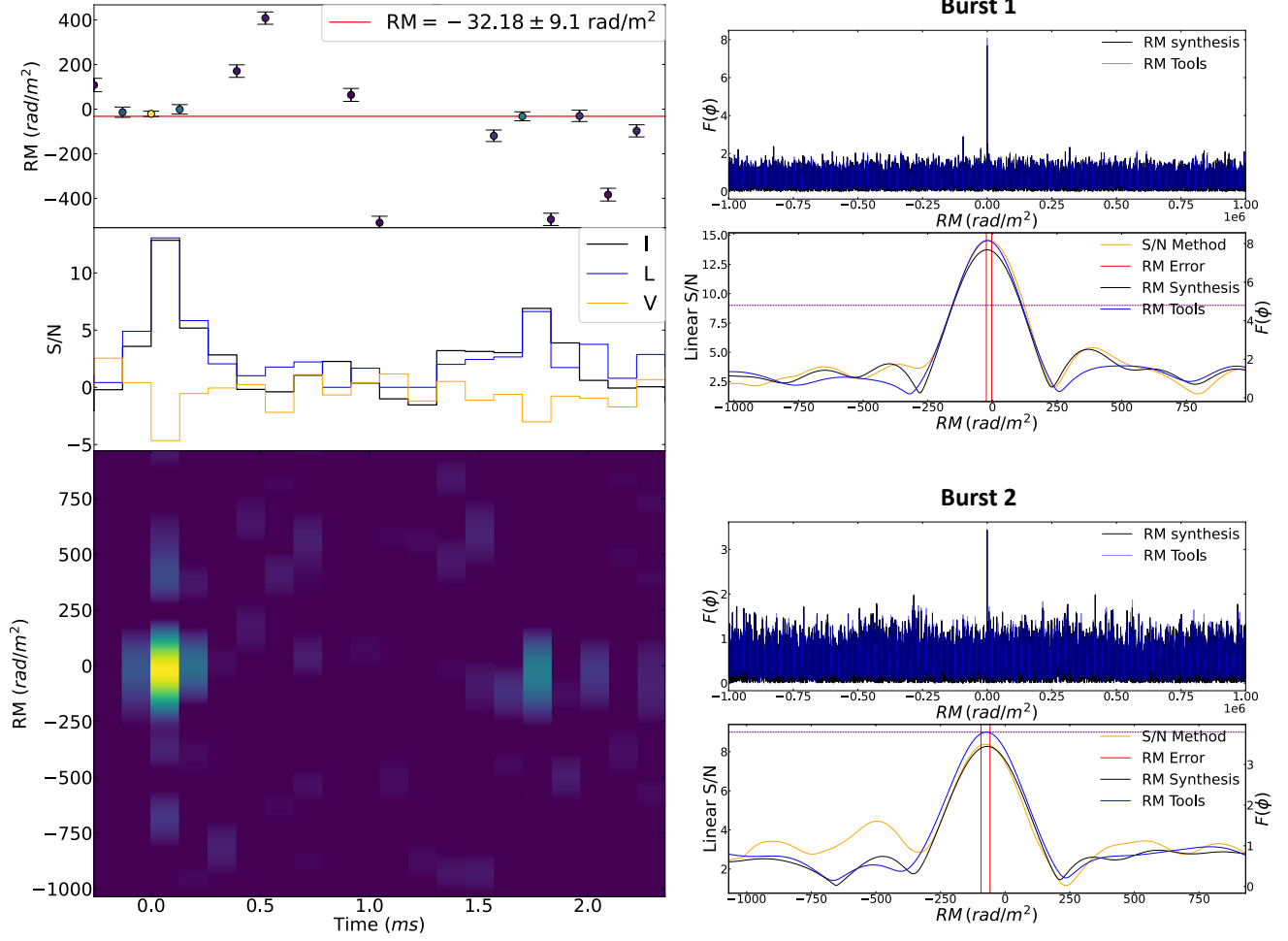


**Figure 24.** Same as Figure 21 for FRB 20221101B. The red line is drawn at the average RM value from both sub-components,  $-13.1 \pm 10.5 \text{ rad m}^{-2}$ .